# Investigations on reactively driven ion beam etching procedures for improvement of optical aluminium surfaces

Von der Fakultät Maschinenwesen

der

Technischen Universität Dresden

zur

Erlangung des akademischen Grades

Doktor-Ingenieur (Dr.-Ing.)

angenommene Dissertation

M. Eng. Ulitschka, Melanie
geb. am: 02.06.1989 in: Hof/Saale

Tag der Einreichung: 17.12.1019
Tag der Verteidigung: 13.08.2020

Gutachter: Prof. Dr. rer. nat. T. Arnold
Prof. Dr.-Ing. A. Lasagni

Vorsitzender der Promotionskommission: Prof. Dr. rer. nat. H. Jäger

Diese Arbeit wurde im Zeitraum Februar 2017 bis Dezember 2019 am Leibniz-Institut für Oberflächenmodifizierung e. V. Leipzig angefertigt.

This work was prepared from February 2017 until December 2019 at the Leibniz Institute of Surface Engineering Leipzig.

Betreuer / Supervisors: Prof. Dr. T. Arnold / Dr. J. Bauer

**This work is dedicated to my family and friends,**

**who have always been a source of love,**

**support, encouragement, and inspiration**

# Bibliographische Beschreibung

Ulitschka, Melanie

*Investigations on reactively driven ion beam etching procedures for improvement of optical aluminium surfaces*

Technische Universität Dresden, Dissertation,

141 Seiten, 193 Quellen, 70 Abbildungen, 14 Tabellen, 8 Gleichungen, 2 Anhänge.

## Kurzfassung

Das reaktiv gesteuerte Ionenstrahlätzen von optischen Aluminiumoberflächen bietet einen vielversprechenden Prozessansatz, um Formfehlerkorrektur, Glättung periodischer Drehstrukturen und die Reduzierung von Rauheitsmerkmalen im Ortsfrequenzbereich der Mikrorauheit in einer Technologie zu kombinieren. Diese Arbeit konzentriert sich auf die experimentelle Analyse der niederenergetischen Ionenbestrahlung von einkorn-diamantgedrehten, technischen Aluminiumlegierungen RSA Al6061 und RSA Al905. Die Ionenstrahlbearbeitung unter Verwendung der Prozessgase Sauerstoff und Stickstoff ermöglicht eine direkte Oberflächenformfehlerkorrektur bis zu 1 µm Bearbeitungstiefe unter Beibehaltung der Ausgangsrauheit. Die sich aus dem vorangegangenen Formgebungsverfahren, dem Einkorn-diamantdrehen, ergebende Drehmarkenstruktur schränkt allerdings häufig die Anwendbarkeit dieser Spiegeloberflächen im kurzwelligen Spektralbereich ein. Daher wurde im Rahmen dieser Arbeit ein zweistufiger Prozessablauf entwickelt, um eine weitere Verbesserung der Oberflächenrauheit zu erreichen. Durch die Ionenstrahl-Planarisierungstechnik unter Verwendung einer Opferschicht werden die im hohen Ortsfrequenzbereich liegenden Drehmarken erfolgreich um insgesamt 82 % reduziert. Eine Kombination mit anschließender, direkter Ionenstrahlglättung zur nachfolgenden Verbesserung der Mikrorauigkeit wird vorgestellt. Um die Prozessführung in einem industrietauglichen Rahmen zu etablieren, wurden die experimentellen Untersuchungen mit einer 13,56 MHz betriebenen Hochfrequenz-Ionenquelle durchgeführt, konnten aber auch erfolgreich auf eine Breitstrahl-Ionenquelle vom Typ Kaufman übertragen werden.

## Abstract

Reactively driven ion beam etching of optical aluminium surfaces provides a promising process route to combine figure error correction, smoothing of periodically turning structures and roughness features situated in the microroughness regime within one technology. This thesis focuses on experimental analysis of low-energy ion beam irradiation on single-point diamond turned technical aluminium alloys RSA Al6061 and RSA Al905. Reactively driven ion beam machining using oxygen and nitrogen process gases enables the direct surface error correction up to 1 µm machining depth while preserving the initial roughness. However, the periodic turning mark structures, which result from preliminary device shaping by single-point diamond turning, often limit the applicability of mirror surfaces in the short-periodic spectral range. Hence, during this work a two-step process route was developed to attain further improvement of the surface roughness. Within the ion beam planarization technique with the aid of a sacrificial layer, the turning marks situated in the high spatial frequency range are successfully reduced by overall 82 %. A combination with subsequently applied direct ion beam smoothing procedure to perform a subsequent improvement of the microroughness is presented. In order to establish the process control in an industrial framework, the experimental investigations were performed using a 13.56 MHz radio frequency ion source, but the developed process routes are also successfully transferred to a broad-beam Kaufman-type ion source.

# Danksagung

Diese Arbeit wäre nicht möglich gewesen ohne die Unterstützung vieler Menschen. Zuerst möchte ich mich bei Prof. Dr. rer. nat. Thomas Arnold bedanken. Er gab mir nicht nur die Möglichkeit, dieses Thema zu bearbeiten, sondern ermöglichte mir auch einen großen Freiraum und Selbstständigkeit in der Vorgehensweise. Selbstverständlich stand er jederzeit mit Rat und Tat zur Seite. Prof. Dr. Dr. h.c. Bernd Rauschenbach danke ich für die Möglichkeit, am IOM tätig zu sein und dadurch dieses Thema bearbeiten zu können. In diesem Zusammenhang möchte ich Prof. Dr. André Anders für die Führung des IOM und seiner Arbeit für den Erhalt der guten Arbeitsbedingungen danken.

Ein ganz besonderer Dank gebührt Dr. Jens Bauer, der mit seinem umfassenden Wissen zur Ionenstrahlbearbeitung von Aluminiumoptiken und der Erfahrung innerhalb der verwendeten Messtechnik stets eine sehr große Hilfe gewesen ist. Er spielte während der Bearbeitung des Themas eine entscheidende Rolle, da ohne seine Vorarbeiten diese Arbeit nicht möglich gewesen wäre. Zudem möchte ich betonen, dass seine von großem Maße strukturierte und durchdachte Herangehensweise an jegliche Problemstellungen immer wieder neu motivierte und er dabei immer einen ermutigenden Optimismus vermitteln konnte. Außerdem möchte ich ihm für die Durchführung der ToF-SIMS Messungen danken, zahlreicher SEM-EDX Messungen und der Durchführung der Monte Carlo Simulationen. Er hat sich immer Zeit genommen, die Ergebnisse, nächste Schritte oder andere Angelegenheiten zu besprechen.

Dr. Frank Frost gilt ebenfalls ein besonderer Dank. Durch seine umfassende Erfahrung war er eine sehr große Hilfe. Er ist nicht nur ein ausgezeichneter Wissenschaftler, sondern auch ein großartiger Mensch. Trotz seines gefüllten Terminkalenders nahm er sich immer Zeit, die Ergebnisse zu besprechen und hatte auch bei Fragen zur AFM-Messtechnik stets eine offene Tür. In diesem Zusammenhang möchte ich ihm für die Möglichkeit, und Dr. Gregor Dornberg für die Durchführung der Experimente auf der ISA 200 danken.

Dr. Ulrich Decker möchte ich für seine stets offene Art und freundliche Unterstützung bei der Analyse der Photoresistmaterialien danken. Hierbei gilt Ingrid Reinhardt für die Durchführung der TGA und DSC Messungen, Nadja Schönherr und Gabriele Mirschel für die Durchführung

der ATR-IR Messungen und Dr. Jan Griebel für die Durchführung der GC-MS Messungen ein großer Dank.

Vielen Dank auch an Herrn Dietmar Hirsch für die Durchführung von SEM-EDX und XPS Messungen.

Herrn Toni Liebeskind möchte ich für seine stets zuverlässige und überaus schnelle Arbeitsweise danken, im Speziellen die Reinigung der Probenmaterialien sowie das Beschichten und Vorbehandeln der Proben mit den Photoresistmaterialien.

Ein großer Dank gilt dem Team der IOM Werkstatt, Stefan Daum, Ann-Grit Birnbaum, Florian Hager, Birgit Voigt, Leon Jahn und Linus Knolle für die Unterstützung und die Umsetzung größerer und kleinerer Bauteile der RIBE-Forschungsanlage.

Für eine sehr gute Atmosphäre im Büro möchte ich Dr. Jens Bauer, Heike Müller und Anne Maiwald danken. Hervorheben möchte ich in diesem Zusammenhang auch Fred Pietag, Michael Mensing, Jan Griebel und Stephan Frenzel. Ich bedanke mich für das freundschaftliche Miteinander, das ermutigend war. Für ihren Beitrag zu einem kollegialen und freundschaftlichen Umfeld am IOM möchte ich auch Dr. Antje Lehmann, Dr. Georg Böhm und Herrn Hendrik Pätzelt danken.

Ich möchte allen Mitarbeitern der Verwaltung und der Abteilung Präzisionsoberflächen des IOM meinen Dank aussprechen, da sie mir auf die eine oder andere Weise geholfen haben. Ich bin ihnen sehr dankbar für ihre Hilfe und für die Schaffung eines angenehmen und freundlichen Arbeitsumfeldes. Bei allen Mitarbeitern am IOM möchte ich mich für das kollegiale und freundliche Miteinander bedanken.

Die finanzielle Unterstützung durch das Bundesministerium für Bildung und Forschung (BMBF) im Rahmen der InnoProfile-Transfer-Initiative 03IPT706X "Ultrapräzise Fertigung mit Atompartikelstrahlen" wird dankbar anerkannt.

Zum Schluss möchte ich mich bei meiner Familie und meinen Freunden bedanken. Zu euch nach Hause zu kommen ließ mich nach jeder noch so stressigen Arbeitswoche wieder entspannen. An meinen Lebensgefährten, vielen Dank für das Aufbringen der Geduld innerhalb dieser Jahre und dafür, eine Menge Freizeit zu opfern. Ich widme euch meine Arbeit, da ihr der Grund für mich seid, hier zu stehen wo ich heute bin.

# Table of Contents

*Bibliographische Beschreibung* ____ *iv*

*Danksagung* ____ *vi*

*Table of Contents* ____ *viii*

*1 Introduction* ____ *1*

*2 Surface engineering with energetic ions* ____ *8*

**2.1 Ion target interactions during ion beam erosion** ____ **8**

**2.2 Ion beam finishing methods** ____ **10**

2.2.1 Ion beam figuring ____ 11

2.2.2 Ion beam planarization ____ 12

2.2.3 Ion beam smoothing ____ 14

*3 Experimental set-up and analytical methods* ____ *15*

**3.1 Experimental set-up** ____ **15**

**3.2 Kaufman-type broad beam ion source** ____ **18**

**3.3 Materials** ____ **19**

3.3.1 Aluminium alloy materials ____ 19

3.3.2 Photoresist materials as planarization layer ____ 21

**3.4 Surface topography error regimes** ____ **22**

**3.5 Analytical Methods** ____ **23**

3.5.1 Analysis of surface roughness ____ 23

3.5.1.1 White light interferometry (WLI) ____ 23

3.5.1.2 Atomic force microscopy (AFM) ____ 25

3.5.1.3 Power spectral density (PSD) analysis ____ 27

3.5.2 Scanning electron microscopy with energy-dispersive X-ray spectroscopy (SEM-EDX) ____ 29

3.5.3 X-ray photoelectron spectroscopy (XPS) ____ 31

3.5.4 Time of flight- secondary ion mass spectrometry (ToF-SIMS) ____ 32

3.5.5 Reflectometry ____ 34

3.5.6 Photoresist composition ____ 35

3.5.6.1 Attenuated total reflection infrared spectroscopy (ATR-IR) 35
3.5.6.2 Thermogravimetric analysis (TGA) 36
3.5.6.3 Differential scanning calorimetry (DSC) 38
3.5.6.4 Gas chromatography coupled mass spectrometry (GC-MS) 39

*4 Surface engineering by reactive ion beam etching 41*

**4.1 Reactive ion beam etching with nitrogen 41**
4.1.1 Dependence of the aluminium alloy composition 42
4.1.2 Ion beam etching of Al905 44

**4.2 Local smoothing by reactive ion beam etching 50**
4.2.1 Local surface error slope dependent sputter erosion 51
4.2.2 RIBE $O_2$ direct smoothing 56
4.2.2.1 Oxygen finishing at 1.5 keV 56
4.2.2.2 Oxygen finishing at 0.6 keV 62

**4.3 Conclusions 66**

*5 Technological aspects on photoresist preparation for ion beam planarization 69*

**5.1 Selection of a suitable photoresist 69**

**5.2 Photoresist application steps 71**
5.2.1 DUV exposure of the photoresist layer 72
5.2.2 Postbake: the influence of the amount of organic solvent 73
5.2.3 Postbake: the influence of the baking temperature 74

**5.3 Influence of process gas composition 77**
5.3.1 Influence on roughness evolution during ion beam irradiation of the photoresist layer 78
5.3.2 Dependency of the process gas on the selectivity 79

**5.4 Influence of the ion energy on the selectivity 80**

**5.5 Ion beam irradiation of the photoresist layer with nitrogen at different material removal depths 81**

**5.6 Conclusions 82**

*6 Ion beam planarization of optical aluminium surfaces RSA Al6061 and RSA Al905 84*

**6.1 Photoresist application on SPDT aluminium alloys 84**

**6.2 Ion beam planarization 85**

6.2.1 Iterative nitrogen processing of RSA Al905 86
6.2.2 Iterative nitrogen processing of RSA Al6061 90
**6.3 Ion beam direct smoothing 93**
6.3.1 RIBE $O_2$ smoothing of RSA Al905 93
6.3.2 RIBE $O_2$ smoothing of RSA Al6061 97
**6.4 Conclusions 101**
***7 Process transfer to a Kaufman-type broad beam ion source 103***
**7.1 RIBE machining investigations on RSA Al905 103**
**7.2 Ion beam planarization of RSA Al6061 106**
**7.3 Ion beam incidence angle dependent sputtering 107**
**7.4 Conclusions 113**
***8 Summary 115***
***9 Conclusions and Outlook 123***
***A List of abbreviations 127***
***B Selected properties of photoresist materials 129***
***References 131***

# 1 Introduction

Optical Mirrors are designed to reflect light for a variety of applications, including beam steering, interferometry, imaging, or illumination [1-3]. An alternative to conventional glass as substrate material for a metallization layer used as a mirror device is an aluminium bulk material device. High strength and low weight allow to design large-scalable mirror optics [4,5]. Due to its good mechanical machinability, light weight, low cost and high thermal conductivity aluminium optics are rather attractive for spacecraft systems [6], high resolution imaging [1] and cryogenic applications [7,8]. Additionally, aluminium has a high reflection coefficient even in the shortwave spectral range. The reflection coefficient ranges from the infrared (IR) spectral range to the shortwave visible (VIS) and ultraviolet (UV) spectral range with values well above 90 % and therefore exceeds optical materials like gold, silver or copper [9].

The increasing demands of enhanced flexible shape adjustment and increasing surface quality require ultra-precise surface machining techniques [10]. Typical mechanical machining comprises cutting methods, such as milling, turning and drilling, and abrasive machining methods as grinding, polishing and lapping [10]. Ultra-precise cutting, referred to as single-point diamond turning (SPDT), is commonly used to figure metal surfaces in optical fabrication. The optical surface has roughness values of typically below 10 nm root mean square (rms) up to 2 – 3 nm, thus fulfilling the required precision for applications in the near infrared (NIR) and IR spectral range [3,4,11,12]. Modern telescope optics for space applications, e.g. based on Three-Mirror-Anastigmat (TMA) are designed of ultra-precise aluminium mirrors.

The machined surface after SPDT exhibits the characteristic periodic groove pattern left by the cutting tool. Those so-called turning marks have a pitch of some microns and an amplitude ranging between 10 – 30 nm. As a result, for short wavelength applications in the VIS and UV spectral range, these periodic patterns show similar optical effects like a diffraction grating deteriorating the optical performance [12,13]. The diffraction effects can lead for instance to diffracted light spots in horizontal and vertical direction around the central spot under mono-wavelength condition or degrade image quality by rainbow areas distributed around the figure of light under polychromatic conditions [14]. He and Zong [14] pointed out, that the height of

the turning marks influences the energy of specular light spot, while the width of these structures only affects the position of diffracted light.

Consequently, a post-finishing step has to be applied to reduce the height of the turning mark structures for improving surface roughness and microroughness, since the demanded tolerances for short-wave applications increase drastically [15]. For applications in VIS and UV spectral range, rms roughness values of 1 nm and <0.3 nm are required, respectively. Fig. 1.1 shows the production chain for metal mirrors production depending on the field of application and its specifications after Steinkopf et al. [3].

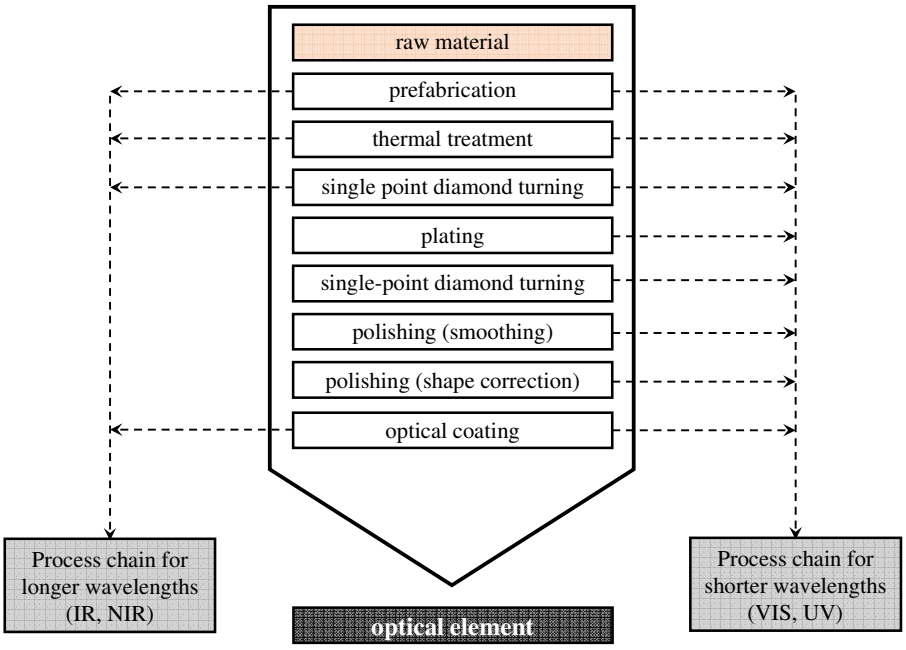


Fig. 1.1: Process chain for metal mirrors production depending on the field of application. Modified after Steinkopf et al. [3]

Mirror optics made of conventional Al6061T6 are commonly used materials for reflective optics in the IR and NIR spectral range for instruments like Visir, MIRI and X-Shooter with a resulting roughness of approximately 5 nm rms after SPDT [4,16,17]. To achieve further roughness improvement of those surfaces, an alternative to conventional aluminium alloys in the last decade has attached value. Rapidly solidified aluminium (RSA) is produced via the melt spinning process, a rapid solidification process (RSP) resulting in a more homogeneous microstructure. The polycrystalline material matrix contains grains with sizes in the micrometer range in contrast to coarse grain standard aluminium alloys. Consequently, the material made of rapid solidification process is harder and exhibits increased stiffness with improved device

construction properties. Using these RSA alloys, surface roughness values of <1 nm rms are achievable which makes these materials promising for applications in the VIS and UV spectral range [16,17]. Additionally, the generation of surface roughness during SPDT is closely related to the material properties of the workpiece to be machined and is influenced, in particular by impurities, inclusions and anisotropy [18,19]. Moreover, the diamond tool conditions and cutting process parameter have a strong impact on the surface quality due to cutting tool edge waviness, wear exert or the rake angle, the spindle speed and the feed rate of the depth of cut, respectively [18,20,21].

In order to minimize scatter losses by removing these turning mark structures, one technological solution is the electroless plating with an amorphous nickel phosphorous (NiP) layer. NiP has an isotropic amorphous matrix with excellent machining properties in SPDT and polishing processes. Diamond-turned NiP reveals smoother surfaces than aluminium and can even be further improved by post-polishing techniques like computer assisted polishing and magnetorheological finishing (MRF®) [14,22] or ion beam planarization (IBP) [23,24] (Fig. 1.1).

Supranowitz et al. and others [14,22] demonstrated the improvement of turning marks on electroless nickel-plated aluminium surfaces using MRF® resulting in a rms roughness of about 2 nm. It has been shown, that when IBP is used, turning marks are successfully reduced and a further decrease in surface roughness can be obtained by multiple run IBP processing [23,24]. Hence, micro roughness values of <1 nm rms are achievable, resulting in ultra-precise optical surfaces for VIS applications. An additional metallization layer on top of the NiP coating is necessary to realize the desired reflective properties for the specific application.

Another non-contact finishing technology after SPDT of a nickel-plated Al6061 surface is abrasive jet polishing [25]. The turning marks on both rough and fine samples were strongly reduced in one or two polishing steps while preserving the initial surface figure. In contrast to MRF®, the material removal rate of this technology is low resulting in longer finishing procedures.

Direct aluminium finishing techniques are under consideration in view of avoiding thermal stress during application when an additional amorphous coating such as NiP is used [3,6-8,12,13,26]. The mismatch of thermal expansion coefficients between aluminium substrate and

NiP coating can cause mechanical stress formation under thermal load conditions resulting in bending and distortion of the optical surface [26,27].

Since during conventional polishing the aluminium surface exhibits microscopic and macroscopic scratches due to the low hardness, the surface quality is commonly limited to IR and NIR applications only [17,28]. Although aluminium is difficult to polish, alternative techniques to simplify the process chain shown in Fig. 1.1 for applications in the short wavelength range are under investigation. Moreover, using aluminium alloy material can cause additional issue due to the heterogeneous matrix containing precipitates, grain boundaries and voids. However, with optimized polishing parameters the surface roughness can be decreased to 1 nm rms of an optical element for X-Shooter that is sufficient for VIS wavelengths as well [17].

An alternative technique for polishing after SPDT is presented by Moeggenborg et al. [29]. In contrast to traditional polishing techniques, chemical mechanical polishing (CMP) was used for finishing of standard Al6061 and Al7075 alloys. Surface roughness below 2 nm rms were achieved and proven by white light interferometry (WLI) using a 20x objective. Another method for direct aluminium polishing is based on a CMP mechanism using $SiO_2$ polishing powder with a moderate hardness polishing cloth in alkaline conditions. The turning marks on the SPDT Al6061 surface were drastically reduced and the surface roughness improved to 1.8 nm rms of initially 14.6 nm rms. However, the polishing time was about 10 h [28].

Aluminium is one preferred material used for demanding requirements on cryogenically optical earth- and space-based instrumentations, especially for monolithic high accurate device elements [17]. Surface roughness of <1 nm rms are achievable by a combination of SPDT and polishing processes. Latest results on RSA Al6061 samples show roughness values of about 1 nm rms by a combination of SPDT, MRF (for shape correction) and CMP (for finishing). The turning marks were successfully removed. These mirrors are suitable for applications in the IR and VIS spectral range [8].

Ion beam figuring (IBF) is a well-established finishing technique of optical surfaces due to its nanometer precision, highly stable and non-contact processing [30-32]. However, during IBF with an inert gas like argon, the roughness of the aluminium surface increases rapidly during the process [33]. Reactive ion beam etch (RIBE) processing is one promising technology for direct aluminium machining. In RIBE processing, the process gas contains chemically active

species which results in an etch mechanism changing from pure physical sputtering to a chemical-enhanced sputter process [34]. Usually, dry etching of aluminium is based on chlorine-based chemistry resulting in aluminium chlorides in gaseous phase [35,36]. From a technological point of view, processing with highly-reactive chlorine produces hazardous by-products.

In contrast, during processing with oxygen, nitrogen or fluorine-containing gases, no volatile products are generated but the surface to be corrected is particularly chemically modified. Consequently, a non-hazardous and stable etch mechanism is obtained. Additionally, the operation with reactive process gases as oxygen and nitrogen allows the preservation of the initial surface topography during ion beam processing [34,37].

In general, machining of optical aluminium surfaces is challenging and often requires the combination of several finishing technologies. However, in accordance to the latest results [34,37], RIBE processing is highly promising to combine shape correction via ion beam figuring (Fig. 1.2a), smoothing of the turning mark structures via ion beam planarization with the aid of a sacrificial layer (Fig. 1.2b) and a reduced microroughness via ion beam direct smoothing (Fig. 1.2c) within only one technology. Hence, the present study will analyze surface error correction methods over a broad range of spatial frequencies combined within one technology: RIBE.

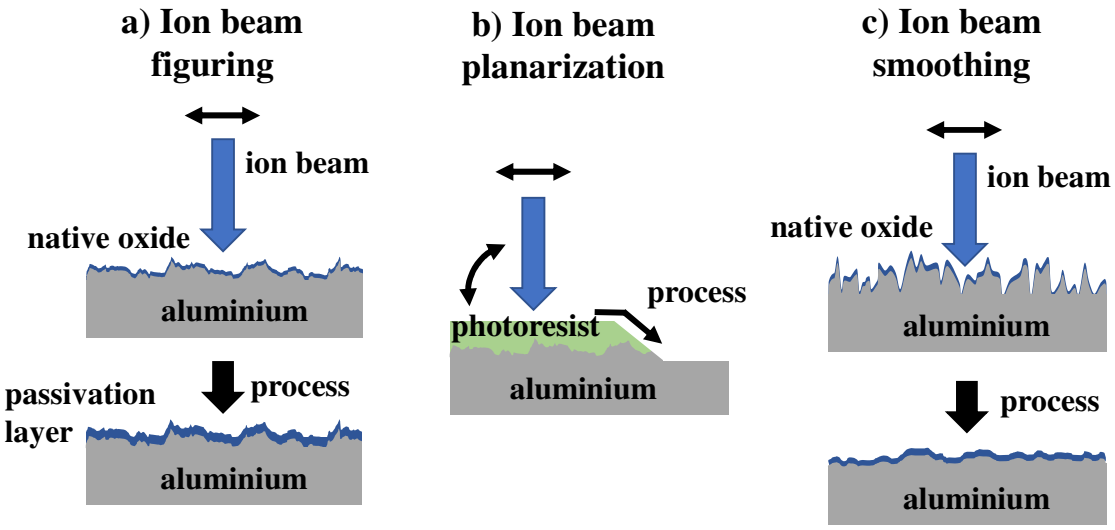


Fig. 1.2: Schematic overview of the sub-aperture ion beam techniques available for optical surface correction. a) Figure error correction via direct ion beam machining. b) Ion beam planarization with aid of a planarization layer for surface smoothing and c) surface error slope dependent direct smoothing of high spatial frequency errors

This manuscript focuses on ion beam machining of optical aluminium alloys Al6061 and Al905 produced by RSP using reactively driven low-energy ion beams of ≤1.5 keV ion energy. The objective of this work is the experimental analysis of the improvement of optical aluminium surfaces after single-point diamond turning. Ion beam figuring of optical aluminium surfaces is part of the current research within the Leibniz Institute of Surface Engineering (IOM) [34]. During studies on reactively driven ion beam figuring of optical aluminium surfaces, it was found that using oxygen gas leads to the formation of a passivation layer inhibiting aluminium surface mobility and compositional inhomogeneity, thus preserving the initial surface topography during RIBE machining up to a depth of 400 nm. The limitation was found to result from the heterogeneous matrix structure. Since reactively-driven ion beam-based smoothing of aluminium surfaces for application in the short wavelength range has been little investigated so far, this manuscript focuses on roughness improvement of these optical surfaces.

Firstly, an extension of the reactively driven ion beam figuring model scheme is analyzed to overcome the previous limitations. In this context, the influence of other reactive process gases on the evolution of surface roughness during the processing shall be investigated. This includes the determination, if the model scheme also holds for other operating gases.

Since the characteristic turning mark structures of diamond-turned surfaces degrade optical performance due to scatter losses, the main objective of the work is to reduce these structures without negatively affecting surface shape and finish. In this context, the ion beam parameters are to be adapted in such a way, that surface smoothing can be performed by means of ion beam planarization with the aid of a sacrificial layer. This allows a planar surface transfer of the smooth surface of the planarizing layer into the aluminium substrate. In the further course of the work, a suitable planarization layer is to be found with the aim of achieving equal removal rates of planarization layer and aluminium. The aim is to gain knowledge about the influence of the processing parameters on the smoothing procedure. Furthermore, on the basis of etching experiments the focus will be on the characterization of interactions between ion beam and aluminium surface and the planarization layer, assuring optimum surface transfer conditions. The investigations should provide information about contributing chemical and physical effects at the surface and determine the limiting causes for the increasing development of surface roughness in the course of higher depth RIBE.

The manuscript is organized as follows:

- Chapter 2 contains a brief description of ion beam sputtering, i.e. the interactions between the incident ions and the substrate and the main theoretical approaches are summarized. Next, the three finishing methods presented in Fig. 1.2, which are all based on reactively driven ion beam etching are elucidated in more detail.
- In chapter 3 an explanation of the experimental set-up used for ion beam investigations with a short description of the materials is given. The surface error regimes significant for each specific ion beam etching method is defined. The analytical methods are briefly addressed.
- From chapter 4 onwards, the presentation and discussion of the experimental results begins. First, the effect of nitrogen and oxygen as processing gas at normal ion incidence on roughness evolution for ion beam figuring investigations is presented. The role of the alloy composition during ion machining is studied with a special focus on roughness evolution and local chemical composition.
- In chapter 5 and 6, the ion beam planarization technique with the aid of a sacrificial layer is considered. Mutual chemical and physical influences between substrate surface and ion beam irradiation are discussed. Next, the ion beam parameters are optimized and the results concerning the ion beam planarization process are discussed. The development of the aluminium surface during the planarization process is systematically investigated.
- In chapter 7, the developed process routes are transferred to a broad-beam Kaufman-type ion source.
- In chapter 8 the results of this work are comprehensively summarized to establish the connections between the ion beam etching procedure and the topography evolution within different spatial frequency regimes.
- A conclusion in chapter 9 presents the results obtained once again in a short form reduced to the essential findings and gives an outlook on relevant further questions.

# 2 Surface engineering with energetic ions

## 2.1 Ion target interactions during ion beam erosion

When a surface is bombarded with energetic ions, many processes can be initiated due to the collision of the incoming ions with the nuclei and electrons of the surface material atoms [38-41]. When the impinging ion encounters the surface, it can be backscattered, the ion may penetrate the surface and loose its energy until it gets trapped inside the solid structure, substrate atoms might be ionized or displaced from their lattice sites (recoil atoms). Additionally, electrons, and photons may be emitted. The process of removing near surface atoms from a condensed matter by direct momentum transfer in a collision cascade is called physical sputtering. A schematic sketch of ion target interactions is shown in Fig. 2.1.

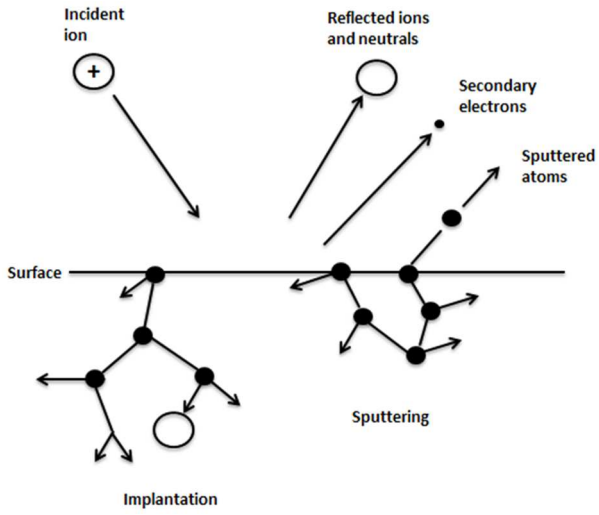


Fig. 2.1: Schematic ion target interactions, from Harsha [38]

Three main regimes are described depending on the type of displacement cascade, the single knock-on regime, the linear cascade regime and the spike regime [38-41]. In the single knock-on regime, the incoming ions are reflected by target material atoms and hit near-surface atoms, causing those recoil atoms to leave the surface if they receive sufficient energy to overcome the surface barrier [42]. In the linear cascade regime, a limited fraction of atoms is set in motion and recoil atoms from ion-target collisions receive enough energy to generate recoil cascades. In the spike regime, the density of recoil atoms is so high that the majority of atoms within a

certain volume are in motion. The linear cascade regime is the dominant regime during this study.

The dominant process is called knock-on sputtering with an elementary event, the atomic collision cascade, where the incoming ion knocks atoms off their equilibrium, leading to further collisions inside the material and leading to an eventually ejection of these atoms through the target surface [41]. The incident ion produces a cascade of recoil atoms along its path and loses energy when penetrating into the substrate material due to collisions with target atoms. The number of recoil atoms produced at any point is linearly proportional to the amount of energy lost by the incident ion at that point. The loss of energy of the incident ion on encountering a solid is typically divided into two categories, the electronic collision (inelastic) and nuclear collision (elastic) [38-41]. In the former category the incidence ion interacts with the electrons in the solid. As a result, inelastic collisions in form of electron excitation or ionizations of the atoms can occur. In the latter category the incoming ion interacts with the nucleus of the atom in the solid. Only the nuclear component of energy loss contributes to the production of energetic recoil atoms [38]. The nuclear collision results from repulsive Coulombic interactions. Depending mainly on the ion energy and the ion-target masses the ions travel a specific distance (ion range).

One characteristic parameter to describe the sputtering process is the sputter yield ($Y$), in principle determined as the number of ejected atoms per incoming ion [39-41]. The first elucidated principle features of the sputtering of metals was experimentally investigated by Wehner et al. [39,40]. They concluded, that the sputtering yield is a function of the atomic number of the bombardment material. The sputtering yield depends on the target species, the surface binding energy of the target atoms, energy, mass and the angle of incidence of the bombarding species and its nature. The crystallinity and the orientation of the target also influence the sputtering yield [38]. Many descriptions of the sputtering yield as a function of the ion incidence angle and the ion energy are given [41,43,44]. Yamamura et. al described the relative sputtering yield dependent on the ion incidence angle at a specific ion energy given by [44,45]:

$$\frac{Y(E_0,\theta)}{Y(E_0,0)} = x^f exp\left\{-\Sigma(x-1)\left[\frac{1-\sqrt{\frac{E_{th}}{E}}/x}{1-\sqrt{\frac{E_{th}}{E}}}\right]\right\} \quad \textbf{(1)}$$

where $E_{th}$ is the threshold energy, $E$ the ion energy, $x = 1/\cos\theta$ with θ being the ion incidence angle counted from the surface normal. Σ and $f$ are related to the angle of ion incidence for which the sputter yield has a maximum. The parameter $f$ incorporates threshold effects.

The sputter yield increases with increasing angle of ion incidence since the deposited energy distribution is shifted closer to the surface, reaching a maximum between 50-70°. The yield decreases rapidly for larger angles. The drop-off of the yield at glancing angles is thought to be caused by the increase of ion reflection from the target surface.

Above a critical value of ion energy, the sputter threshold energy, the sputtering yield increases with increasing energy reaching a maximum value. With further increasing energy, the sputtering yield decreases again due to the higher implantation depth of the incoming ions [39-41,46].

When the surface is bombarded by ions, a change in the surface topography and structure can result due to a number of causes. Sputtering is expected to retain an initially flat surface, which is free from imperfections, over time. However, the variation of sputtering yield with the angle of incidence of ions can bring about a change in the surface topography when the surface has unevenness. Since the erosion rate increases with increasing ion incidence angle, the surface topography may change when sputtering continues. During irradiation, dislocations, voids and stacking faults to the point of amorphization can occur, which lead to variations in sputtering yield and consequently contribute to changes of the surface topography. Additionally, impurities within the surface can give rise to locally different sputtering yields [38].

## 2.2 Ion beam finishing methods

During irradiation with energetic oxygen or nitrogen ions a temporally stable oxide or nitride passivation layer is formed, which is continuously eroded and simultaneously newly formed by ion implantation and results in a quasi-stationary layer thickness. The chemical modification during processing passivates structural and compositional inhomogeneities of the alloy matrix.

Hence, the oxide or nitride layer acts as a moderating etch front and preserves the initial surface roughness. [34,37].

From a technological point of view, reactive ion beam machining with oxygen is a rather slow process with an etch rate of about 0.17 $mm^3/h$, being 4-5 times lower than ion beam figuring with argon. Though, the roughness preservation during processing in comparison to IBF with argon, enables direct figure error correction of optical aluminium surfaces. Additionally, the process is stable without generating hazardous by-products, which makes the process clean.

Ion beam machining techniques available for finishing of optical aluminium surfaces are illustrated in Fig. 1.2 (chapter 1) and discussed in the following in detail.

## 2.2.1 Ion beam figuring

Direct figure error correction of optical surfaces using IBF is a well-established method due to the high accuracy [30,31,32]. For correction, an ion beam is used with a small diameter compared to the surface to be corrected. The application of reactively driven ion beam technologies is very promising for figure error correction of optical aluminium surfaces made of RSA Al6061 and RSA Al905 (see Fig. 1.2a).

In principle shown in Fig. 2.2, a dwell-time algorithm is applied to transfer the measured figure error data into a motion sequence. In particular, the surface errors are characterized and deconvolved with a removal function to create dwell-time instructions for the sub-aperture ion beam tool. Thus, the ion beam is scanned deterministically over the surface following the simulated motion profile. The path velocity of the ion beam over the surface results from a dwell time distribution proportional to the desired depth distribution of the material removal.

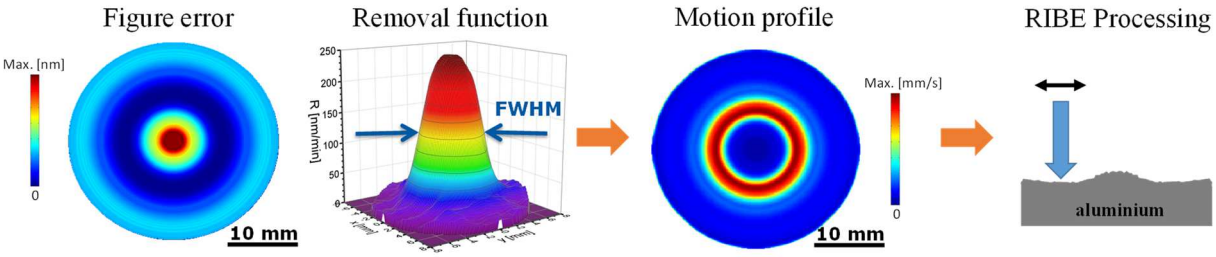


Fig. 2.2: Principle processing sequence for figure error correction method

For ion beam processing, oxygen or nitrogen gases are used. The erosion process is strongly dependent on the ion energy and the ion incidence angle since it is based on pure physical

sputtering. The results of the interaction of a low energy ion beam with the aluminium surface suggest the in-situ formation of a surface passivation layer with a thickness of about 13 nm over the entire surface, acting as a moderating etch front [34,37]. However, the process route is limited due to the inhomogeneous aluminium alloy composition and the resulting preferential sputtering.

### 2.2.2 Ion beam planarization

For applications in the short-wavelength VIS or UV spectral range it is necessary to improve the high-spatial frequency properties of the surface after SPDT. Originally, Johnson et al. proposed an ion polishing technique with the aid of a planarizing film to remove polishing scratches on fused silica [47,48]. As illustrated in Fig. 1.2b and Fig. 2.3a, the initial surface is covered with a planarizing layer of a specific thickness, so that the high-spatial frequency surface roughness features are fully embedded and surface waviness is levelled to a considerable extend. As a result, a smooth and planar surface is revealed. Depending on the initial surface quality, the thickness of the planarizing film typically ranges between some 100 nm and a few microns. Then, the plane surface is transferred into the underlying substrate by ion beam etching. To ensure an optimum surface transfer, the etch rates of the planarizing film and the aluminium substrate should be equal. The ratio of the etch rates between aluminium substrate and planarizing film is defined as the selectivity $S = R_{substrate}/R_{layer}$,

The volume etch rate of the photoresist layer $R_{layer}$ and aluminium substrate $R_{substrate}$ after RIBE processing at various etch depths d is calculated in consideration of the deterministic scan parameters as line velocity $v_y$, line feed $\Delta x$, and scan repetition count $N_{rep}$ as:

$$R = \frac{d \cdot v_y \cdot \Delta x}{N_{rep}} \qquad \textbf{(2)}$$

For an optimum process result, S needs to be 1. The selectivity is tunable by the experimental conditions, which differ for any material combination. But not any material combination allows the adjustment of S towards 1. The first limitation is given by the substrate material to be smoothed, since the initial surface quality and thus the surface errors to be corrected play an important role. Moreover, the volume etch rate for the specific experimental conditions, alloying elements and also the properties of the substrate like chemical composition or thermal

stability strongly influence the planarization procedure. Another important factor is choosing a suitable planarization layer. The properties of the planarization layer like chemical composition, thermal stability or layer thickness mainly influence the planarization process. Additional to the choice of materials, also the applied process technologies for layer coating have an impact. When the planarization layer is applied by spray coating, commonly a thinner layer is needed to embed the surface errors compared to spray coating.

Hence, to achieve a successful ion beam planarization, the process conditions have to be customized to the specific material combination [23,49,50]. In pure physical etching, i.e. ion beam sputtering, the etch rate strongly depends on the ion energy and the ion incidence angle. However, the scaling of the etch rate with respect to the ion energy behaves similar for most materials. In contrast, the specific characteristics of the ion incidence angle can be considerably diverse for different materials to be machined. So, for many material combinations there is a crossing in the incidence angle dependent etch rate characteristics, which is defined by the so-called planarization angle (see Fig. 2.3b). Thus, processing at the planarization angle $\Theta_P$ is one common solution to realize equal etch rates for both materials. This technique has been investigated for various material combinations, such as photoresist on diamond-turned copper [50], photoresist on diamond-turned nickel-phosphorous [23] and photoresist on silicon [51]. If the removal process is dominated by chemical ion-surface-interactions, the etch rate can be additionally adjusted by the process gas composition and the ion energy as well (see Fig. 2.3c). In ion beam processing with reactive process control there is a mixture of physically and chemically driven etch removal, so that extended degrees of freedom are available for process development. Those planarization processes are most effective in the waviness/roughness spatial frequency regime.

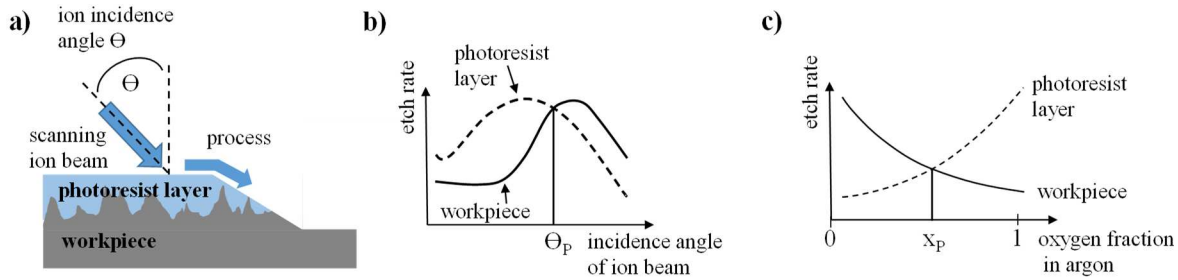


Fig. 2.3: Principle of a) ion beam planarization technique according to Johnson et al. [47,48]. Illustration of plane surface transfer of planarization layer into aluminium workpiece by ion beam machining. b) Dependency of etch rate for workpiece and coating material on the ion incidence angle. Planarization angle ($\Theta_P$) is marked as point of intersection for both curves. c) Etch rate dependency of photoresist layer and workpiece on process gas composition and resulting selectivity [107]

### 2.2.3 Ion beam smoothing

During ion beam smoothing, the ion incidence angle dependent sputter yield as a function of the local surface slope is adverted to reduce high spatial frequency errors in the microroughness regime (see Fig. 2.4a). The incoming ions are directed normal to the sample surface, where the sputtering yield is assumed to be a function of the local surface gradient (see Fig. 2.4b). Based on the RIBE machining process routine illustrated in Fig. 1.2a, a further development on direct smoothing of high spatial frequency errors using oxygen gas is suggested as schematically illustrated in Fig. 1.2c. The model scheme suggests, that surface areas with high slopes exhibit enhanced in-plane removal rates. As a result, surface roughness features with high slope border areas are gradually reduced in the progress of the ion erosion process [52-57].

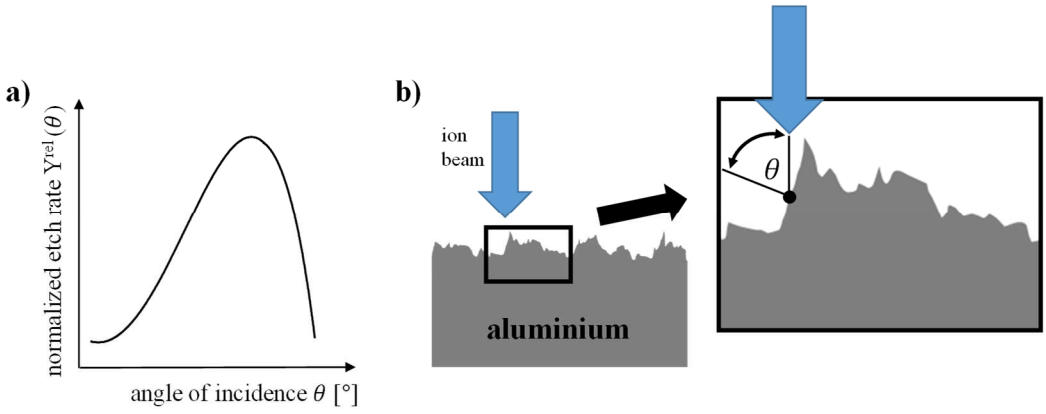


Fig. 2.4: a) Typical normalized etch rate dependent on the incidence angle of the incoming ions. b) Model scheme of local varying ion beam incidence angle on surface microroughness features. The roughness features are drawn enlarged

# 3 Experimental set-up and analytical methods

## 3.1 Experimental set-up

The experimental set-up used for ion beam machining investigations was developed at the IOM in the last years within the framework of the InnoProfile Transfer initiative [03IPT706X] "Ultra-precision manufacturing using atomic particle beams". For ion beam machining experiments, a high-vacuum (HV) vessel with a base pressure in the low $10^5$ Pa region was used. Several operating gases as argon, oxygen, nitrogen and fluorine containing gases like $CHF_3$ and $NF_3$ were provided. The schematic sketch of the set-up is shown in Fig. 3.1.

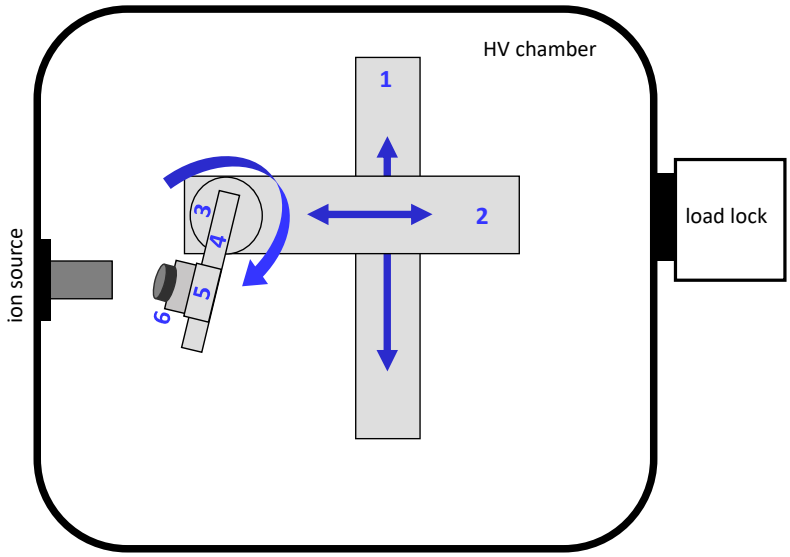


Fig. 3.1: HV vessel with load-lock chamber. The five-axis motion set-up for deterministic sample movement consists of a compensation axis a (1), the z-axis (2), x- and y-axis (4 and 5) enabling the movement of the sample holder (6) horizonal and vertical to the ion source. An additional rotational axis (3) enables the movement of the sample holder under different angles to the ion source

The load lock chamber enables the loading and unloading of samples without disturbing the ultrahigh vacuum inside the vessel. It contains a nitrogen feed line for gas flooding and a pumping system consisting of a booster pump and a turbo molecular pump.

**Motion set-up**

The five-axis motion set-up allows sample movement in front of the fixed ion source to scan the ion beam over the sample in a meandering pattern. The x- and y-axis ((4) and (5) in Fig. 3.1) enable the movement of the sample holder horizontal and vertical in front of the ion source.

With the additional rotational axis (3), z- and a-axis ((1) and (2)), a movement of the sample holder with incidence angles up to 67° and constant working distance is enabled. The x- and y-axis are individually selected and equipped with a stepping motor and an encoder.

**Sample holder**

The water-cooled sample holder is mounted on the five-axis motion system ((6) in Fig. 3.1). The water cooling ensures efficient heat dissipation from the sample reducing thermal effects during the process. The sample holder is additionally equipped with an integrated Faraday cup that permits in-situ spatially resolved ion beam current density analysis before and after each experimental run to determine the ion beam tool function and verify their stability (see photograph in Fig. 3.2a). The integrated Faraday cup is made of graphite with an opening diameter of 1 mm. Usually, the process conditions are chosen to obtain a Gaussian shaped tool function and thus can be characterized by the full-width at half maximum (FWHM) expressing the tool width and the integral beam current. After each process run, Faraday probe analysis was performed a second time to check possible changes during processing. An example of such a measurement is shown in Fig. 3.2b generated by 1.5 kV extraction voltage using nitrogen gas. The sample holder additionally enables the opportunity to add an aluminium mask with an opening diameter of 13 mm, defining a specific limited area for RIBE machining.

**TCP-type ion source**

The ion beam was generated by a 13.56 MHz transformer coupled plasma (TCP) type ion beam source. It consists of a cylindrical $Al_2O_3$ vessel surrounded by the RF coil. On the backside the process gas inlet is located. Inside the vessel a plasma discharge is ignited and maintained. The plasma comprises positively and negatively charged ions, electrons and neutrals. The ion extraction and beam formation are performed by a triple grid extraction system, allowing a constriction of the free-beam without use of an aperture [58]. The concavely shaped grids are made from graphite. The screen grid (G1) opening is 10 mm and the curvature radius is 150 mm. Due to the curvature of the grids, the ion beam exhibits a constricted region with the maximum point of constriction defining the working distance [58]. The beam energy is provided by the positive beam potential of the plasma anchor, which is situated near the process gas inlet and stays in direct contact with the plasma. The inner screen grid surface is in contact with the plasma too and thus is set to beam potential as well. During the investigations, the ion source is driven by reactive gases at beam energies $\leq$ 1.5 keV. The acceleration grid (G2) is

negatively charged. The deceleration grid (G3) is normally grounded and helps beam collimation reducing divergence of the beam and re-deposition of sputtered material back onto the accelerator grid. For ion beam machining investigations, the ion source is running at least one hour before the experiments to ensure stable process conditions. The schematic sketch of the ion source is shown in Fig. 3.2c and a photograph of the running ion source is shown in Fig. 3.2d.

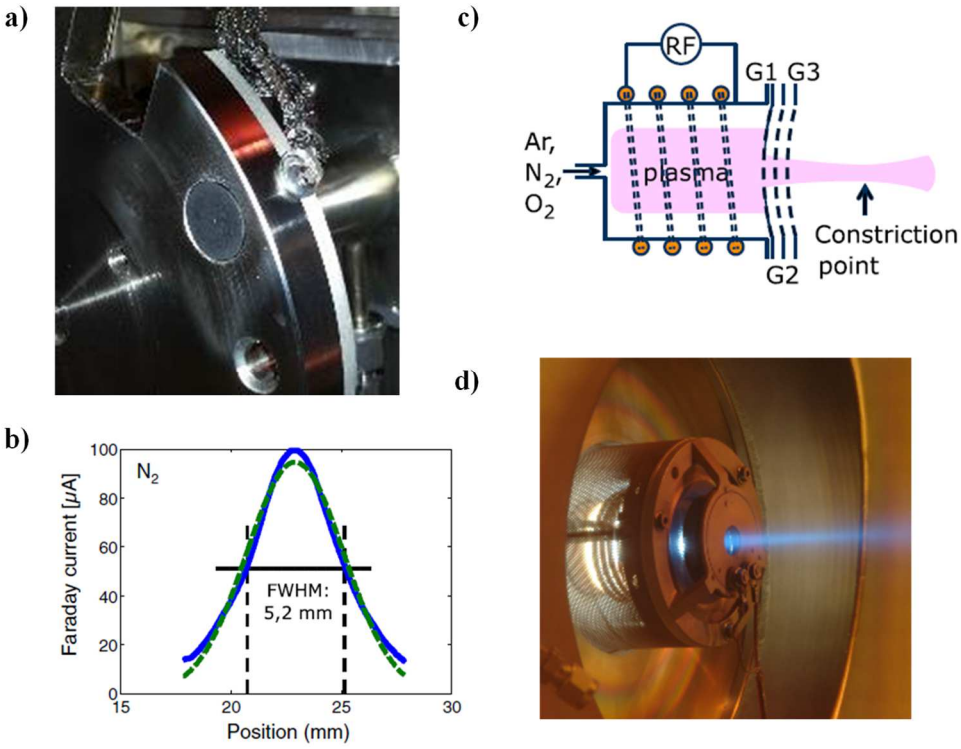


Fig. 3.2: a) Sample holder with integrated Faraday cup for in-situ beam analysis; b) Faraday probe measurement of 1.5 keV nitrogen ion beam; c) schematic illustration of TCP-type ion beam source with a photograph of the running ion source in d). Modified from [58]

### Motion sequence

The universal position control unit PS 90 (OWIS .GmbH) adapted to the computer was used to control positioning tasks for the motion sequences during RIBE machining [59]. Via closed-loop operation, the motion processor measures each current axis position via encoder, considering the temporal change of the position parameters due to the feedback signals. The movement of the sample to the ion source was controlled by manual configured program sequences via an operating software. During the study, the sample was moved to the ion source in such a way, that the ion beam is scanned in a raster path over the surface with constant velocity and line pitch within the defined machining area. Based on the ion beam tool function,

determined by Faraday probe measurements, precise sample positioning in front of the ion source with specific working distance was ensured. A specific material removal depth was implemented by increasing number of scanning repetitions. One single repetition includes the raster path scanning of the ion beam over the whole machining area. Thus, multiple repetitions define a specific material removal depth. For each repetition a mask border overrun in the order of about 1x beam FWHM of the scan area was conducted to ensure a planar etch profile inside the mask opening area.

## 3.2 Kaufman-type broad beam ion source

The ion beam finishing investigations are additionally transferred to an ion beam plant ISA200 (NTG Neue Technologien GmbH) employing a Kaufman-type (filament-based discharge) broad beam source. The schematic setup of a Kaufman-type ion source is shown in Fig. 3.3.

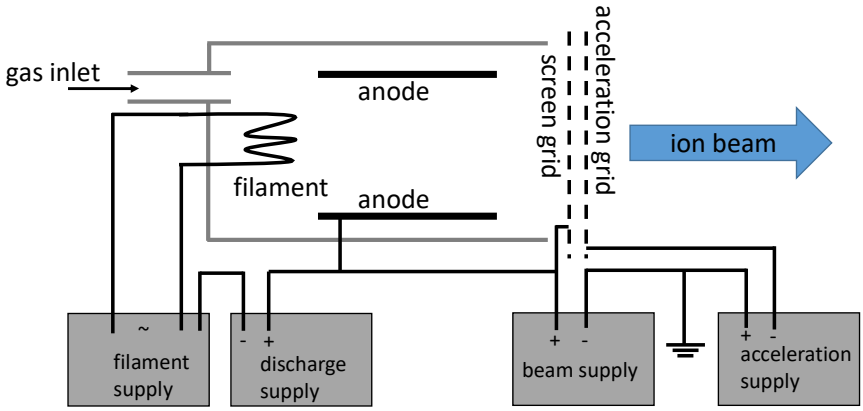


Fig. 3.3: Schematic sketch of hot filament Kaufman-type broad beam ion source after Zeuner et al. [60]

In principle, the process gas is fed into a hollow cylinder which is biased with a positive voltage and is the anode. The cathode is a filament subjected to a current. Due to this current the filament is heated up and emits electrons thermionically. The discharge voltage between the cathode and the anode accelerates the emitted electrons. The field of a permanent magnet confines the emitted electrons inside of a region within the chamber, where the process gas is ionized by electron impact [60 and reference therein]. A two-grid extraction system made from graphite with 180-mm grid opening was applied for the extraction of the ions. The average ion energy results from the sum of the discharge voltage (150 V) and the voltage of the screen grid (1350 V). The corresponding ion beam has a width of about 178 mm (FWHM) and the beam current was set to 70 mA. The working distance between sample and acceleration grid was

435 mm. Additionally, the sample was mounted on a rotating water-cooled (15 °C) sample holder.

# 3.3 Materials

## 3.3.1 Aluminium alloy materials

Aluminium as common engineering material is lightweight, ductile, low-cost and readily formable with outstanding optical properties. Aluminium has a face-centered cubic (fcc) structure and exhibits a high reflection coefficient even in the shortwave electromagnetic spectral range. The reflection coefficient ranges from the infrared spectral range to the shortwave visible and ultraviolet spectral range with values well above 90 %, marked by an absorption band at 800 nm, and therefore exceeds optical materials like gold silver or copper (see Fig. 3.4) [9,61]. The native oxide layer is immediately formed when the aluminium is exposed to air, but does not significantly deteriorate the reflectivity in the visible spectrum.

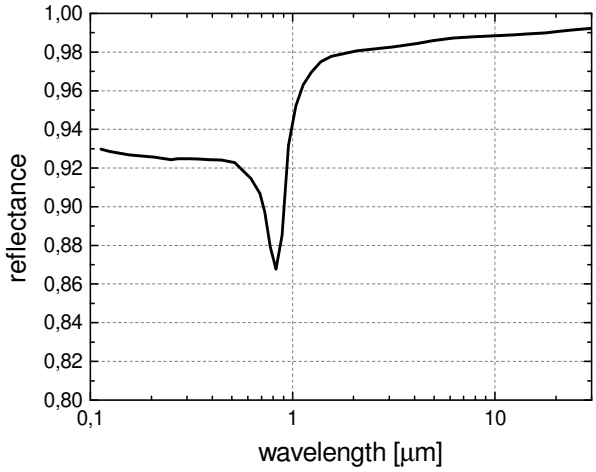


Fig. 3.4: Reflectance of aluminium, from Paquin [61]

Additionally, pure aluminium has both high thermal and electrical conductivity. However, aluminium has also a low elastic modulus and high thermal expansion [27]. To strengthen aluminium, alloying elements are added resulting in increased hardness, tensile strength and elastic modulus. As shown in Fig. 3.5, the dimensional change during precipitate heat treatment is small for Al6061 alloy, a significant shrinkage is observed for Al7075 and an expansion is seen for Al2014 [27]. In such polycrystalline materials, the structure is comprised of randomly oriented crystalline grains separated by grain boundaries, resulting in different mechanical properties for each crystallographic orientation [62,63]. Consequently, this behavior affects the

deformation introduced during SPDT and therefore small topographic variations of each crystal [62]. Standard Al6061 is a polycrystalline material with differences in crystallographic orientation that can cause differences in hardness and shear incompatibilities between neighboring grains resulting in grain scale roughening [2,64]. For increasing demands on optical surface quality, a new series of aluminium alloys is produced by RSP, developed by RSP Technology for TNO Science and Industry.

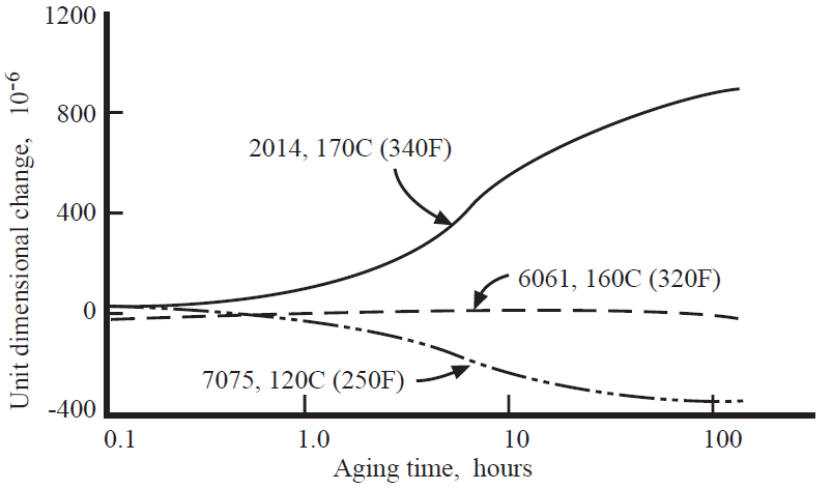


Fig. 3.5: Dimensional change as a function of time at the precipitation heat treating temperature employed to produce the T6 temper for three aluminum alloys, from Ahmad and Paquin [27]

During melt spinning, the highest cooling rates for producing aluminium alloys is possible. This technique provides an ultra-fine grained and homogeneous microstructure which results in reduced roughness values during SPDT [62]. A comparison of the surface measured by WLI with 5 x objective is shown in Fig. 3.6. Therefore, RSA materials are very promising for optical applications in the short-wavelength VIS and UV spectrum [2,65]. The production chain includes firstly melting and alloying, followed by melt spinning and chopping. The flakes are degassed and subjected to hot isostatic pressure processing to create a consolidated material [16,65].

Since former studies reveal enhanced etch pit formation during RIBE machining of RSA Al6061, a second alloy material RSA Al905, a so-called “second generation” aluminium, is tested [16,34] The alloy was found to form less etch pits with smaller sizes in the sub-micrometer range compared to RSA Al6061 [34]. The difference is mainly caused due to the chemical composition of the alloying elements. For RSA alloy materials, various compositions are known from literature. According to Gubbels et al., RSA Al6061mainly contains Mg, Si,

Cu, Fe and portions of Cr, Mn, Ti and Zr within the aluminium base [2]. In contrast, ter Horst et al. found a reduced composition consisting of Mg, Si and Cu within the aluminium base [16]. In contrast to RSA Al6061, the "second generation" alloy material RSA Al905 cannot be heat-treated and is dispersion hardened [16]. In the aluminium base of RSA Al905, mainly Ni, Cu, Fe and portions of Mn, Zr and Mo were found [16]. Since there seems no strict definition for the alloy composition, ToF-SIMS experiments were performed in positive mode (not shown here) revealing the following constituents beyond the surface region: Mg, Mn, Cr, Fe, Si and Ti, Cu, Ni and Zr portions within RSA Al6061 and Ti, Ni, Cu, Fe, Mn and Mg and traces of Cd, Mo, Zn, Zr, Cr and Si within RSA Al905. Apparently, there are deviations within the composition of RSA materials. Thus, an analysis in any development study is prerequisite. The experiments were performed on aluminium planar disc samples with 47 mm in diameter. Cleaning is carried out with isopropanol using an optical cloth prior to the experimental investigations.

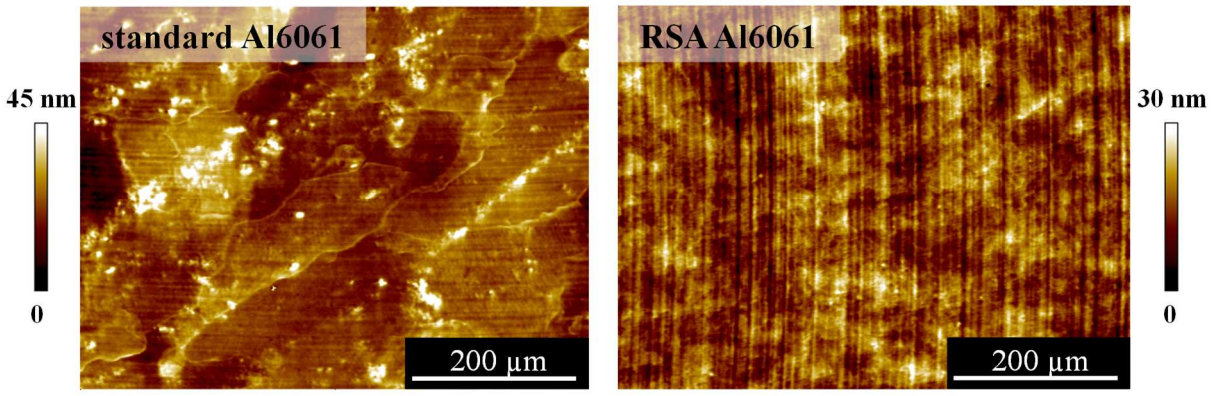


Fig. 3.6: WLI images (10 x objective) of standard Al6061 alloy in comparison to RSA Al6061

## 3.3.2 Photoresist materials as planarization layer

Polymer coatings reveal as an excellent choice for the ion beam planarization technique. For ion beam etching experiments, positive and negative working photoresist materials were analyzed. A photoresist in general describes a radiation-sensitive material that changes the chemical solubility during irradiation. In case of an increase in chemical solubility, the material is defined as positive tone photoresist. In contrast, negative tone photoresist materials are characterized by a decrease in chemical solubility during irradiation [66]. For the experimental investigations, conventional photolithography on a positive or negative tone photoresist layer was applied. For preliminary experiments, negative and positive tone photoresist materials were

tested in case of reproducibility, ion beam etching behavior, roughness evolution and chemical modification. The positive tone photoresist materials tested are ma-P 1205 [67], AZ 1505 [68] and mr-PosEBR0.3 [69]. Two types of negative tone photoresist materials, ma-N 405 [70] and ma-N 2405 [71] were also tested. Some selected properties of the used photoresist materials are summarized in appendix B.

## 3.4 Surface topography error regimes

Ion beam technologies are rather slow surface machining methods but offer a high degree of precision since the surface errors to be corrected are on the nanometer and subnanometer scale. The surface topography errors are specified by the spatial frequency range they occur in and the amplitude. Depending on their lateral dimension the surface errors are generally divided into three groups, the low-spatial frequency (LSF), mid-spatial frequency (MSF) and high-spatial frequency (HSF) errors [37,72,73] (see Fig. 3.7). The cut-off frequencies $f_f$ and $f_s$ strongly depend on the specific application including the applied wavelength of light. Standard cut-off frequency values are given in Deutsche Industrie-Norm ISO 10110-8:2012-02 as follows: $f_f = 400\ m^{-1}$ and $f_s = 400\ mm^{-1}$ with an ISO reference wavelength of 546.07 nm [74]. Consequently, the cut-off frequencies illustrated in Fig. 3.7 are marked as ranges [37].

Surface figure errors including deviations of the surface shape or form are LSF errors occurring below the cut-off frequency $f_f$. They cause classical aberrations in an optical image as distortions and can be corrected by deterministic sub-aperture finishing techniques such as MRF or IBF. Contrary, high-spatial frequency errors situated above the cut-off frequency $f_s$ are surface finish (or microroughness) errors causing a diffusive shine due to wide angle scattering [37]. In this spatial frequency region classical polishing techniques can be applied, IBP or direct ion beam smoothing. MSF errors are situated between HSF and LSF irregularities and are difficult to remove. Regular or irregular error features in the mid-to-high spatial frequency range are waviness and roughness. Prominent feature types are the turning marks from SPDT, which mainly result from the feed of the diamond tool. Additionally, superimposed oscillations resulting from mechanical vibrations (“chatter”) of the turning machine can also be observed on aluminium surfaces after SPDT [20 37,75]. However, those oscillations are situated in the MSF error range and cannot be corrected so far. Indeed, the turning mark features situated in the HSF range can be smoothed by ion beam planarization. Irrespective of the surface finish technique, caution is advised when choosing a surface machining method or process chain in

order to improve the surface in the specific frequency range as well as preserving the surface quality in the other spatial frequency ranges [37].

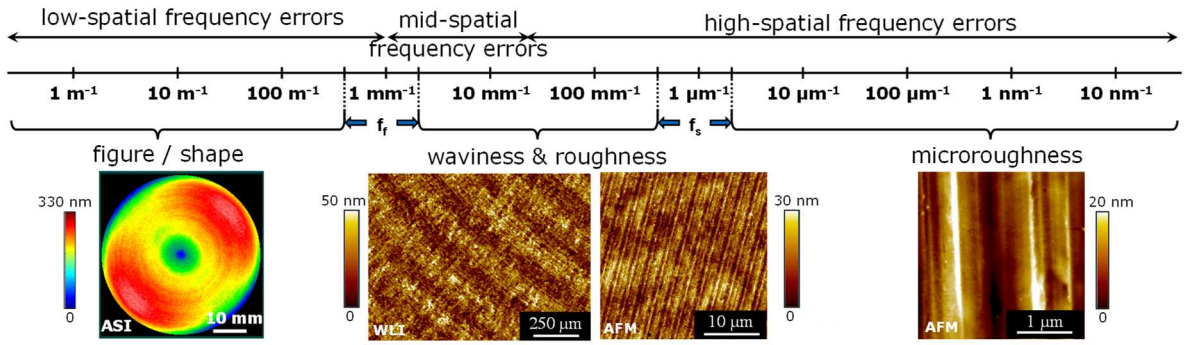


Fig. 3.7: Surface error types of optical surfaces depending on the spatial frequency range. From Bauer et al. [37]

# 3.5 Analytical Methods

## 3.5.1 Analysis of surface roughness

Investigations on the surface roughness in the mid-to-high spatial frequency range requires characterization methods with high resolution. By combining these methods, a broad spatial frequency range is intended to be covered to achieve information about the evolution of different surface feature types and to draw conclusions on the underlying beam-surface interactions.

### 3.5.1.1 White light interferometry (WLI)

Optical interferometry was used to determine surface roughness. It was performed using a Bruker NPFlex Optical Profiling microscope (Bruker NPFLEX$^{TM}$ 3D Surface Metrology System) using phase shift interferometry (PSI).

An interferometer is an optical device that splits a beam of coherent light exiting a single source (like a laser or LED) into two beams and then recombines them to create an interference pattern. The combined pattern can be analyzed to determine the difference in optical paths the two beams traveled [76]. The schematic imaging interferometer setup with a Michelson interferometer and a typical measurement of a single-point diamond turned aluminium surface is shown in Fig. 3.8.

The optical metrology module (OMM) contains a CCD camera and a multiple magnification detector (MMD) with field of view (FOV) lens tubes used for magnifying the objectives. A scanner assembly allows precise movement of the measurement objective. Dual LEDs with a filter flipper assembly provide illumination to the OMM. Light from the LEDs travels through the OMM and is reflected down to the objective by a beam splitter. After the light reaches the objective, another beam splitter separates the light into two beams. The reference beam reflects from a super smooth reference mirror in the objective, while the test beam reflects from the surface of the sample and back to the objective. If the surface of the sample is in focus, the two light beams recombine and form an interference pattern of light and dark bands (fringes). The number of fringes and their spacing depend on the optical path difference between the test beam and the reference beam. If reference and sample are parallel, only one large fringe appears (in this case the fringes are said to be nulled). The interference pattern is imaged by the CCD camera and the signal is transferred to the computer where it is processed via Vision64™ operation and analysis software. Vision64™ produces a graphical output display representing a contour map of the sample's surface [76,77].

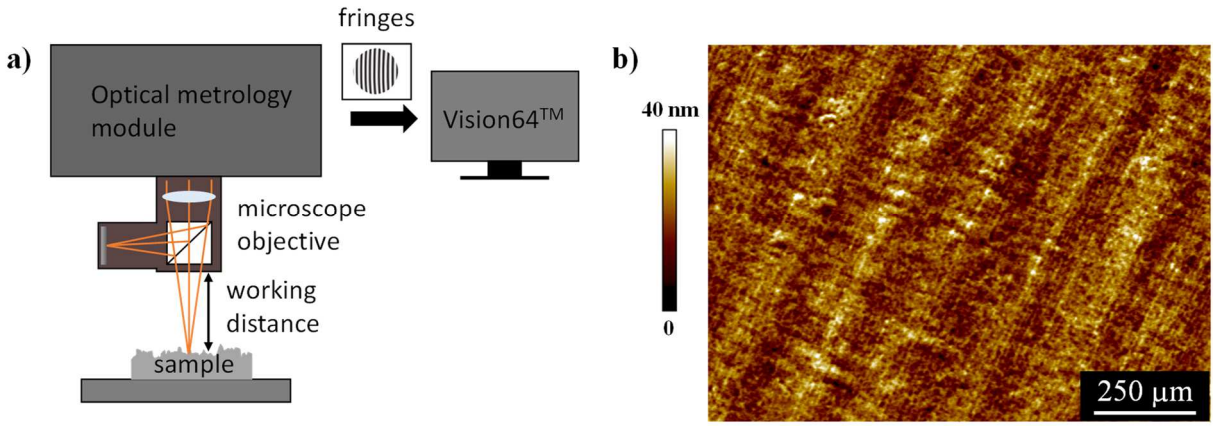


Fig. 3.8: a) Schematic measurement method for a 5 x objective in NPFlex™ with a Michelson interferometer and b) an example of the surface topography of a single-point diamond turned aluminium sample measured with a 5 x objective

Two basic measurement modes are available at the system. During a PSI measurement, a mechanical translation system precisely alters the optical path length of the test beam. Each optical path change causes a lateral shift in the fringe pattern. The shifted fringes are periodically recorded by the camera, producing a series of interferograms. Computerized calculations then combine these interferograms to determine the surface height profile [76,77]. Vertical scanning interferometry (VSI) uses a broadband light source and is effective for

measuring objects with rough surfaces and those surface height topographies up to several millimeter amplitude. Indeed, it yields precision in the nanometer range rather than in the sub-nanometer range (as does PSI). Additionally, VXI interferometry combines PSI and VSI for high-resolution characterization of both smooth and rough surfaces in a single measurement. Since the investigated aluminium mirror surfaces are very smooth with roughness values in the low nanometer range, in this work PSI is used with the NPFlex system only.

For measurements, objectives with 5 x and 10 x magnifications were used with 1 x field of view multiplier in PSI mode. The image sizes were 1230 µm x 925 µm and 624 µm x 467 µm, respectively, with a pixel resolution of 640 x 480. In contrast to the described schematic measurement method for a 5x objective in NPFlex$^{TM}$ with a Michelson interferometer, the 10x objective is based on Mirau type interferometer. Although the two objectives differ in the arrangement of the optical components, the general functional principle is the same. In both cases, the incident light is divided into a measurement beam and a reference beam. With the Mirau interference objective, a beam splitter plate and a reference mirror are located in the optical beam path.

### 3.5.1.2 Atomic force microscopy (AFM)

Atomic force microscopy (AFM) is a well-established high-resolution technique to analyze the surface of a wide range of materials, i.e. hard or soft, conducting or non-conducting surfaces without special preparation. AFM is one type of Scanning probe microscopy (SPM). During all analysis methods of SPM, a sharp force-sensing probe tip at the end of a cantilever is physically interacting with the surface building a three-dimensional height or topography map. In general, three types of imaging modes of the sample surface are used in AFM: contact mode, non-contact mode and ‘intermittent’ or tapping mode [78,79].

The ‘intermitted contact mode’ (‘tapping mode’) is deployed, where an oscillating signal is generated and applied mechanically to the cantilever. Usually, a laser beam is reflected by the back side of a reflective cantilever onto a four-segment photodetector (see Fig. 3.9).

The cantilever is oscillating typically close to its resonant frequency with large vibrational amplitude applied without any contact to the surface. When the tip (mounted on the cantilever) is brought close to the sample surface, the oscillation changes due to repulsive forces and the driven oscillation of the cantilever is attenuated resulting in a decrease in amplitude and the

reflected light path changes [79]. While scanning the tip over the surface in a raster-like pattern in x- and y-direction, the cantilever oscillation is continuously measured by monitoring the change in light detected by the four quadrants of the photodetector [79]. The detected change in oscillation is used in a feedback loop to maintain the probe-sample interaction constant by correcting the voltage applied to a piezo element controlling the z-position of the cantilever. Thus, the change in vibration amplitude is equivalent to a specific height of the sample surface. Therefore, for each x-y-position the relative z-signal is measured, and each grid point is represented by a specific pixel. The measured height-signal is represented in a respective brightness value.

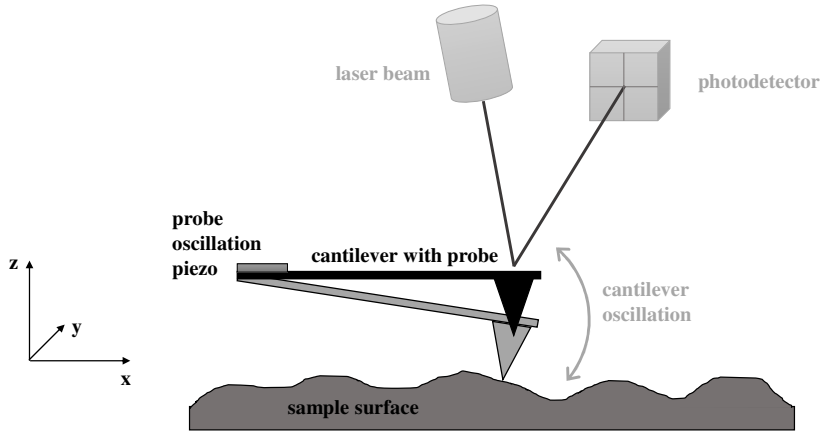


Fig. 3.9: Schematic drawing of the basic operation principle of an atomic force microscope. The measuring setup is located in a sound-insulated enclosure that is located on a vibration-decoupled foundation

The measurements were performed using a Dimension ICON in tapping mode™ from Bruker in a xy closed loop configuration. The cantilevers are 160 µm long, 40µm wide and 3.7 µm thick with an aluminium reflex coating on the backside. The Si tips are 9 - 19 µm in height with maximum 10 nm tip radius (typical value 7 nm). The cantilever resonant frequency is typically 300 kHz and the spring constant 26 N/m. Special attention was given to prevent artifacts in the measurements. Scanning areas of 3 µm x 3 µm, 10 µm x 10 µm and 35 µm x 35 µm were measured with a pixel resolution of 1024 x 1024.

The raw image height data was subjected to a plane correction consisting of a global plane fit and a line-wise correction. In this routine, a fitted polynomial function of the 3rd order is subtracted from each line of the image. Each line is therefore centered on zero height. For the AFM image processing, the Scanning Probe Image Processor (SPIP™) software version 6.0.14 by Image Metrology was used [80].

### 3.5.1.3 Power spectral density (PSD) analysis

For technological applications, surface roughness is an important property. A first order statistics to describe the roughness of a sample surface is given by the RMS roughness. The results of different types of measurements made on the same sample converted to this common quantity can generally differ due to the spatial frequency bandwidth limits of the instrument used in order to gain information on the spectral content of the surface topography.

The measured image can be converted from the spatial domain into the frequency space using a two-dimensional Fast Fourier transform (2D-FFT) operation. When a 2D-FFT of the measured height map is performed, information about dominant frequencies can be obtained. From the 2D-FFT, the power spectral density (PSD) function is provided, which decomposes a surface into contributions from different spatial frequencies [37,81,82]. Consequently, quantitative information about the height and lateral distribution of surface error features is given. The PSD represents the spatial frequency spectrum of the surface roughness measured in inverse-length units. Mathematically, the PSD is the Fourier transform of the autocorrelation function of the signal, which contains the power across the spatial frequency range [81,82]. The two-dimensional PSD is the averaged of the Fourier transform magnitude squared:

$$PSD\left(f_x, f_y\right) = \frac{1}{L^2}\left|\int_{-L/2}^{L/2}\int_{-L/2}^{L/2} h(x,y) \times exp\left[-2\pi i\left(f_x x + f_y y\right)\right]dxdy\right|^2 \quad \textbf{(3)}$$

where the PSD variables $f_x$ and $f_y$ are the spatial frequencies of the surface roughness and are related to the periodicity of the surface features, $h(x,y)$ are the surface topography data and L is the length of the measured window [81].

A self-written MATLAB® script was employed for angular integration resulting in the isotropic PSD function by obtaining angular averaging over all spatial frequencies with constant distance. For direct aluminium machining the measurements were performed five times under the same conditions but at different positions to calculate an average PSD function. For each instrument (AFM and WLI) a certain range of surface spatial frequencies were measured. Different scanning areas were chosen for each instrument. Additionally, measuring the same sample at different positions with similar parameter is more representative as long as the surface topography exhibits a homogeneous structure. The PSD functions of all measurements can be combined with two important conditions fulfilled: 1) measurements with different spatial

frequency ranges should partially overlap and 2) within the overlapping regions, the PSD functions should merge [81]. Statistical roughness values $R_q$ (or RMS) are obtained from the area beneath a band-limited part of the PSD function and can be calculated from the isotropic PSD data via:

$$R_q(t) = \sqrt{\int_{f_{min}}^{f_{max}} 2\pi f \times PSD(f,t)df} \quad \textbf{(4)}$$

with the integral boundary limits $f_{max}$ and $f_{min}$ defining the overall measured frequency range of 0.0024 µm$^{-1}$ – 34.7 µm$^{-1}$ corresponding to a spatial wavelength range of 416.7 µm – 0.0288 µm employed in this work. RMS roughness values were additionally calculated in the spatial frequency ranges of 0.0024 µm$^{-1}$ – 1.7 µm$^{-1}$ for waviness/roughness and 1.7 µm$^{-1}$ - 34.7 µm$^{-1}$ for microroughness regime. In Table 3.1 the spatial frequency ranges for sample topography measurements by AFM and WLI are summarized. Since each measurement technique is limited in image size and resolution, the specific spatial frequency ranges of each partial PSD were restricted and are not equivalent to the whole spatial frequency range of each image data.

Table 3.1: Image sizes and spatial frequency ranges for sample topography measurements by AFM and WLI

| | Image size | Spatial frequency range |
|---|---|---|
| AFM | 3 µm x 3 µm | 1.67 µm$^{-1}$ – 34.7 µm$^{-1}$ |
| AFM | 10 µm x 10 µm | 0.478 µm$^{-1}$ – 19.96 µm$^{-1}$ |
| AFM | 35 µm x 35 µm | 0.0857 µm$^{-1}$ – 7.31 µm$^{-1}$ |
| WLI | 624 µm x 467 µm | 0.00481 µm$^{-1}$ – 0.120 µm$^{-1}$ |
| WLI | 1230 µm x 925 µm | 0.00243 µm$^{-1}$ – 0.0786 µm$^{-1}$ |

An example of a typical PSD function of an aluminium surface after SPDT is shown in Fig. 3.10, consisting of AFM measurements with scan sizes of 3 µm x 3 µm and 35 µm x 35 µm, as well as WLI images with scan sizes of 1230 µm x 925 µm and 624 µm x 467 µm, respectively.

The bump at about 0.0035 µm$^{-1}$ – 0.008 µm$^{-1}$ (I) corresponds to error features located in the MSF range. These periodic structures are characterized by a period of average 180 µm and are schematically illustrated in the WLI image with 5 x objective inside the inset in Fig. 3.10. They originate from mechanical vibrations of the machine during SPDT resulting in periodically superimposed oscillations [20,74]. Additionally, the turning marks located in the spatial frequency range of about 0.3 µm$^{-1}$ – 3 µm$^{-1}$ (II) result from the tool feed with a periodicity of 2.5 µm, corresponding to the PSD deviation at 0.4 µm$^{-1}$. Several superstructures corresponding

to the PSD deviations at 0.8 µm$^{-1}$, 1.2 µm$^{-1}$, 1.6 µm$^{-1}$, 2.0 µm$^{-1}$, 2.4 µm$^{-1}$ also represent periodically turning mark structures with $\frac{1}{2}$, $\frac{1}{3}$, $\frac{1}{4}$, $\frac{1}{5}$, and $\frac{1}{6}$ multiples of the initial periodicity. Superstructures may also result from mathematically analysis, but in the shown example they are actually present on the surface.

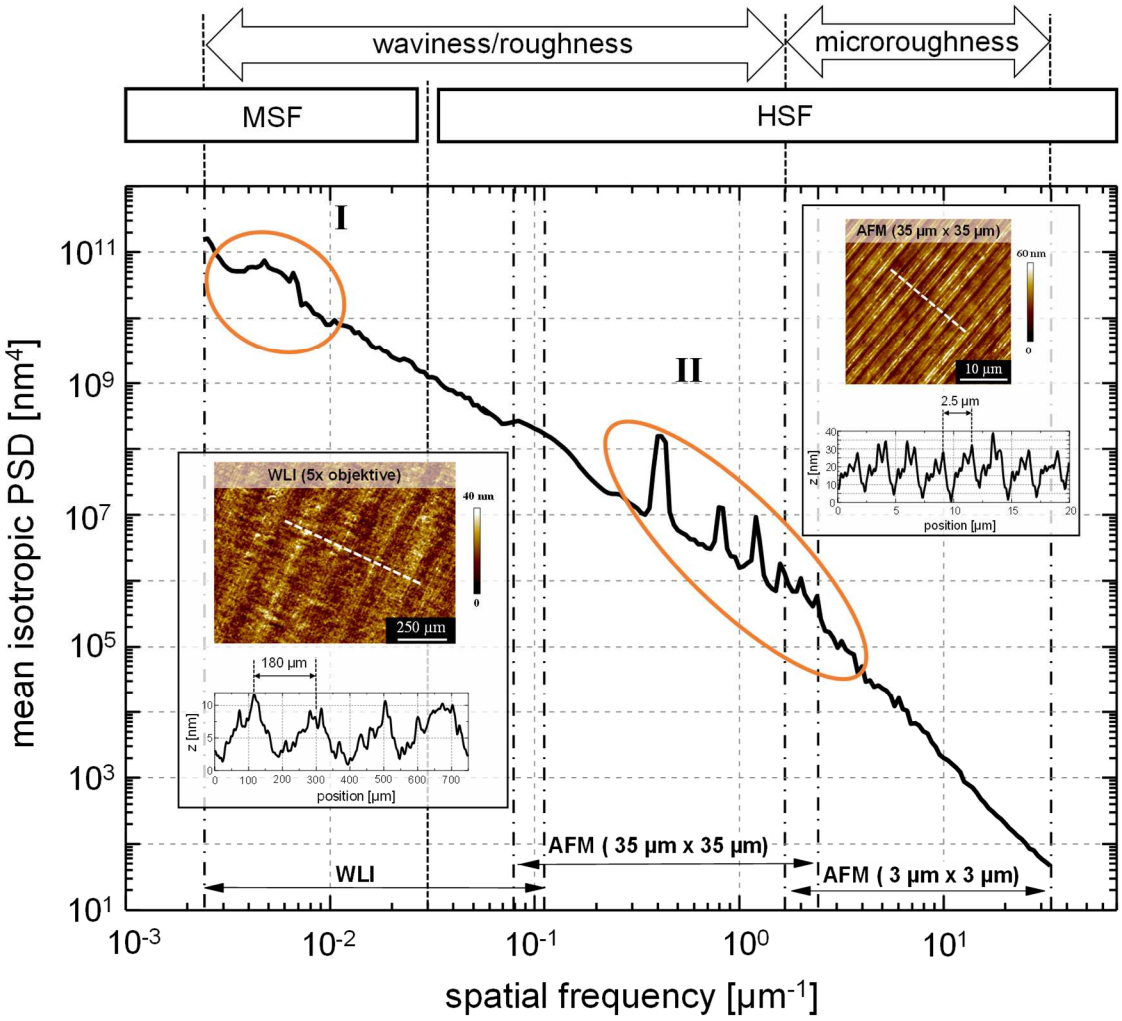


Fig. 3.10: PSD function of a typical aluminium RSA Al905 surface after SPDT. The orange marked bump (I) in the PSD corresponds to waviness in the MSF region illustrated with the inset of a WLI image in this spatial frequency range and a cross section. The second orange marked peaks (II) correlate with the turning marks observed in the AFM image and illustrated cross-section

### 3.5.2 Scanning electron microscopy with energy-dispersive X-ray spectroscopy (SEM-EDX)

In scanning electron microscopy (SEM), a focussed electron beam is scanned over the surface with an acceleration voltage of 0.1 kV - 30 kV. During interaction of the electron beam with

the sample surface, especially secondary electrons, backscattered electrons and X-rays are emitted. For imaging mainly secondary electrons are used which originate from near-surface regions and provide information about the surface topography. The emitted secondary electrons are gathered by an Everhart-Thornley or an in-lens-detector. The signal is enlarged and used for imaging. The result is a qualitative height information. The contrast is produced in a way that areas that are inclined to the detector are imaged brighter than averted areas [83]. An integrated feature of SEM instrument is energy-dispersive X-ray (EDX) analysis. This technique is used for local material elemental composition analysis up to about 3 µm depth. This technique is used to create element composition maps over a broad scanned area. When the sample is bombarded by the SEM's electron beam, electrons are ejected from the atoms comprising the sample's surface. The resulting electron vacancies are filled by electrons from a higher state, and an X-ray photon is emitted to balance the energy difference between the two electrons' states. The X-ray energy is characteristic of the element from which it was emitted. The detector is typically a lithium-drifted silicon, solid-state device. The X-ray photons detected by energy dispersive detectors generate peaks in the EDX spectrum which position is element specific [83,84]. A typical SEM-EDX mapping of a RSA Al905 surface is shown in Fig. 3.11.

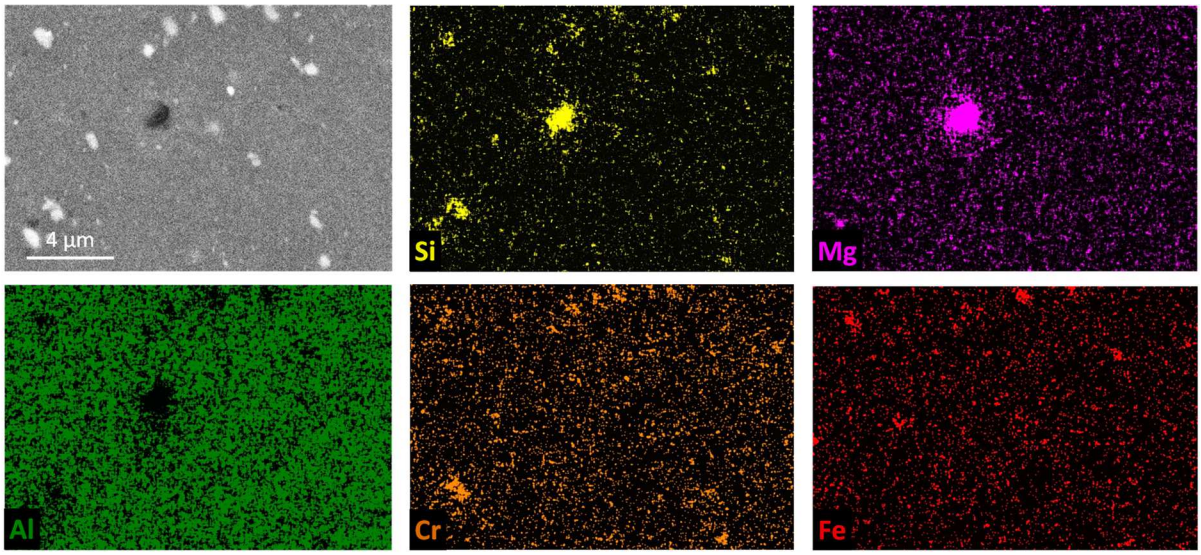


Fig. 3.11: SEM and SEM-EDX mapping image of an aluminium RSA Al905 alloy separated into Si (yellow), Mg (pink), Al (green), Cr (orange) and Fe (red)

Surface composition mapping of aluminium samples is performed by SEM-EDX measurements in a Zeiss Gemini Ultra 55 machine with a Bruker XFlash 3001 detector. A beam voltage of 15 kV, a beam aperture of 60 µm, and a working distance of 7.2 mm are applied.

### 3.5.3 X-ray photoelectron spectroscopy (XPS)

X-ray photoelectron spectroscopy (XPS), also known as electron spectroscopy for chemical analysis (ESCA), is an analytical method to determine quantitative atomic composition and chemistry of a solid's outer surface within the first 10 nm. Elements from Li on are detectable with this method, if the element of interest exists at >0.05 atomic percent, except for He and H, which are not detectable due to the extremely low photoelectron cross sections [85]. The surface is irradiated with monochromatic X-rays, whereas the energy of the detected electrons is analyzed. This method is based on the photoelectric effect, i.e., emission of electron following excitation of core level electrons by photons (see Fig. 3.12).

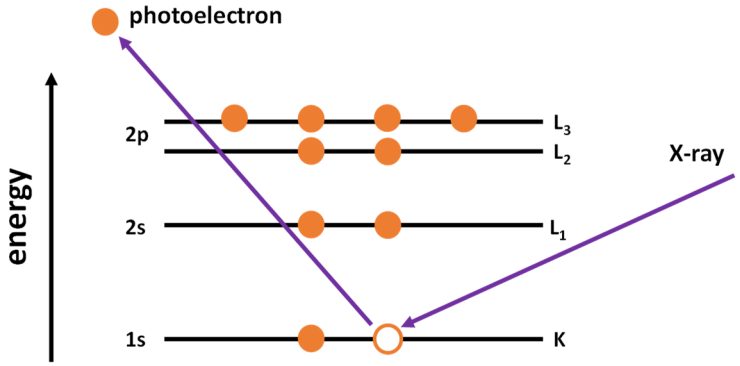


Fig. 3.12: Schematic example of the photoelectron process with the various electronic energy levels

Additionally, one of the two primary de-excitation processes that follows photoelectron emission, is the Auger process. Since also Auger de-excitation results in electron emission, peaks from both photoelectrons and Auger electrons are observed in XPS spectra. The generated photon is transferring the whole energy to the electron during interaction. If the energy transfer is sufficient, the electron is emitted from the atom/ion as well as the solid to a detector. Quantitatively measured is the kinetic energy that remains on the emitted electron which is a function of the electron binding energy and is specific for an element within the sample volume. The resulting kinetic energy is:

$$E_{kinetic} = E_{photon} - (E_{binding} + \Phi) \quad \textbf{(5)}$$

with $E_{binding}$ is the energy of an electron attracted to a nucleus, $E_{photon}$ is the energy of X-ray photons being used by the spectrometer, and $\Phi$ is the spectrometer work function, a correction factor for the instrument and correlates to the minimum energy required to eject an electron

from an atom [85,86]. XPS was performed with a Kratos Axis Ultra DLD system. In this work, monochromatic Al-$K_\alpha$-radiation with an energy of 1.486 keV was used to excite the photoelectric effect. To increase the photoelectron yield, an electrostatic lens combined with a magnetic immersion lens was used. The photoelectron detection and the determination of its kinetic energy was realized by a hemispherical analyzer with a channel plate secondary electron multiplier at a pass energy of 160 eV and 40 eV, respectively. The XPS spectra obtained in this way were then adjusted and evaluated using the Unifit software [87]. By showing the energy of electrons emitted from a material, XPS allows for the composition of a material to be determined [85,86].

### 3.5.4 Time of flight- secondary ion mass spectrometry (ToF-SIMS)

Secondary ion mass spectrometry (SIMS) is an analytical technique with high sensitivity enabling the detection of very low concentrations of trace elements. The surface is irradiated with primary energetic ions resulting in the formation of secondary ions during the sputter process in ultrahigh vacuum (UHV). A most precise SIMS technique is time-of-flight secondary ion mass spectrometry (ToF-SIMS).

To characterize surfaces with ToF-SIMS, a high-energy ion beam is required first and rastered over a square region to form a flat beam crater. These so-called primary ions are shot at the sample surface, transferring their energy in elastic shocks to the atoms of the sample, impacting a collision cascade within the first 5 to 10 nm of the sample surface. The charged particles leaving the sample are called secondary ions. The secondary ions with the desired polarity are then collected with a time-of-flight mass spectrometer and detected according to their mass-to-charge ratio. In order to ensure that the secondary ions enter the flight path simultaneously, the primary ion beam is pulsed [88]. In pulsed operation bunches of primary ions are focussed onto the sample surface. The secondary ions are extracted in a static electrostatic field into a time-of-flight analyzer which is equipped with a reflectron to double the flight path in the ToF column. The mass resolution, primarily depending on the flight time $\tau$ via $m/\Delta m = \tau/2\Delta\tau$, reaches values of 1:5000 up to 1:12000 with respect of the ion mass in the spectrum. The ion detection is equipped with a micro-channel plate for gaining the signal and a silicon detector with a scintillator screen. Thus, a high dynamic range of 5 orders of magnitude is achieved. This technique can provide mass spectral information and allows depth profile information.

The principle setting of a ToF-SIMS is shown in Fig. 3.13a. SIMS imaging is accomplished through the use of finely focused ion beams or by preserving the spatial relationship of emitted ions through suitable secondary ion optics [88-90]. The primary $Ga^+$ ion gun generates a focused ion beam which is directed to the sample surface at an angle of 45° [91]. The ions are applied to the sample with an energy of 15 keV, reaching a sample current of about 25 nA in direct current (continuous operation) mode and about 1.0-3.0 pA in pulsed operation mode. The primary ion gun is intended only for the generation of secondary ions for analysis [92]. The knocked out secondary ions are bundled with the extraction electrode (extractor) in the desired polarity and fed into the flight tube. Via an ion mirror, which further extends the flight path for better resolution, the ions reach the detector, where they are finally registered according to their mass-to-charge ratio. An additional ion gun, the so-called sputter gun, is required for sample removal for depth profile analysis.

It has two different ion species that can be used to sputter the sample surface. On the one hand, $O_2^+$ ions can be selected as sputter species, which are generated by electron impact ionization. On the other hand, a thermionic caesium ion source can be used with $Cs^+$ ions as sputter species. The energy of the ions can be varied from 250 eV to 2 keV, whereby currents of 30 - 90 nA ($Cs^+$) and 90 - 250 nA ($O_2^+$) on the sample surface are reached. The $Cs^+$ sputter source is used to obtain secondary ions with predominantly negative polarity. For secondary ions with positive polarity, $O_2^+$ is selected as sputter species [88,93]. Most ToF-SIMS devices today also have an electron gun to compensate for the sample charge that occurs during bombardment with primary ions. All components are located in an ultrahigh vacuum chamber with a residual pressure of approximately $10^{-9}$ mbar.

Time-of flight secondary mass spectrometry (IONTOF;TOF SIMS 5) is used for depth profiling of the sample composition in the near surface region. Qualitative composition analysis of RSA samples is performed in positive mode. For sputtering, a 1 keV $O_2^+$ ion beam with about 250 nA beam current is used. The aluminium near-surface region is examined in negative mode, for which a 0.5 keV $Cs^+$ ion beam with about 45 nA beam current is applied for depth sputtering. The analysis is done by a 15 keV $Ga^+$ ion beam, while the analysis scan field of (50 × 50) $\mu m^2$ is centered within the (300 × 300) $\mu m^2$ sputter crater. The depth calibrations are provided by WLI analysis of the sputter crater depths. An example of ToF-SIMS depth profiling analysis is shown in Fig. 3.13b. The oxide and nitride layer thickness were determined as the distance of the surface to the depth, where the signal is decreased to its half maximum value.

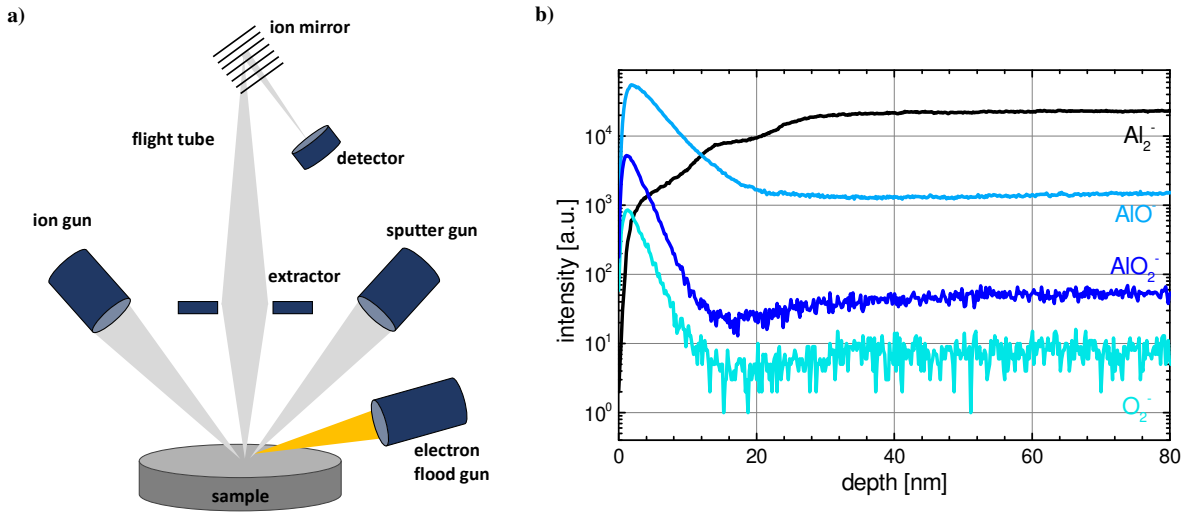


Fig. 3.13: a) Measurement principle of a TOF-SIMS and b) schematic depth profiling of a RSA Al905 surface showing typical $Al_2^-$, $AlO^-$ and $O_2^-$ - signals

## 3.5.5 Reflectometry

The photoresist thickness was measured using a thin film analyzing system (Mikropack NanoCalc 2000). Thin layers up to several hundred micrometer thickness can be analyzed with this technique. However, the layers need to be partially transparent for the incoming light and the refraction indices for substrate and layer have to differ. The optical thin film measurement technique analyzes the light-interference caused by thin layers. Utilizing the reflectance method, one common analytical method for thin films, the amount of reflected light from the thin film is measured, with the incident light normal to the sample surface. The reflection at the layer surface and layer substrate interface results in constructive and destructive interference depending on the wavelength of the light. To determine the layer thickness, a sample layer model with the material-specific spectral dielectric film properties is modelled by a best-fit algorithm to match the measured reflection spectrum. Additionally, the reflectivity characteristic of the aluminium surface is determined with this technique in the wavelength range of 400 – 800 nm. The reflection spectrum is analyzed at five different sample positions to calculate an average reflectance curve. A single-side polished p-type Si-(100) sample is taken as reference. To adjust the illumination light intensity, an untreated aluminium surface is measured under the same conditions.

## 3.5.6 Photoresist composition

### 3.5.6.1 Attenuated total reflection infrared spectroscopy (ATR-IR)

The chemical composition of the photoresist layers was analyzed via IR spectroscopy, specifically mid-infrared (MIR) spectroscopy, using the tendency of these materials to absorb light in the infrared wavelength range [94,95]. Between 14000 – 4000 $cm^{-1}$ the near-IR region is situated, the mid-IR region between 4000 – 400 $cm^{-1}$ and the far-IR region between 400 – 10 $cm^{-1}$. IR spectroscopy involves the study of the interaction of radiation with molecular vibrations via changing its vibrational state. This interaction of light and matter is a resonance condition involving the electric dipole-mediated transition between vibrational energy levels. The vibrational bands are characterized by their frequency, intensity and band shape, providing a "fingerprint of a particular molecule analyzed since the vibrational energy levels are unique to each molecule. The IR spectrum is obtained by plotting the intensity of absorbance or transmittance versus the wavenumber, which is proportional to the energy difference between the ground and excited vibrational states. For energy to be transferred from the IR photon to the molecule via absorption, the molecular vibration must cause a change in the dipole moment of the molecule. The excitation of vibrational modes of the molecules are represented via peaks in an IR spectrum, associated with various chemical bonds and functional groups. Complex molecules may have many oscillation possibilities, differentiating valence oscillations (bond length change) and deformation oscillations (bond angle changes) in plane or out of plane. Taking symmetry into account, symmetrical and asymmetrical oscillations are distinguished [95]. The emitted light is collected and focused onto a wavelength-dispersive Fourier transform instrument [95].

The basic equipment consists of a commercial IR spectrometer and suitable reflection accessory for internal (total) or external reflection. Attenuated total reflection (ATR) is part of internal reflection. ATR uses the evanescent wave existing at the interface of the IR waveguide and the sample. The internal reflection element (IRE) in the light path used is germanium. Due to the non-absorbing IRE medium the electromagnetic wave penetrates the interface to the absorbing analysis specimens evanescent wave [96,97]. The photoresist layers with thicknesses of about 500 nm were coated on p-type silicon (100) wafer. Since silicon is non-absorbing, no spectral interference occurs, so that any absorption of the evanescent wave is due to the photoresist thin

film. However, since thin monolayers are close to the detection limits, grazing angle attenuated total reflection (GAATR) with variable angle ATR accessories exhibits sufficient sensitivity to analyze the thin photoresist layers [98].

For analysis of the thin photoresist layers, MIR spectroscopy using a Bruker IFS 55 (FT-IR) armed with 64° GAATR accessory (Harrick VariGATR™) with a coupled MCT detector was used. The incidence angle of 64° is greater than the critical angle to enable total internal reflectance [95]. The measuring principle, based on the principle of Maxwell's theory [99], is shown in Fig. 3.14a. The resulting typical spectrum is shown in Fig. 3.14b. Vibrational bands located below 1500 $cm^{-1}$ are characteristic for the specific molecule. This so-called "footprint-region" is one main section of an IR spectrum. The second main section situated above 1500 $cm^{-1}$ are absorption bands that can be assigned to individual functional groups. The frequencies of the stretching vibrations generally follow the rule, that with increasing bond strength between two atoms the oscillation frequency in the spectrum is higher. Accordingly, triple bonds absorb at higher wavenumbers than double and single bonds.

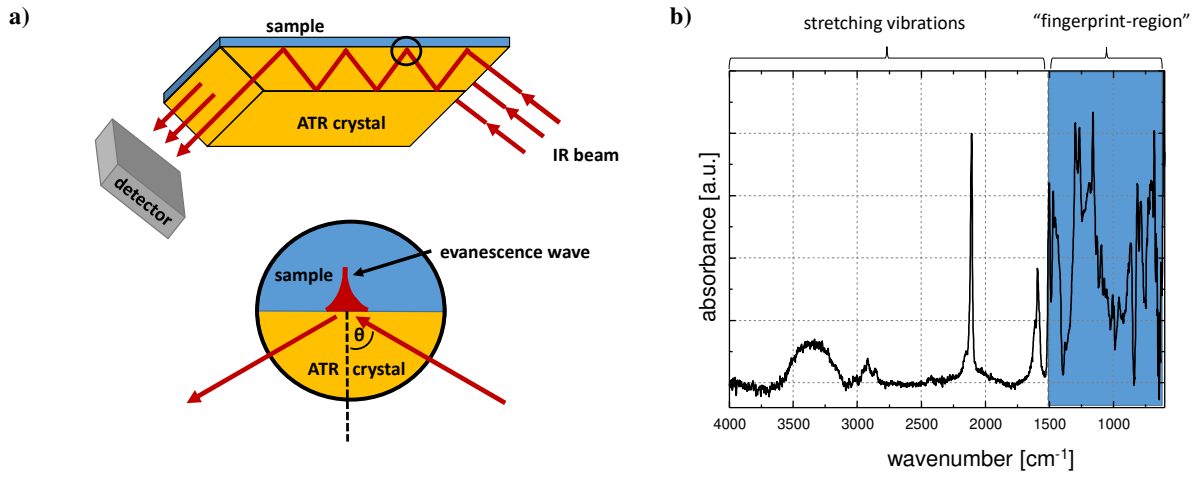


Fig. 3.14: a) Measurement principle of ATR IR spectroscopy and b) schematic IR spectrum of the negative tone photoresist ma-N 2405 with two main spectrum sections marked

### 3.5.6.2 Thermogravimetric analysis (TGA)

Thermogravimetric analysis (TGA) is a method for primarily investigating the thermal stability, compositional properties and oxidative stabilities of substances. For this purpose, a precisely weighted sample is placed in an open crucible on a sensitive balance and heated or cooled in a controlled atmosphere. The mass of the sample is monitored continuously depending on time and/or temperature. The controlled temperature program is either isothermal or non-isothermal.

In isothermal TG, the chosen temperature is mainly constant over the time. In non-isothermal TG the temperature changes, commonly linearly over time resulting in a constant heating rate. The graphical representation of the sample mass relative to the initial mass in percentage as a function of temperature or time (the so-called thermogram) characterizes mass gain or mass loss processes. Thermal processes resulting in weight gain are attributed to adsorption or oxidation reactions, whereas weight loss processes are results of i. a. decomposition, reduction reactions, desorption or dehydration [100,101].

For a more detailed analysis of particular mass loss and mass gain processes, the derivative thermogram (DTG) and the TG curve data are usually coupled. The DTG curve is extracted via deriving the weight data as a function of temperature or time, representing specific mass loss and mass gain regimes by downward and upward peaks, respectively. The peak onset point gives a characteristic initiation temperature for each mass change mechanism. The peak of the first derivative indicates the point of greatest rate of change on the curve [100,101]. Within this study, TGA was performed with a Perkin Elmer model Pyris 1 instrument. The measurements were executed in nitrogen atmosphere at a heating rate of 20°C/min in the temperature range of room temperature to 800 °C. A typical TG and DT analysis of a ma-N 2405 photoresist is illustrated in Fig. 3.15. The location of each peak onset and the peak temperature are marked via dashed lines.

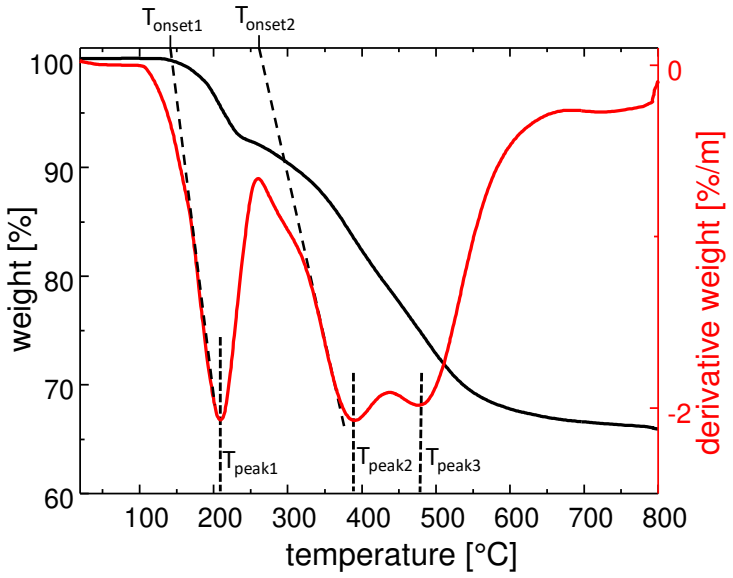


Fig. 3.15: Typical thermogravimetric analysis (black) of negative tone photoresist ma-N 2405 and the corresponding first derivative thermogram (red) of the TG function

### 3.5.6.3 Differential scanning calorimetry (DSC)

Differential scanning calorimetry (DSC) is a universal method to investigate phase transitions and structural changes generated via a heat flow change leading to local temperature difference along its path. According to Höhne et al. DSC is defined as "*the measurement of the change of the difference of the heat flow rate to the sample and to a reference sample while they are subjected to a controlled temperature program*" [102]. DSC curves are therefore obtained as the differential rate of heating against temperature. The area under a DSC peak is directly proportional to the heat absorbed or evolved by the thermal event, and integration of these peak areas yields the heat of reaction [103].

Two basic types of DSCs are distinguished, the heat flux DSC and the power compensation DSC. Both types combine a differential method of measurement but differ in design and measurement principle. In particular, the measured quantity is compared with a quantity of the same kind of known value and in which the difference between the two values is measured. The measured signal is proportional to a heat flux rate $\phi$ which allows the observation of the time dependence of a transition on the basis of the $\phi$(t) curve [102]. In heat-flux DSCs or single-furnace DSCs, both materials are heated at the same rate from a single heating source in one furnace. In power-compensation DSC or double-furnace DSC, two identical independent small furnaces measure sample and reference individually. In both furnace a heater and temperature sensor are present.

Power-compensation DSC analysis was performed with a Perkin Elmer model DSC 8500 in this study. The measurements were executed in nitrogen atmosphere at a heating rate of 10 C / min. An illustration of the schematic setup of a power-compensation DSC and a typical DSC thermogram of the negative tone photoresist ma-N 2405 is shown in Fig. 3.16. The sample and reference are kept at the same temperature using individualized heaters and the parameter recorded is the difference in power. The furnaces are controlled by two control loops, the average temperature control loop and the differential temperature control loop. The average temperature control loop delivers equal power to sample and reference sides, whereas the differential control loop is designed to minimize the temperature difference between the sample and reference positions. In appearance of a transition, the differential control loop will supply differential power to control the energy of the sample reaction [102,103].

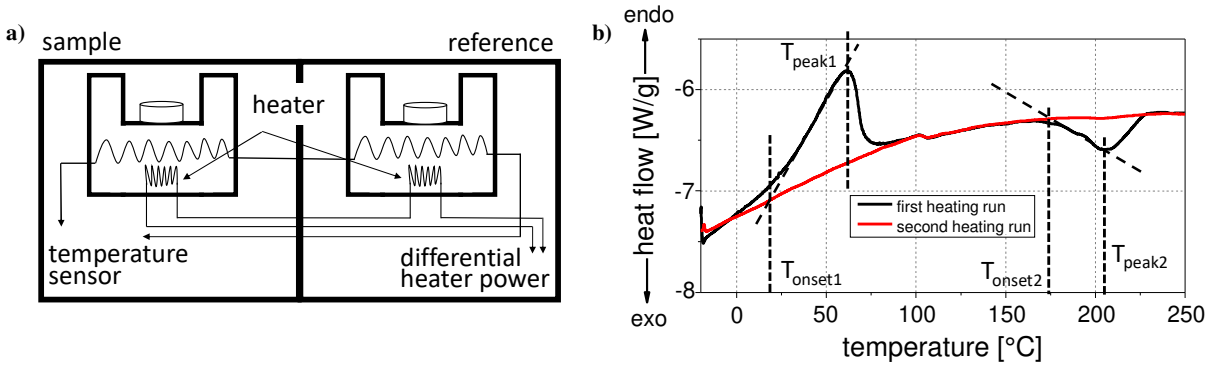


Fig. 3.16: a) Schematic setup of a power-compensation DSC with an example of a DSC thermogram of ma-N 2405 photoresist layer shown in b)

The reactions occurring in a DSC thermogram can be exothermic or endothermic. Exothermic reactions are attributed to crystallization, oxidative decomposition, curing or cross-linking, whereas endothermic reactions are mainly melting, boiling, vaporization, sublimation, desolvation, chemical degradation or solid-solid phase transitions [103]. Unfortunately, the use of power compensation DSC results in endothermic reactions being displayed as positive events, a situation which is counter to IUPAC recommendations [103].

The coupling of DSC and thermogravimetric measurements is of particular importance. The combination of both methods enables information about changes in heat flow rate and heats of transition combined with information about whether volatile components are involved and which change in mass is attributed to a transition.

### 3.5.6.4 Gas chromatography coupled mass spectrometry (GC-MS)

Gas chromatography coupled mass spectrometry (GC-MS) is an analytical method combining two features – gas chromatography and mass spectrometry- to identify different substances within one test specimen. In gas chromatography, the mobile phase is a carrier gas, usually an inert or non-reactive gas and the stationary phase is a microscopic layer of polymer or liquid on an inert solid support inside glass or metal tubing. The gas chromatography portion separates different components of a sample specimen by vaporizing and swiping onto this so-called capillary column by the carrier gas. The compounds comprising the mixture of interest are separated by virtue of their relative interaction with the coating of the column. The latter part of the column passes through a heated transfer line and ends at the entrance to ion source where compounds eluting from the column are converted to ions. The mass spectrometer identifies and quantifies the chemicals according to their mass-to-charge ratio [104]. Two potential

methods exist for ion production. The most frequently used method is electron ionization (EI) with electrons of typically 70 eV kinetic energy and the occasionally used alternative for selective ionization is chemical ionization (CI) [105]. For the present study, EI was used. When sufficient energy is impacted on neutral molecules, outer shell electrons are removed and positive molecular ions ($M^+$) are produced. The resulting peak from this ion can be seen in a mass spectrum. Due to the large amount of energy impacted to the molecular ion it fragments and further smaller ions with characteristic abundances are produced that provide a so-called fingerprint of the molecular structure. This information can be used to elucidate the structure of unknown mixtures and identify compounds of interest [106]. GC/MS measurements were performed with an Agilent 5973 series. The measurements were conducted in vacuum at a scanning rate of 10 °C/min in the temperature range of 45 °C to 310 °C.

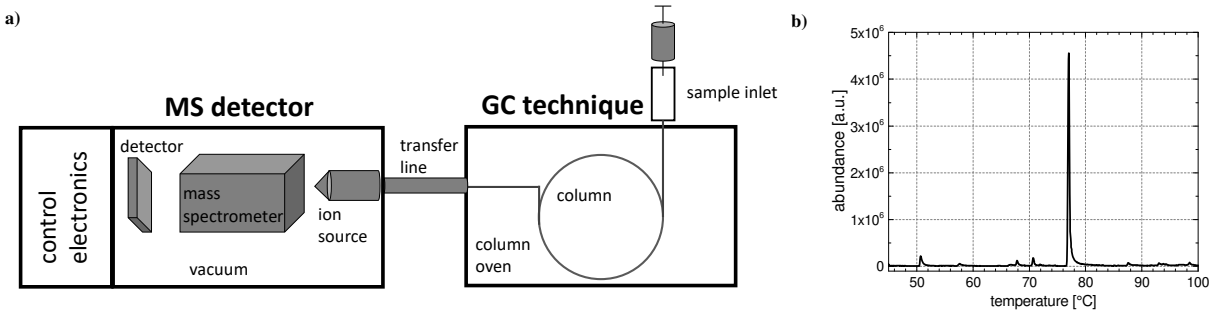


Fig. 3.17: a) Schematic diagram of a GC-MS setup with an example measurement focusing on the organic solvent of negative photoresist ma-N 2405 detected over temperature shown in b)

# 4 Surface engineering by reactive ion beam etching

During reactively driven ion beam machining of RSA Al905 with pure oxygen process gas with the purpose of figure error correction, the initial surface roughness is mainly preserved. PSD analysis of Al905 before and after oxygen machining revealed almost no increase in roughness and waviness in the spatial frequency range of 0.0035 $\mu m^{-1}$ – 2.4 $\mu m^{-1}$ after 400 nm depth etching, turning into a moderate degradation after 1 µm material removal [34,37]. In contrast, residual surface degradation caused by the formation of a series of etch pits and domain pattern structure was obtained in the spatial frequency range of 0.0035 $\mu m^{-1}$ – 2.4 $\mu m^{-1}$ due to the heterogeneous precipitate structure within the aluminium bulk material [34,37]. An extension of the reactively driven ion beam figuring model scheme of optical aluminium surfaces using nitrogen process gas is examined in the following. Note that most of the following content has been submitted and is currently under review [107] [108] or is ready for submission [109].

## 4.1 Reactive ion beam etching with nitrogen

Ion beam machining investigations at normal ion incidence were performed with $N_2$ at 1.5 keV beam energy. The ion beam is scanned in a raster path over the surface with a constant velocity of 4 mm/s and a 1 mm line pitch with multiple repetitions within the defined machining area. For investigations in section 4.1.2, the etch depth is determined by an increased number of scan field repetitions with a constant velocity of 5 mm/s and a 1 mm line pitch. The corresponding ion beam parameters are summarized in Table 4.1.

Table 4.1: Ion beam process parameters and corresponding etch rates of RSA Al905 and RSA Al6061 (index[1]) In the second section (index [2]) ion beam machining investigations for the purpose of quantitative comparison of increasing material removal depth with almost retained ion beam processing parameter is presented

| Material | Process gas | Process pressure [Pa] | FWHM [mm] | Beam current [mA] | Etch rate [$mm^3/h$] | Etch depth [nm] |
|---|---|---|---|---|---|---|
| RSA Al905[1] | $N_2$ | 3.8 x $10^{-3}$ | 9.9 | 1.9 | 0.54 | 300 |
| RSA Al6061[1] | $N_2$ | 1.5 x $10^{-3}$ | 9.0 | 1.9 | 0.68 | 230 |
| RSA Al905[2] | $N_2$ | 8.0 x $10^{-4}$ | 7.1 | 4.30 | 0.88 | 49 |
| | $N_2$ | 8.0 x $10^{-4}$ | 7.2 | 4.54 | 0.88 | 196 |
| | $N_2$ | 8.0 x $10^{-4}$ | 7.1 | 4.36 | 0.89 | 492 |
| | $N_2$ | 8.0 x $10^{-4}$ | 7.2 | 4.34 | 0.91 | 1006 |
| | $N_2$ | 8.0 x $10^{-4}$ | 7.2 | 4.40 | 0.99 | 1998 |

### 4.1.1 Dependence of the aluminium alloy composition

Fig. 4.1 shows AFM topography images and the calculated PSD functions of RSA Al905 and RSA Al6061 samples before and after $N_2$ RIBE processing.

The surface topography of RSA Al905 is generally dominated by 2.4 µm spaced turning marks with an initial height of (23.3 ± 1.9) nm corresponding to the strong deviation in the PSD spectra at 0.4 $\mu m^{-1}$ with several superstructures at 0.8 $\mu m^{-1}$, 1.2 $\mu m^{-1}$, 1.6 $\mu m^{-1}$, 2.0 $\mu m^{-1}$ and 2.4 $\mu m^{-1}$ (see Fig. 4.1). These superstructures observed in the PSD spectrum result from the periodical turning mark structure present on the surface. They might indicate an imperfection in the cutting tool shape used during SPDT [110,111]. Additionally, a bump in the PSD spectra at about 0.006 $\mu m^{-1}$ corresponds to 167 µm spaced periodicity resulting from chatter, i.e. mechanical vibrations of SPDT machine [20,74]. During $N_2$ RIBE machining of about 300 nm material removal, the PSD curve is increased in the short-wavelength range above 2.6 $\mu m^{-1}$. Surface bumps and pits are formed resulting in a slightly increased microroughness of (4.2 ± 0.5) nm rms compared to (3.8 ± 1.2) nm rms before RIBE machining (see Fig. 4.1a). Below 1.5 $\mu m^{-1}$ the PSD deviation after RIBE is almost negligible. The full range roughness of (9.9 ± 2.3) nm rms is largely preserved during processing. With a resulting height of (16.3 ± 1.3) nm after RIBE machining, the turning marks are reduced to some extent but besides the formation of etch pits with sizes in the sub-micrometer range is observed (see Fig. 4.1a).

In contrast, ion beam irradiation of RSA Al6061 causes surface degradation during 230 nm material removal. The PSD spectrum is increased in the spatial frequency range above 0.15 $\mu m^{-1}$. Below 0.15 $\mu m^{-1}$ both PSD curves merge (see Fig. 4.1b). Similar to RSA Al905, surface degradation in the microroughness regime is observed leading to (3.4 ± 1.0) nm rms after machining compared to the initial value of (1.3 ± 0.6) nm rms. The largest deviation of approximately 1 - 1.5 orders of magnitude is obtained in the high frequency range above 10 $\mu m^{-1}$ which is a result of the formation of a granular structure with sizes below 100 nm. In the range between 1 $\mu m^{-1}$ and 10 $\mu m^{-1}$ there is a deviation in the order of 0.5 - 1 dec resulting from pit and particle formation with individual sizes of several hundred nanometers. The turning marks are still apparent with smoothed edges but comparable depth. As a consequence, the waviness/roughness increases to (6.1 ± 1.1) nm rms compared to the initial value of (4.9 ± 0.9) nm rms.

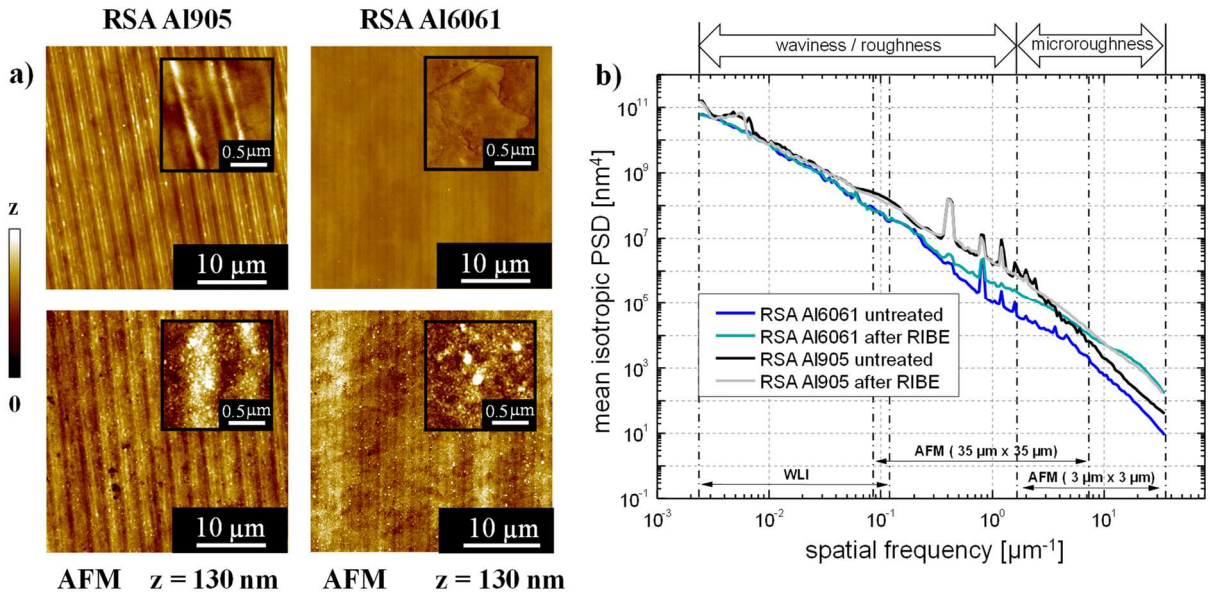


Fig. 4.1: a) AFM measurements of RSA Al905 and RSA Al6061 samples before (top) and after (bottom) $N_2$ RIBE machining at normal angle. The etching depths for both process runs are 300 nm for RSA Al905 and 230 nm for RSA Al6061. The insets in the AFM measurements show the roughness evolution of surface topography on 1.5 µm x 1.5 µm scan size. The z range of the insets is 20 nm. b) PSD function calculated on the basis of AFM and WLI measurements [107]

To further analyze the effect of RSA Al6061 surface degradation, the local composition distribution after RIBE machining was monitored by SEM-EDX mapping (see Fig. 4.2). ToF-SIMS experiments performed in positive mode (not shown here) reveal the following constituents beyond the surface region: Mg, Mn, Cr, Fe, Si and Ti, Cu, Ni and Zr portions.

The particles formed on the surface are mainly due to Cr, Fe, Si and partially Ti fractions (see Fig. 4.2). Significant Si and Mg fractions are found together within the etch pits. In particular, $Mg_2Si$ precipitates are reported to be formed during the initial alloy annealing procedure causing etch pits [34,63,112]. Due to the inhomogeneous matrix structure of Al6061 alloy, the formation of pits is promoted resulting from preferential sputter erosion [34].

Contrary to RIBE investigations with RSA Al6061, the etch pit formation on RSA Al905 is less pronounced with sizes mainly in the sub-micrometer range. This effect might be favored due to the different alloy constituents within the aluminium matrix. RSA Al905 mainly contains Ni, Cu, Fe and portions of Mn, Zr and Mo [16] instead of Mg and Si, which are assumed to mainly cause the observed etch pits.

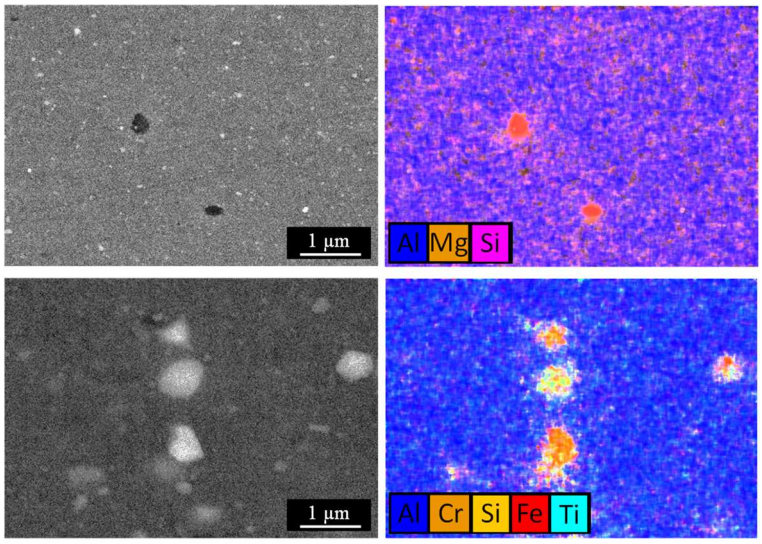


Fig. 4.2: SEM and SEM-EDX mapping image of a nitrogen processed aluminium RSA Al6061 sample after 300 nm etch depth revealing mainly Si and Mg precipitates within the etch pits and Si, Cr, Fe, Ti in the remaining nanogranules [107]

Since the $N_2$ RIBE investigations after removing 300 nm material are most promising, the forthcoming investigations are addressed to increasing material removal depths for the RSA Al905 alloy.

## 4.1.2 Ion beam etching of Al905

Reactively driven ion beam machining was performed on a RSA Al905 sample with gradually increasing machining depths up to 2000 nm at normal ion incidence. The experiments were performed within a defined machining area limited by an aluminium mask at different positions on the sample. Fig. 4.3 illustrates the roughness evolution analyzed via WLI and AFM measurements and the corresponding PSD functions. The effect of RIBE machining on surface roughness segmented into waviness/roughness and microroughness is summarized in particular in Table 4.2 and the corresponding spatial frequency ranges are marked in Fig. 4.3. For a more detailed discussion of turning mark evolution, averaged cross section profiles are generated by defining an average area for the cross-section line. Within this area, about 300 parallel cross-sections are averaged. The positions for the midline of the cross section profiles illustrated in Fig. 4.4a are represented by solid lines in the AFM images in Fig. 4.3b.

The untreated aluminium Al905 surface is characterized by turning marks with a period of 2.5 µm corresponding to the peak at 0.4 $\mu m^{-1}$ with several superstructures at 0.8 $\mu m^{-1}$, 1.2 $\mu m^{-1}$, 1.6 $\mu m^{-1}$, 2.0 $\mu m^{-1}$ and 2.4 $\mu m^{-1}$ in the PSD function (see Fig. 4.3). The spatial wavelength

range, where the turning marks are situated, is illustrated enlarged by means of an inset in Fig. 4.3a. During nitrogen processing, the PSD function in the spatial frequency range below 3 $\mu m^{-1}$ remains almost unchanged up to 500 nm material removal. However, with increasing material removal, the PSD peaks corresponding to the turning mark structures are continuously decreased and almost completely disappeared after 2000 nm material removal (see Fig. 4.3a).

Table 4.2: Surface roughness of aluminium Al905 divided into microroughness and waviness/roughness, respectively, as well as the full range roughness

| RSA Al905 | Machining depth [nm] | Microroughness [nm rms] | Roughness + waviness [nm rms] | Full range [nm rms] |
|---|---|---|---|---|
| Untreated | | 3.8 ± 1.2 | 9.5 ± 1.7 | 10.2 ± 2.3 |
| RIBE $N_2$ | 49 | 4.3 ± 0.8 | 9.6 ± 1.5 | 10.6 ± 1.7 |
| | 196 | 4.1 ± 0.4 | 8.5 ± 1.2 | 9.6 ± 1.2 |
| | 492 | 4.2 ± 0.5 | 9.3 ± 1.3 | 10.2 ± 1.4 |
| | 1006 | 4.4 ± 0.7 | 9.8 ± 0.8 | 10.9 ± 2.0 |
| | 1998 | 4.2 ± 0.5 | 12.2 ± 0.7 | 12.9 ± 1.8 |

One exception is the bump at 0.4 $\mu m^{-1}$ corresponding to the 2.5 µm spaced turning marks (see Fig. 4.3 and Fig. 4.4a). Hence, the turning marks are gradually smoothed and the turning mark height decreases with increasing material removal. Consequently, the turning mark height decreases to about (14.6 ± 1.3) nm after 500 nm removal compared to the initial height of (23.1 ± 2.1) nm. However, with increasing material removal of 1000 nm and 2000 nm, the turning mark height is marginally further decreased to (14.1 ± 1.6) nm and (11.1 ± 2.3) nm, respectively. This might be caused by a contrary process of increased surface degradation due to enhanced etch pit formation resulting in an increased PSD function in the spatial frequency range where the turning marks are situated. Consequently, the PSD deviations corresponding to the turning mark seem to be superimposed by the surface degradation.

Additionally, the PSD spectrum is increased in the spatial frequency range above 2.5 $\mu m^{-1}$ up to maximum one order of magnitude, which is related to the formation of nanoscopic granules already observed in section 4.1.1. Thus, the microroughness is marginally increased after 50 nm removal to (4.3 ± 0.8) nm rms compared to (3.8 ± 1.2) nm rms of the untreated surface. Note that the surface structure is already formed within the first 50 nm material removal and hardly changes with increasing material removal depth. Though, additionally larger particles are formed after 200 nm removal but no significant change is observed up to 2000 nm depth (see Fig. 4.4b and Table 4.2).

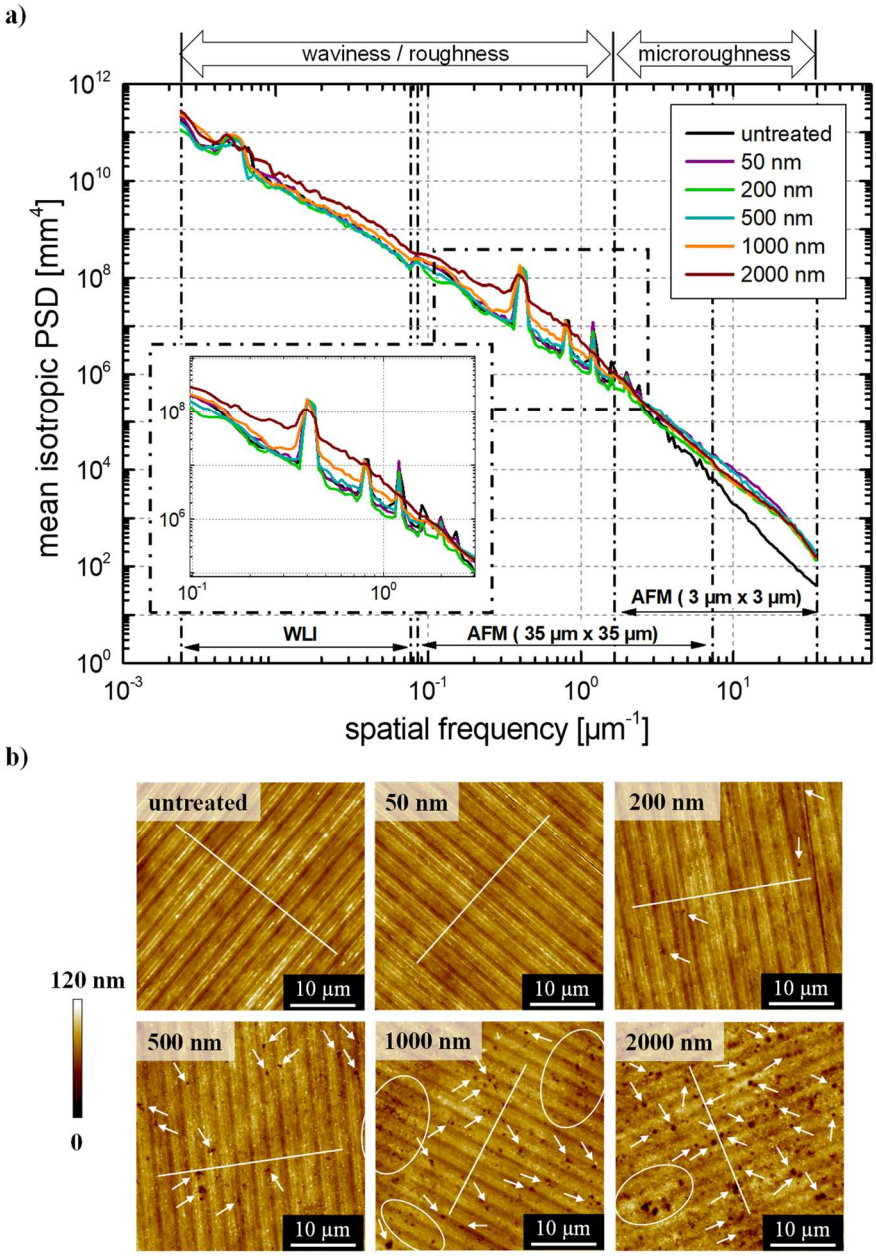


Fig. 4.3: a) PSD spectra calculated on the basis of AFM and WLI (5x objective) measurements. b) AFM measurements of the untreated Al905 surface and after RIBE machining with oxygen gas at different material removal depths [109]

Similar granular structure was also observed during depositing of polycrystalline AlN films on quartz substrates [113] and plasma nitriding of aluminium and aluminium alloys [114]. During the initial plasma nitriding, AlN nodules or particles are formed on the surface, covering in the proceeding stages the whole surface and resulting in the growth of a nitride layer controlled by thermal induced diffusion [113,114]. These small particles are a few tens of nanometers in diameter and tend to coalesce depending on the process parameters chosen.

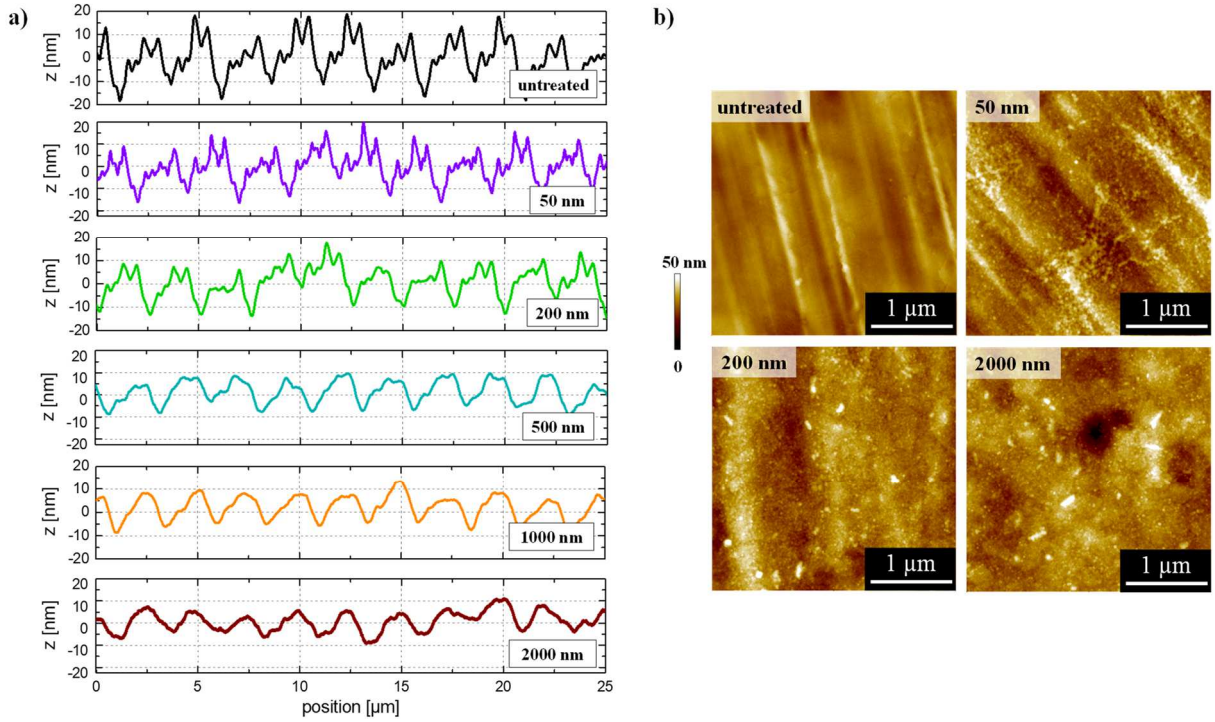


Fig. 4.4: a) Cross section profiles corresponding to the solid lines in the AFM measurements in Fig. 4.3 of the untreated Al905 surface and after N2 RIBE machining at different material removal depths. b) AFM measurements of the untreated Al905 surface and after N2 RIBE machining at different material removal depths [109]

ToF-SIMS measurements shown in Fig. 4.5 reveal, that instantly during the first 50 nm material removal, an approximately 15.1 nm thick nitride layer is formed. With increasing material removal depth, the nitride layer thickness does not change significantly, resulting in an averaged layer thickness of about (14.7 ±0.9) nm for all machining depths.

Consequently, a comparable model scheme can be suggested for RIBE processing with $N_2$ as already observed during oxygen machining [34]. The nitride layer formed also seems to act as a passivation layer which is eroded and simultaneously newly formed during processing, thus preserving the initial roughness. Indeed, the aluminium surface after RIBE machining with nitrogen exhibits a yellowish color. Since AlN is transparent in the visible spectral range, compositional or structural defects or impurities should be the reason for optical absorption and thus a changing color [113,115]. Consequently, reflectivity measurements were performed for each machining depth in comparison to an untreated surface (see Fig. 4.6).

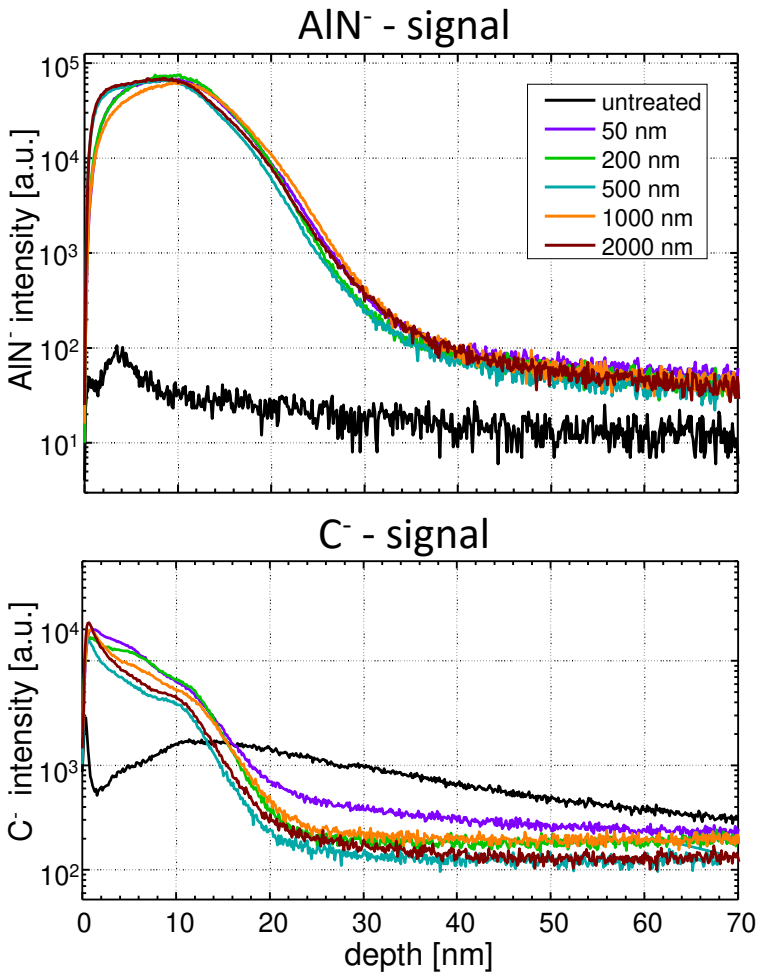


Fig. 4.5: ToF-SIMS depth profiles of RSA Al905 after RIBE machining with nitrogen operating gas at different machining depths. The extent of a nitride surface layer is represented by the AlN- - signal (top). The carbon is represented by the C- - signal (bottom) [109]

The untreated aluminium surface reveals high reflectivity over the whole measured wavelength range in the visible spectra with values of about 80 - 85 %. During nitrogen processing, the reflectivity decreases strongly over the whole measured wavelength range, especially at lower wavelength ranges below 700 nm. This might be caused by the formation of surface error features in the microroughness regime, since these roughness features have a considerable impact on light scattering influencing the spectral reflection characteristics in the visible spectral range due to broad halo scattering [115,116].

It is particularly noticeable that the lowest reflectivity is observed after the least material removal of 50 nm. With increasing material removal depth, the reflectivity increases again. This effect may be due to the increased microroughness as a result of the formation of nanoscopic granules without remarkable smoothing of the turning marks situated in the microroughness regime (see Fig. 4.4).

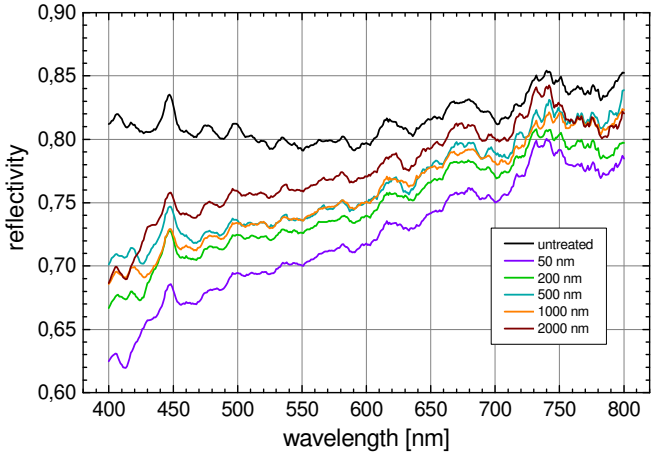


Fig. 4.6: Reflectivity in the visible spectral range of the untreated aluminium surface and after RIBE machining with nitrogen operating gas at different machining depths, [109]

In general, the reflectivity increases with increasing material removal depth. Minor deviations from this trend are found on the sample after $N_2$ irradiation with 500 nm material removal. In comparison to RIBE investigations after 1000 nm material removal, the reflectivity is slightly enhanced. Additionally, the 500 nm sample exhibits the lowest carbon incorporation (Fig. 4.5) while a distinct reduction of the turning mark structure situated in the microroughness regime is observed (Fig. 4.3).

Thus, also the carbon content might be a factor influencing the reflective properties of the surface. In general, the maximum carbon intensity is detected at the surface and increases with increasing depth for all RIBE machining depths (Fig. 4.5). Indeed, the carbon incorporation is deeper for lower material removal depths of 50 nm and 200 nm. The detected carbon signal within the aluminium nitride layer reaches to 6.9 nm depth after 50 nm material removal. In contrast, after 1000 nm and 2000 nm machining depth, the detected carbon signal reaches a depth of 4.1 nm and 2.8 nm, respectively (see Fig. 4.5). The graphite plasma anchor and the first ion extraction grid, which is made of graphite too, are in direct contact to the nitrogen plasma within the ion source. Thus, the anchor as a component in erosion seems to lead to carbon incorporation into the surface and might cause the reduced reflectivity after $N_2$ irradiation.

Generally, aluminium surface modification via nitrogen ion implantation is favorable for a number of technological applications like piezoelectric materials for surface acoustic wave devices or barrier layers in semiconductors [117,118]. For such applications, deep nitrogen diffusion into subsurface layers is appropriate [119]. Due to the limited implantation depth of

low-energy nitrogen ions, deep nitriding can thus only be achieved at sufficiently high temperatures [118-120]. During low-energy ion bombardment, the native oxide layer is reduced and a continuous AlN layer near the surface is formed. Additionally, a diffusional gradient of aluminium from the underlying bulk towards the surface results in a process-specific nitride thickness [119-121].

Similar observations are made during this study. However, the aim of these investigations is no specifically nitriding of the aluminium surface, but utilizing the formation of an AlN layer with nearly-constant thickness for roughness preservation during ion beam machining. The investigations on ion beam etching of an aluminium surface with $N_2$ at 1.5 keV reveal the formation of an aluminium nitride layer with a nearly-constant thickness of about (14.7 ±0.9) nm for all machining depths from 50 nm - 2000 nm material removal.

The process scheme for the $N_2$ RIBE process is thus expected to behave almost similar to the $O_2$ RIBE process [34], i.e. during processing a quasi-stationary, constant sized, moderating nitride etch front is formed as a result of the interplay between nitride film formation by nitrogen ion implantation and simultaneous sputter erosion of this nitride film. However, during $N_2$ irradiation an aluminium nitride layer is formed, which is accompanied by an increased microroughness and thus reduced reflectivity properties of the optical surface.

## 4.2 Local smoothing by reactive ion beam etching

Since high reflection coefficient over a broad wavelength range is required for high-performance mirror devices, the aim of the following chapter is to remove the nitride layer and establish an oxide layer instead, that shows improved reflectivity and a reduced microroughness [122].

Firstly, a process route is presented to directly smooth high spatial frequency errors on aluminium surfaces. Monte-Carlo simulations of the ion-surface interactions were performed with principle parameter settings chosen as described in [34]. The simulations were performed with the transport of ions in matter for sputtering (TRIM.SP) [123] code. Calculations of ion trajectories inside the solid to determine implantation profiles and collision cascades for sputtering yield analysis is enabled with this code [34]. Based on the Monte Carlo simulations and investigations on ion incidence angle dependent sputter erosion, a model scheme for direct smoothing of high-frequency surface features is suggested.

Subsequently, the described process route was applied on RSA Al905 after $N_2$ machining. Primarily the whole surface was irradiated with $N_2$ as described in section 4.1.2. Next, a RIBE-based smoothing procedure using oxygen at normal ion incidence was applied. The formation of a favorable oxide layer was analyzed by using two different ion energies (0.6 keV and 1.5 keV) in accordance to the ion energy dependent erosion process at normal ion incidence (2.2.3).

### 4.2.1 Local surface error slope dependent sputter erosion

A complete description of the surface topographical evolution under ion bombardment in direction of the sample normal is given by the local erosion velocity $\nu(\theta)$ related to the ion incidence angle dependent sputter yield $Y_{Al}(\theta)$ as a function of the local surface slope according to Nobes and Carter et al. [52-55]:

$$\nu\,(\theta) = \frac{J}{N} Y_{Al}(\theta)\cos\,(\theta) \qquad \textbf{(6)}$$

where N is the atomic density of the substrate, $J$ is the incident ion flux density and $\theta$ describes the local deviation of the incidence ions and the surface normal illustrated in Fig. 4.7a. For illustration, a cross-section profile of the schematic surface errors is demonstrated. The arbitrary point A on the surface is eroded to A' in a time t during machining. From equation (6), the rate of change of the point A in y-coordinate (perpendicular to the surface) and x-coordinate (parallel to the surface) is given by:

$$\nu_y(\theta) = \frac{J}{N} Y_{Al}(\theta)\ cos^2(\theta) \qquad\qquad \nu_x(\theta) = \frac{J}{N}\ Y_{Al}(\theta)\ \sin(\theta)\cos(\theta) \qquad \textbf{(7)}$$

Carter et al. [53-55] expected an additional contribution towards the evolution of a surface contour that is perceived as a progressive wavefront [53,56]. Hence, generally the erosion rate terms in equation (7) need to be enhanced by the correction terms $\nu_x+\nu_{\delta x}$ and $\nu_y+\nu_{\delta y}$, respectively, resulting in a further adjustment of A'. Though, for reasons of simplicity those contributions are neglected in this consideration, since the resulting adjustment is expected to be small for microroughness evolution. These equations indicate a local surface slope dependent evolution of surface roughness features during sputter erosion resulting in a smoothing of initially rough surfaces [56,57].

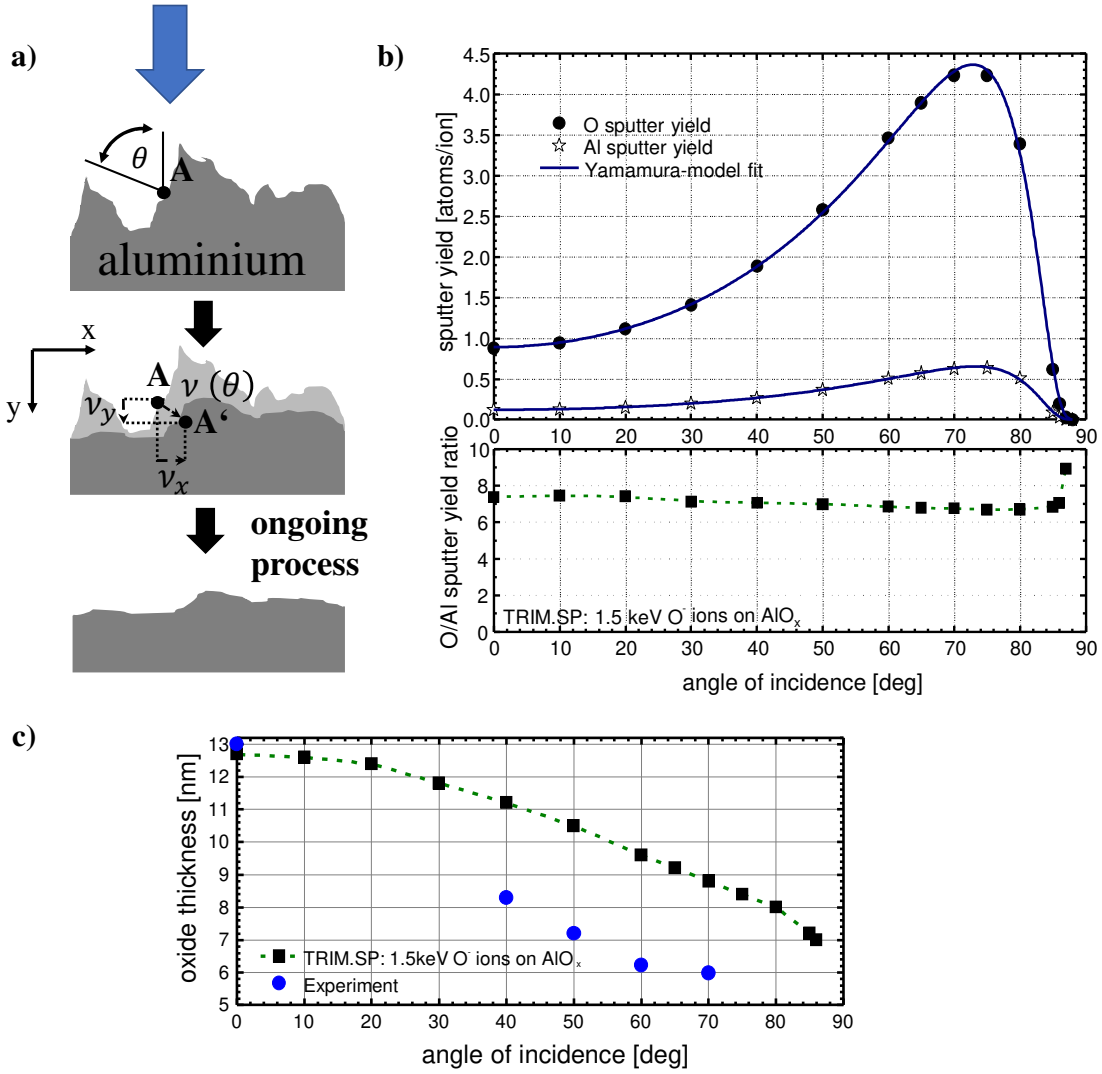


Fig. 4.7: a) Model scheme of microroughness reduction during RIBE machining with oxygen. The incidence angle of incoming ions deviated at the slopes of the microroughness features result in a smoothing effect. b) Component sputter yields $Y_{Al}(\Theta)$ and $Y_O(\Theta)$ with respect to incidence angle of 1.5 keV oxygen ions impacting oxidized aluminium calculated by TRIM.SP. c) Oxide thickness derived from the ion implantation depths of the TRIM.SP simulations and experimental thickness values derived from ToF-SIMS profiles (Fig. 4.8) [108]

For the special case of oxygen ions impinging the aluminium oxide layer, TRIM.SP simulations have been performed. The principle parameter settings have been chosen as described in the previous study [34]. For modeling of the RIBE machining process, the formation of non-stoichiometric $AlO_x$ was considered. As a remarkable result, sputtering with 1.5 keV oxygen ions results from the amorphous $AlO_x$ near surface region up to 1 nm depth. In this outer surface region, a high oxygen content with O/Al ratios ≈ 6 has to be considered [34,124-126]. With increasing oxygen content in the oxide layer, the sputtering yield of aluminium decreases gradually at normal ion incidence.

Fig. 4.7b shows the angle-dependent sputtering yield of aluminium $Y_{Al}(\Theta)$ and oxygen $Y_O(\Theta)$.The sputtering yields of both components are enhanced at an angle of incidence of about 70 deg by a factor of 5 compared to the value at normal ion incidence angle. As a noticeable result, the sputter yield ratio $Y_O(\Theta)/Y_{Al}(\Theta)$ as shown in Fig. 4.7b (lower plot) is almost constant up to 86 deg indicating a stoichiometry preservation of the surface oxide also in local surface areas with high slopes.

In Fig. 4.7c the calculated oxide thickness is shown for 1.5 keV oxygen ions impinging the surface. As a measure for the oxide thickness, the implantation depth covering 99.5 % of the implanted oxygen ions is applied. The oxide thickness is reduced with increasing ion incidence angle to 7.0 nm at 86 deg compared to 12.7 nm at normal ion incidence. Indeed, the oxide thickness is larger than the near surface region of 1 nm, where sputtering originates. Thus, the formation of sufficient thick surface oxide even in strongly inclined surface areas is suggested.

In addition to TRIM.SP calculations, ToF-SIMS depth profiling was performed with the resulting oxide thicknesses shown in Fig. 4.7c. Similar to the results obtained via TRIM.SP simulations, ToF-SIMS depth profiling of the Al905 surface after $O_2$ machining reveal a decreasing oxide thickness with increasing ion incidence angle as shown in Fig. 4.7c and exemplary illustrated in Fig. 4.8 for ion beam irradiation at 40° and 60°, respectively. For comparison, the approximate oxide thickness is determined as the distance from the surface to the depth, where the gradually decreasing $AlO_2^-$ - signal and increasing $Al_2^-$ - signal intersect.

However, the such-determined thicknesses of the experimental results are smaller than the values obtained during Monte-Carlo simulations. Indeed, the TRIM.SP program code does not regard the following experimental circumstances: (1) The roughening of the surface in the microroughness regime observed with increasing ion incidence angle is not covered. (2) The compositional gradients observed by SIMS experiments are not included [34].

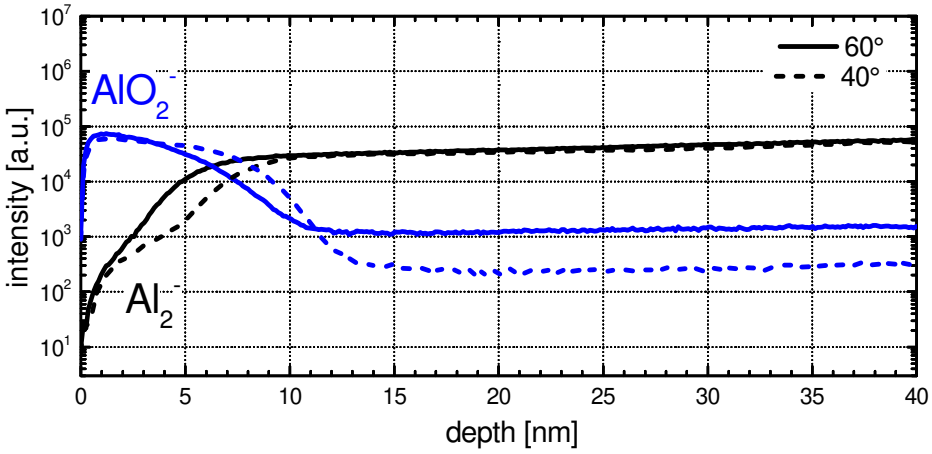


Fig. 4.8: ToF-SIMS depth profiles of RSA Al905 after $O_2$ ion beam irradiation at 40° and 60°, respectively. The oxide is represented by the $AlO_2^-$ - signal and aluminium by the $Al_2^-$ - signal

Moreover, as a result of the quasi-stationary process scheme, the sputter yield depends on the composition of the oxide formed during RIBE machining, which is not necessarily equal under changed ion current density conditions. However, the oxygen sputter yield is near unity in a broad range of $AlO_x$ compositions from O/Al ratios of 1.5 to 6.0, contributing to process stability [34]. For a ratio of 6, the oxygen to aluminium sputter yield ratio is almost independent of the angle of incidence (Fig. 4.7b). However, the situation changes, if the $AlO_x$ composition changes with the angle of incidence. Since the oxygen ion current density is homogeneously distributed over the sample and $Y_{Al}(\theta)$ increases at slopes, indeed a reduced oxygen content has to be considered in those local areas. Under experimental conditions of a slope area at the sample surface, the incoming ion current density has to be projected on the inclined surface area.

As a result, the arriving ion current density is reduced in slope areas counteracting the angle dependent effect on the sputtering yield as concluded from equations (6) and (7). The angle dependent effect on the erosion velocity is calculated via $\nu(\theta) / \nu(0) = Y_{Al}^{rel}(\theta) \cos(\theta)$ containing the relative aluminium sputter yield $Y_{Al}^{rel}(\theta) = Y_{Al}(\theta) / Y_{Al}(0)$. The erosion velocity perpendicular and parallel to the surface result from the relations can be written as [54,55,57]:

$$\nu_{yrel}(\theta) = \frac{\nu_y(\theta)}{\nu(0)} = \frac{Y_{Al}(\theta)}{Y_{Al}(0)} * cos^2(\theta) \qquad \nu_{xrel}(\theta) = \frac{\nu_x(\theta)}{\nu(0)} = \frac{Y_{Al}(\theta)}{Y_{Al}(0)} * \sin(\theta) * cos(\theta) \qquad \textbf{(8)}$$

In TRIM.SP calculations the ion current density decreases due to correction via equation (8). Consequently, an effective enhancement of the sputtering yields by a factor of 2 is obtained at the slightly shifted maximum at 60 deg compared to normal incidence (Fig. 4.9).

With increasing angle of incidence, the erosion velocity increases, since the intersection area of the ellipsoidal cascade volume with the surface increases and reaches a maximum at about 60° [45,127]. The ratio of the erosion velocity parallel to the surface and the erosion velocity perpendicular to the surface increases generally with increasing angle of incidence resulting in an increased smoothing effect.

These results are in good agreement with the experimental results illustrated in Fig. 4.9b in comparison to TRIM.SP simulations. However, with further increased ion incidence angles, the relative erosion velocity decreases again, since the probability of recoil generation decreases. Additionally, at near grazing incidence the number of reflected ions is increased which cannot penetrate the surface [55,128,129].

As a consequence, the surface errors with slopes ranging between 30° and 75° with respect to the surface normal are assumed to be faster eroded (Fig. 4.9). Thus, less enhanced smoothing rates are expected on roughness features with small surface gradients below 30°. Additionally, even reduced erosion rates are expected for surface slope border areas at near grazing angles above 80° compared to normal ion incidence.

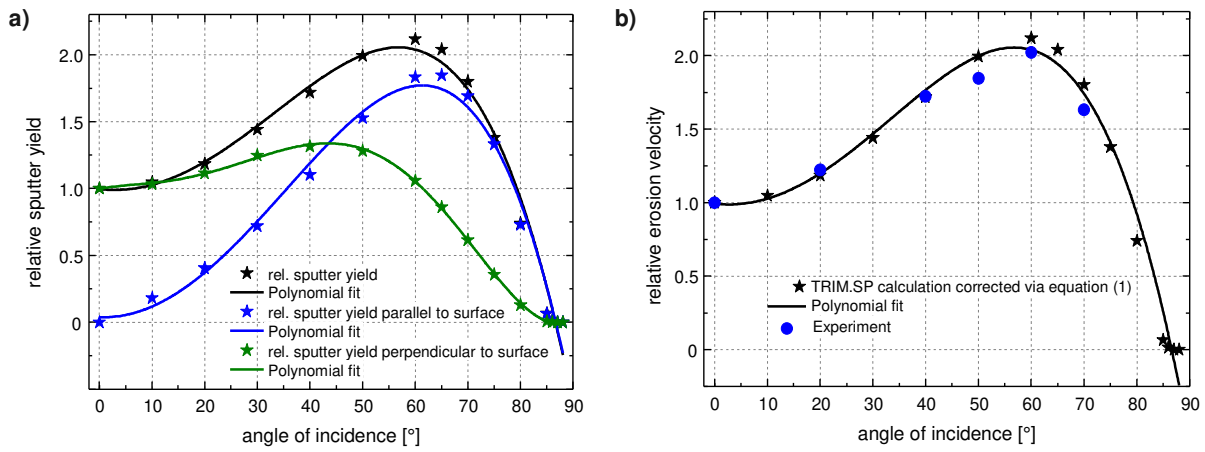


Fig. 4.9: a) Relative sputter yield of aluminium with respect to incidence angle of 1.5 keV oxygen ions impacting oxidized aluminium calculated by TRIM.SP and corresponding sputter yield rate parallel and perpendicular to the surface normal calculated via equation (8) and the experimental result are shown in b) [108]

Hence, the local sputtering yield can vary considerably at rough surfaces with high slopes. At the high slope surface sites, the oxide thickness and composition may be reduced and the sputtering yield is increased there, while the formation of an $AlO_x$ surface in locally smooth surface areas can lead to a self-masking effect as always obtained during oxygen ion beam processing at smooth surfaces.

Based on the experimental and the simulation results, the following model view is suggested for the effect of surface roughness evolution in RIBE processing of RSA Al905 surfaces with oxygen ions: Smooth surfaces exhibit an about 13 nm thick surface oxide layer during processing, which passivates structural and compositional inhomogeneities of the alloy matrix. Hence, the initial topography is preserved. With increasing surface roughness, more pronounced slopes become apparent on the surface resulting in locally different incidence angles of the incoming ions. Due to the angle dependence of the sputter yield, sputter erosion increases with increasing angle of incidence reaching a maximum at about 60 deg. Hence, surface areas with high slopes show an enhanced removal rate.

## 4.2.2 RIBE $O_2$ direct smoothing

Consequently, the as-described ion beam smoothing process is applied to an aluminium surface after $N_2$ RIBE processing for further reduction of the high spatial frequency errors in the microroughness regime and to improve the reflectivity.

### 4.2.2.1 Oxygen finishing at 1.5 keV

Firstly, the whole surface of an aluminium RSA Al905 disc sample was eroded using $N_2$ RIBE machining up to 900 nm machining depth (see Fig. 4.10). Subsequently, the material removal depth using $O_2$ RIBE was gradually increased via increasing number of scanning field repetitions within the defined machining area. One single repetition includes the raster path scanning of the ion beam over the whole defined machining area. Thus, multiple repetitions define a specific material removal depth (see Table 4.3).

The roughness evolution, reflectivity and chemical composition of the aluminium surface after 1x, 3x, 10x and 20x repetitions with oxygen at 1.5 keV beam energy were analyzed.

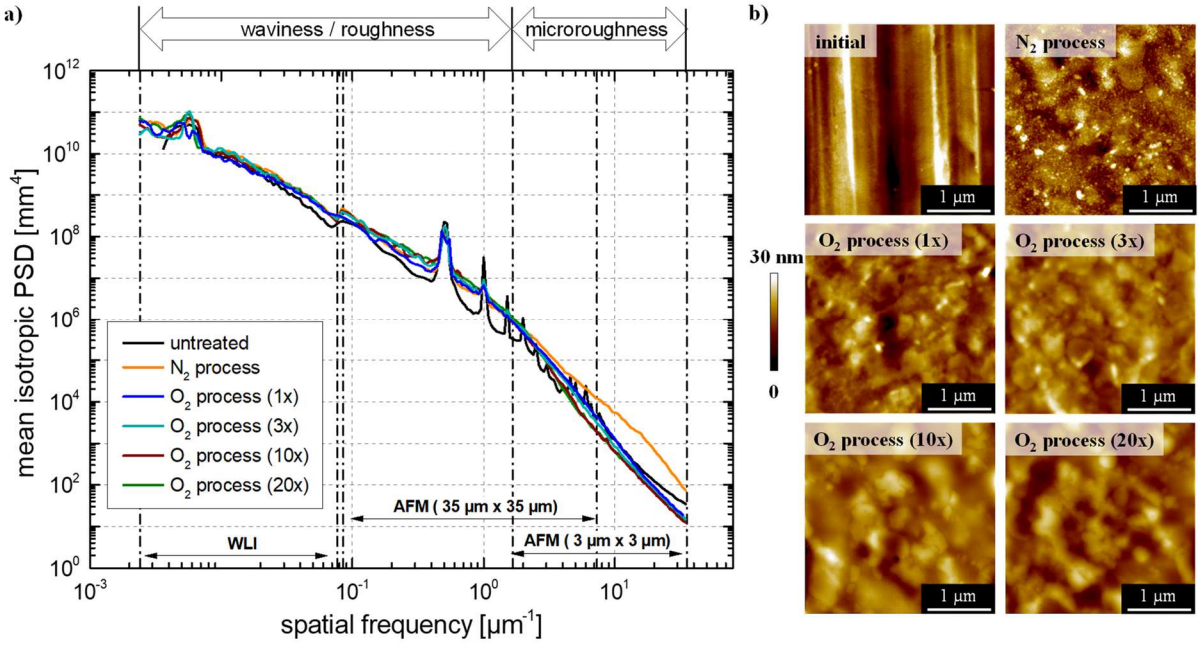


Fig. 4.10: a) PSD spectra calculated on the basis of AFM measurements. b) AFM measurements of the untreated RSA Al905 surface, after RIBE machining with nitrogen and subsequently applied RIBE machining with oxygen at different number of repetitions [109]

Table 4.3: Surface roughness of the untreated aluminium RSA Al905 surface and after RIBE machining with $N_2$ and subsequently $O_2$ gas at 1.5 keV beam energy

| RSA Al905 | Repetitions | Machining depth [nm] | Microroughness [nm rms] | Roughness + waviness [nm rms] | Full range [nm rms] |
|---|---|---|---|---|---|
| Untreated | - | | 3.4 ± 0.8 | 10.1 ± 1.5 | 10.6 ± 1.8 |
| RIBE $N_2$ | 20 | 905 | 4.5 ± 0.7 | 11.2 ± 1.4 | 12.0 ± 1.6 |
| RIBE $O_2$ | 1 | - | 3.4 ±0.5 | 10.2 ± 1.4 | 10.7 ± 1.8 |
| | 3 | 18 | 3.1 ± 0.3 | 11.1 ± 0.8 | 11.6 ± 1.6 |
| | 10 | 65 | 3.3 ±0.5 | 11.6 ± 1.8 | 12.0 ± 1.6 |
| | 20 | 123 | 3.5 ±0.9 | 11.5 ± 2.1 | 12.1 ± 2.6 |

Through RIBE machining with nitrogen, the whole PSD function illustrated in Fig. 4.10a slightly increases. The strongest deviation of about one order of magnitude in the PSD spectra can be observed in the high spatial frequency region of about 10 $\mu m^{-1}$ – 15 $\mu m^{-1}$. The microroughness is increased during $N_2$ RIBE to (4.5 ± 0.7) nm compared to (3.4 ± 0.8) nm of the untreated surface.

During $O_2$ finish, independent on the material removal depth, the microroughness is strongly reduced resulting in a decrease of all PSD spectra in the spatial frequency range above 2 $\mu m^{-1}$. Below 2 $\mu m^{-1}$ the PSD functions almost merge (Fig. 4.10a). One scanning repetition results in the removal of the granular structure and consequently a reduced microroughness of about (3.4 ±0.5) nm rms. With increasing material removal after 3x, 10x and 20x repetitions, no

distinct difference is observed, since the resulting microroughness values are (3.1 ±0.3) nm rms, (3.3 ±0.5) nm rms and (3.5 ±0.9) nm rms, respectively.

For a detailed discussion of microroughness evolution during RIBE finishing with $O_2$ gas, the gradient distributions of the microroughness features present on the aluminium surface after each processing step are calculated from the AFM measurements depicted in Fig. 4.10b. The gradient norm distribution was produced by assigning the local value of the maximal slope to each pixel via SPIP™ software. The local surface error slope distributions of the aluminium surface after RIBE machining with nitrogen and after subsequently applied RIBE finishing with oxygen at 1x, 10x and 20x repetitions are illustrated in Fig. 4.11.

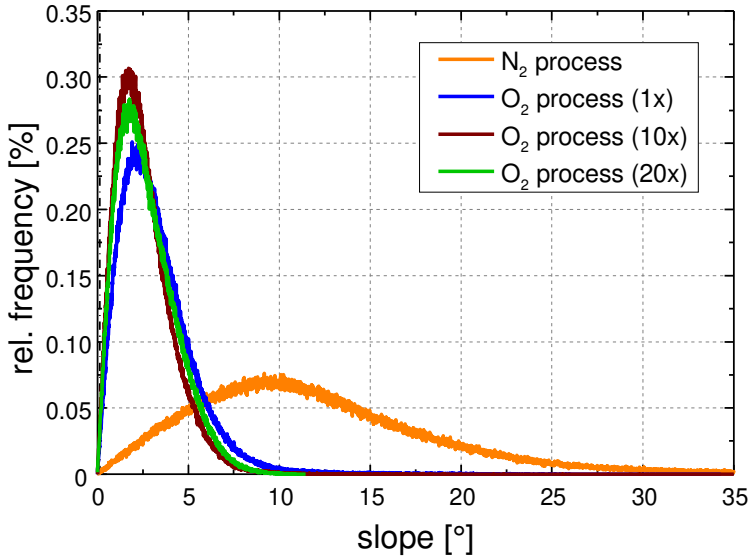


Fig. 4.11: Gradient distributions of RSA Al905 surface errors after RIBE machining with nitrogen and after RIBE finishing with oxygen using 1x, 10x and 20x repetitions [109]

The gradient distributions in Fig. 4.11 show, that already after one scanning repetition RIBE machining with oxygen, the local surface error slopes are shifted to lower values. With increasing scanning repetitions and therefore an increased material removal, the gradient distributions are further slightly shifted to lower values. Consequently, roughness features with high slope border areas are remarkably reduced since they show an enhanced erosion velocity resulting in a gradually smoothing of these surface roughness features [52-56,130]. Similar observations for ion beam smoothing of various materials (e.g. III-V semiconductors (InAs, InP, InSb), Si or fused silica) have been presented [57,131].

These results are in good agreement with the roughness evolution illustrated in Fig. 4.10. The smoothing of surface error features situated in the microroughness regime, which were formed during $N_2$ RIBE machining, are significantly reduced during oxygen finishing. In contrast, the formation of etch pits on the aluminium surface is enhanced with increasing material removal depth resulting in a slight degradation of the optical surface. Consequently, marginal material removal, generated within one scanning repetition, seems adequate to reduce the microroughness features formed during $N_2$ machining without any surface degradation due to the formation of etch pits.

Beside the improvement of the microroughness, the $O_2$ finishing additionally restores the optical properties to a considerable fraction after diminishing as a result of $N_2$ processing (see Fig. 4.12a). Indeed, during RIBE finishing with oxygen, the reflectivity over the whole measured wavelength range of 400 nm – 800 nm increases again but does not longer reach the initial value of an untreated RSA Al905 reference (see Fig. 4.12a). Scanning repetitions up to 10x lead to similar reflectivity improvement. However, after 20 repetitions, where an increased etch pit formation was observed, the reflectivity decreases in the wavelength range of 450 nm – 650 nm.

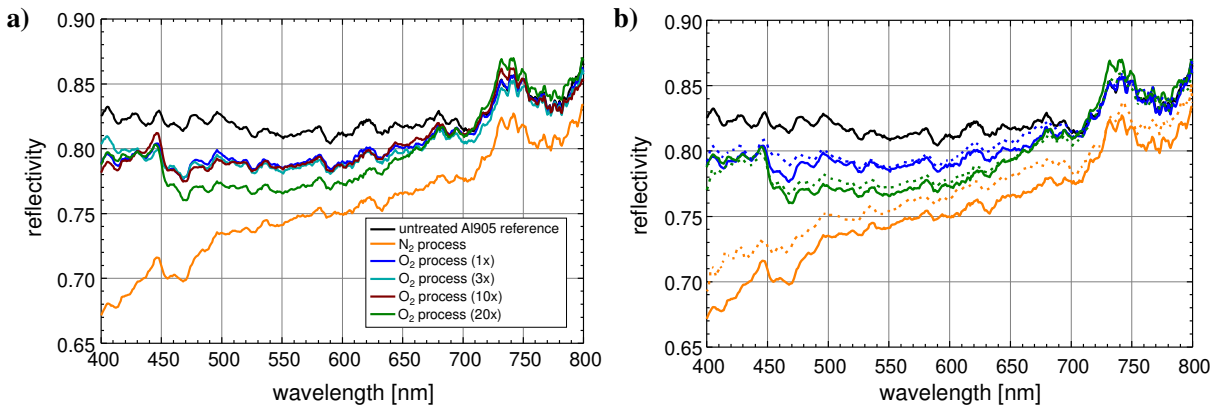


Fig. 4.12: a) Reflectivity in the visible spectral range of the initial aluminium surface, after RIBE machining with nitrogen and subsequent RIBE finishing with oxygen of 1x, 3x, 10x and 20x repetitions. The measurements are repeated after about one year. The resulting measurements are additionally shown in b) [109]

Additionally, the reflectivity was measured again after about one year storing the sample in air under lab conditions. The analysis shown in Fig. 4.12b reveals an increase in reflectivity over the whole wavelength range of the surface irradiated with nitrogen. It should be noted, that for reasons of clarity, only two exemplary curves of the repeated measurement on surfaces after subsequently applied $O_2$ finishing are shown in Fig. 4.12b.

The surfaces after 3x and 10x repetitions reveal similar improvement. Indeed, the surfaces which were subsequently irradiated with oxygen reveal only a slight improvement of the reflectivity. Specific oxidation of AlN is a temperature-dependent process, controlled by reaction or diffusion resulting in several µm oxide thickness [132]. However, the contact of the surface with ambient air after ion beam irradiation might result in a modification of the top surface layer due to reactions with oxygen at room temperature [133,134]. Consequently, the increased reflectivity might result from the formation of an oxygen-rich surface during storage.

ToF-SIMS measurements were performed on the aluminium surface after $N_2$ RIBE and subsequent $O_2$ finishing after different machining depths are shown in Fig. 4.13. The extent of an oxide surface layer is represented via the $AlO^-$ - signal. In addition, the $AlN^-$ - signal is used to illustrate the extent of a nitride surface layer after RIBE machining with nitrogen process gas and the residual nitrogen fraction inside the surface layer after subsequent $O_2$ RIBE processing.

After nitrogen machining, an about 15.3 nm thick nitride layer is formed on the aluminium surface overlapping with an approximately 5.5 nm thick oxide layer revealed on the surface, which may be attributed to native oxide layer formation instantly during the contact of aluminium with ambient air. The surface composition is strongly modified during $O_2$ finishing. An about 15.9 nm thick oxide layer is formed after one scanning repetition and is nearly independent on the material removal depth, since the thicknesses calculated after 3x and 20x repetitions are 16.8 nm and 16.1 nm, respectively (see Fig. 4.13b).

Consequently, the surface oxidation process described in a former study has to be considered [34]. Indeed, the $AlO^-$ - signal near the surface increases obviously while the corresponding $AlN^-$ - signal decreases strongly with increasing material removal (see Fig. 4.13a). The oxynitride - signal decreases with increasing scanning repetitions (see Fig. 4.13c). However, the near-surface region is mainly $oxygen^-$ - rich, so that the nitride surface layer formed during $N_2$ machining is continuously eroded and displaced during subsequent $O_2$ finishing.

Similar observations were discussed by Yue et al. and Kurbutowicz et al. during thermal oxidation of AlN ceramic substrates in the temperature range of 850 °C- 1100 °C [135,136]. Depending on the composition of the atmosphere, a series of physical and chemical processes take place. Hence, surface diffusion processes and sputter erosion seem to be the driving forces for surface modification within these investigations. The oxidation process observed during $O_2$ finishing procedure might result in the reduced reflectivity improvement observed in Fig. 4.12

over time. During the process, already an effective surface modification and oxygen-enrichment is introduced, leading to a reduced reaction with oxygen in ambient air when the sample is stored.

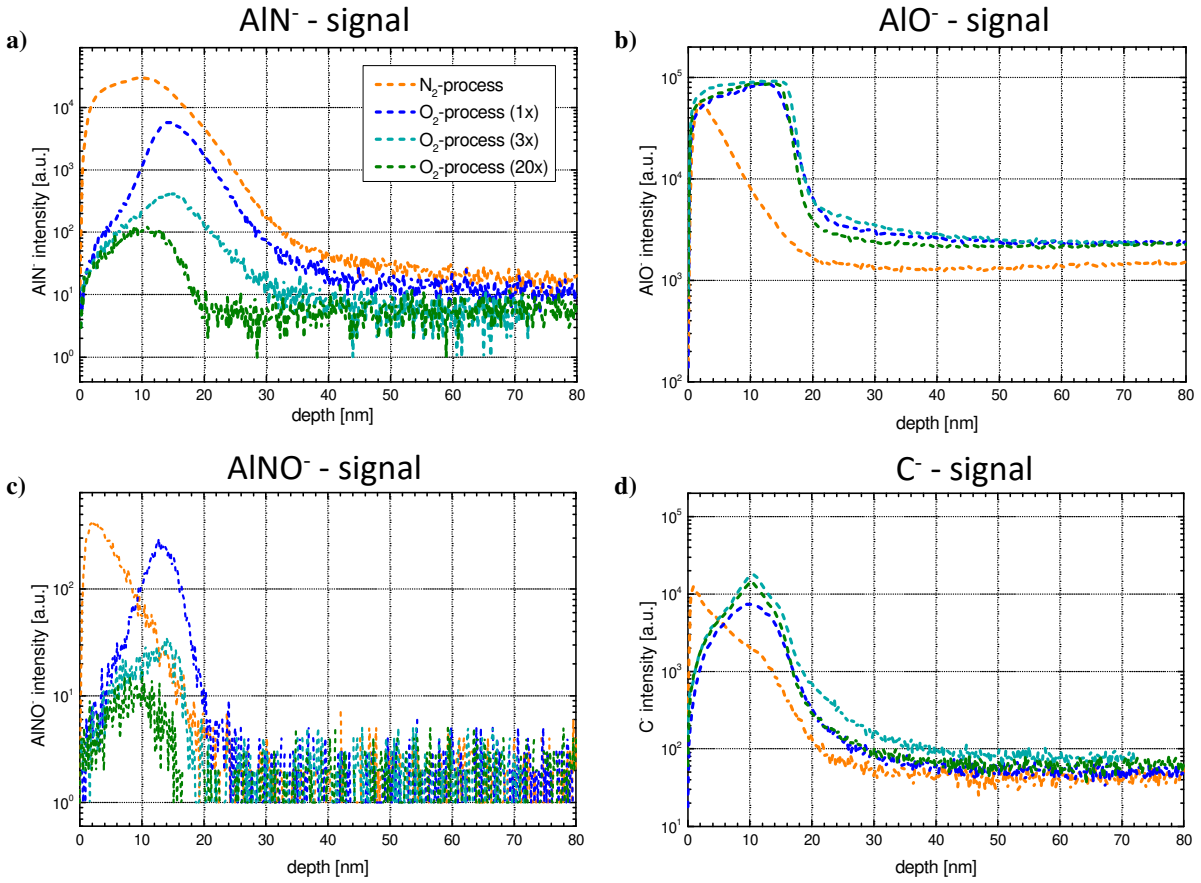


Fig. 4.13: ToF-SIMS depth profiles of RSA Al905 after RIBE machining with nitrogen and after oxygen finishing with 1x, 3x and 20x repetitions at 1.5 keV beam energy. The extent of a nitride surface layer is represented by the $AlN^-$ signal in a), the surface oxide layer is represented by the $AlO^-$ signal in b), the oxynitride is represented via the $AlNO^-$ intensity in c) and the carbon is represented by the $C^-$ signal in d) [109]

ToF-SIMS depth profiling investigations further reveal a shifting of the carbon signal during $O_2$ finishing (see Fig. 4.13d). During $N_2$ irradiation, the maximum carbon intensity is detected directly at the surface and decreases with increasing depth within the surface layer. In contrast, during subsequently applied $O_2$ finishing, the carbon is implanted deeper within the surface layer resulting in the shifted maximum at about 10 nm. The graphite plasma anchor might again be a driving force for carbon incorporation, as already discussed in section 4.1.2, causing also the reduced reflectivity compared to an untreated aluminium surface after oxygen finishing observed in Fig. 4.12. Carbon contaminations during optics fabrication is known as a critical issue reducing amongst others the reflectivity [137-139].

#### 4.2.2.2 Oxygen finishing at 0.6 keV

The second part of oxygen finishing investigations comprise RIBE machining with lower beam energy of 0.6 keV on another RSA Al905 disc sample with 1x, 2x and 4x repetitions. Despite the sputtering yield and thus the etch process efficiency are reduced at 0.6 keV, the ion implantation depth and forward sputtering of matrix atoms are reduced in general. Hence, at the expense of process time a less destructive sputter etch process with a reduced necessary removal depth can be expected to convert the nitride into an oxide layer.

The impact on oxide formation during ion beam irradiation at lower beam energy is analyzed in the following with distinct focus on roughness evolution, surface modification and reflectivity. Primarily, the whole surface of RSA Al905 sample is eroded with $N_2$ RIBE machining up to 1090 nm depth. The roughness evolution is summarized in Table 4.4 and illustrated in Fig. 4.14. The initial full range roughness of the RSA Al905 surface is already lower this time compared to the investigations for higher beam energy depicted in Fig. 4.10 and Table 4.3.

Table 4.4: Surface roughness of the untreated aluminium RSA Al905 surface and after RIBE machining using $N_2$ and subsequently $O_2$ gas at 0.6 keV beam energy

| RSA Al905 | Repetitions | Machining depth [nm] | Microroughness [nm rms] | Roughness + waviness [nm rms] | Full range [nm rms] |
|---|---|---|---|---|---|
| Untreated | | | 1.6 ± 0.2 | 7.6 ± 1.5 | 7.8 ± 0.6 |
| RIBE $N_2$ | 20 | 1091 | 3.4 ± 0.9 | 10.0 ± 1.3 | 10.7 ± 1.4 |
| RIBE $O_2$ | 1 | -- | 3.1 ±0.2 | 9.9 ± 1.3 | 10.4 ± 1.6 |
| | 2 | -- | 3.1 ± 1.0 | 8.8 ± 1.8 | 9.4 ± 3.0 |
| | 4 | -- | 3.2 ± 0.6 | 9.3 ± 1.3 | 9.8 ± 1.4 |

During $N_2$ machining, the PSD function is increased in the whole spatial frequency range resulting in a full range roughness of (10.7 ±1.4) nm rms (see Fig. 4.14a). Contrary to the results depicted in Fig. 4.3 and Fig. 4.10, exceptionally strong etch pit formation distributed over the whole surface is observed (see Fig. 4.15a). The surface degradation might be caused by the different initial surface quality, as different samples have been used.

In particular, the turning mark structure observed on the initial RSA Al905 surface for $O_2$ finishing at 0.6 keV has a period of 2.5 µm and an average height of (10.3 ± 2.0) nm (see Fig. 4.15a/c). In contrast, the initial surface for $O_2$ RIBE investigations at the higher beam energy of 1.5 keV depicted in Fig. 4.10 and Fig. 4.15b is characterized by turning marks with a period of 2 µm and an average height of (25.9 ± 2.5) nm. Probably the cutting tool of SPDT machine

might already be worn out which results in an eroded, larger cutting edge radius less prone to cutting and creating more plastic side flow [62,110]. The resulting smeared top surface layer results in a reduced roughness, but when this top layer is eroded during ion beam etching, the underlying surface quality is revealed resulting in an increased roughness. Indeed, the double-peak structure of the turning marks observed in Fig. 4.15b/c may also indicate an imperfection in the cutting tool shape.

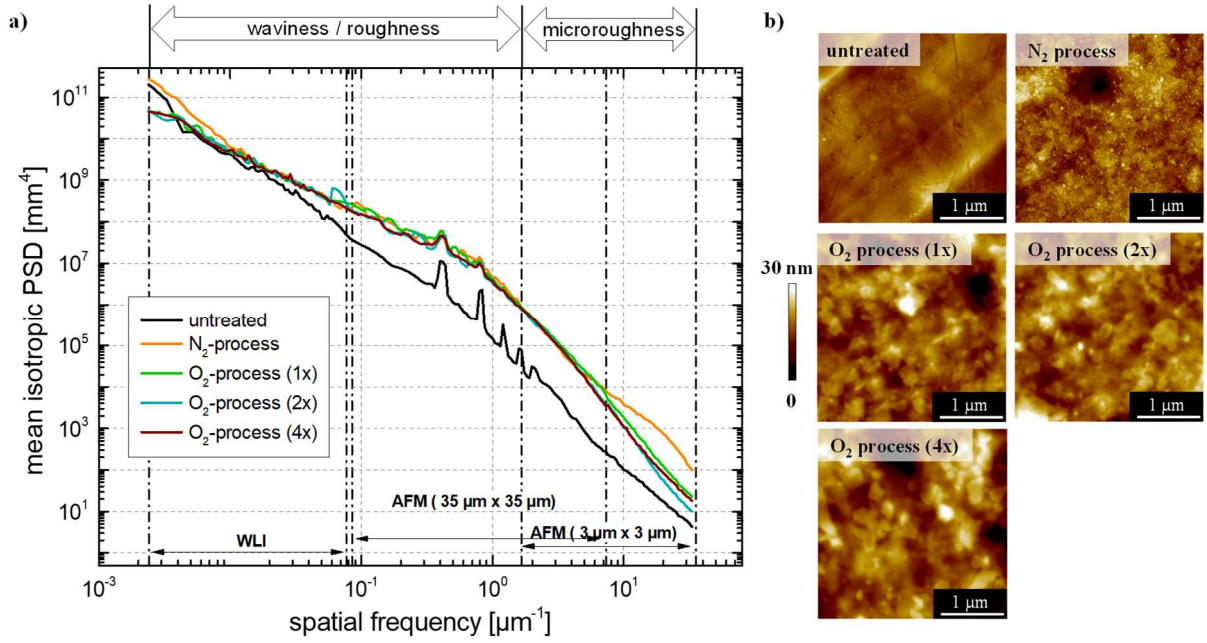


Fig. 4.14: a) PSD function of the untreated RSA Al905 surface, after RIBE machining with nitrogen gas and subsequent RIBE machining with oxygen at different numbers of scanning repetitions at 0.6 keV beam energy and b) corresponding AFM measurements with 3 µm x 3 µm scan sizes

Furthermore, the fine-grained structure of the precipitated phases, characteristic for rapidly solidified aluminium alloys [2,65], becomes more apparent during $N_2$ machining and subsequent $O_2$ finishing. This specific structure is already observed on the initial aluminium surface and might be carved out during ion beam erosion (see Fig. 4.14 and Fig. 4.15).

The gaping discrepancies in the batch number of both aluminium samples used for ion beam investigations might be affected by compositional differences of the alloy. The RSA Al905 alloy material mainly contains Ti, Ni, Cu, Ga, Fe, Mn and Mg and portions of Cd, Mo, Zn, Zr, Cr and Si in the aluminium base. As already observed in a formed study [34], etch pit formation due to Mg and Si fractions within the aluminium matrix was promoted resulting from preferential sputter erosion.

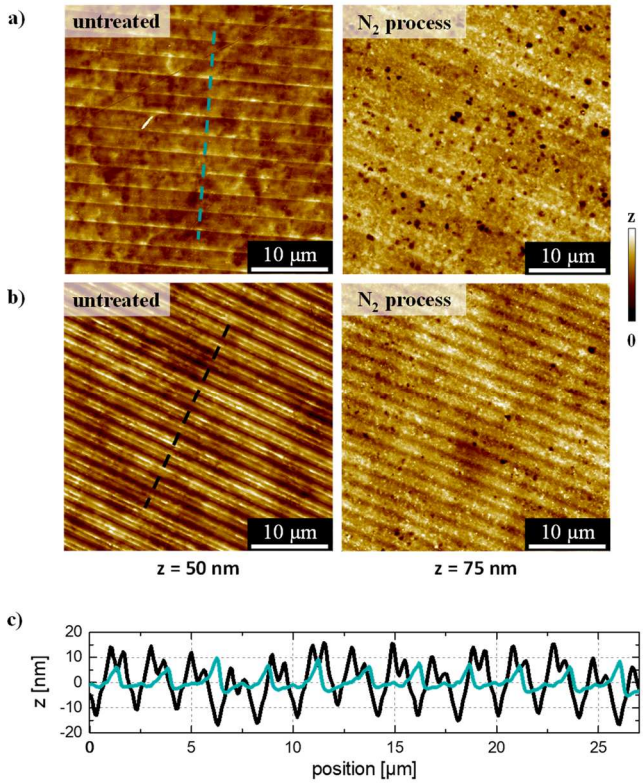


Fig. 4.15: AFM measurements (35 µm x 35 µm) of the a) untreated Al905 surface depicted in Fig. 4.14 and after subsequent N2 machining with 1090 nm material removal and b) the untreated Al905 surface depicted in Fig. 4.10 and after subsequent N2 machining with 900 nm material removal. The corresponding cross section profiles of both untreated surfaces represented via dashed lines in a/b is illustrated in c)

Nevertheless, during $O_2$ finishing, the PSD functions indicate a distinct reduction in the spatial frequency range above 7.3 $\mu m^{-1}$. Consequently, the microroughness is reduced to (3.1 ±0.2) nm rms after one repetition. With increasing material removal, the microroughness hardly changes and results in (3.1 ± 1.0) nm rms and (3.2 ± 0.6) nm rms after two and four repetitions, respectively. Additionally, the PSD functions in the whole spatial frequency range almost merge (see Fig. 4.14a).

The chemical surface modification analyzed by ToF-SIMS measurements further indicate a native oxide layer of about 4.9 nm and the formation of a 14.5 nm thick nitride layer after $N_2$ processing (see the orange curves in Fig. 4.16a/b).

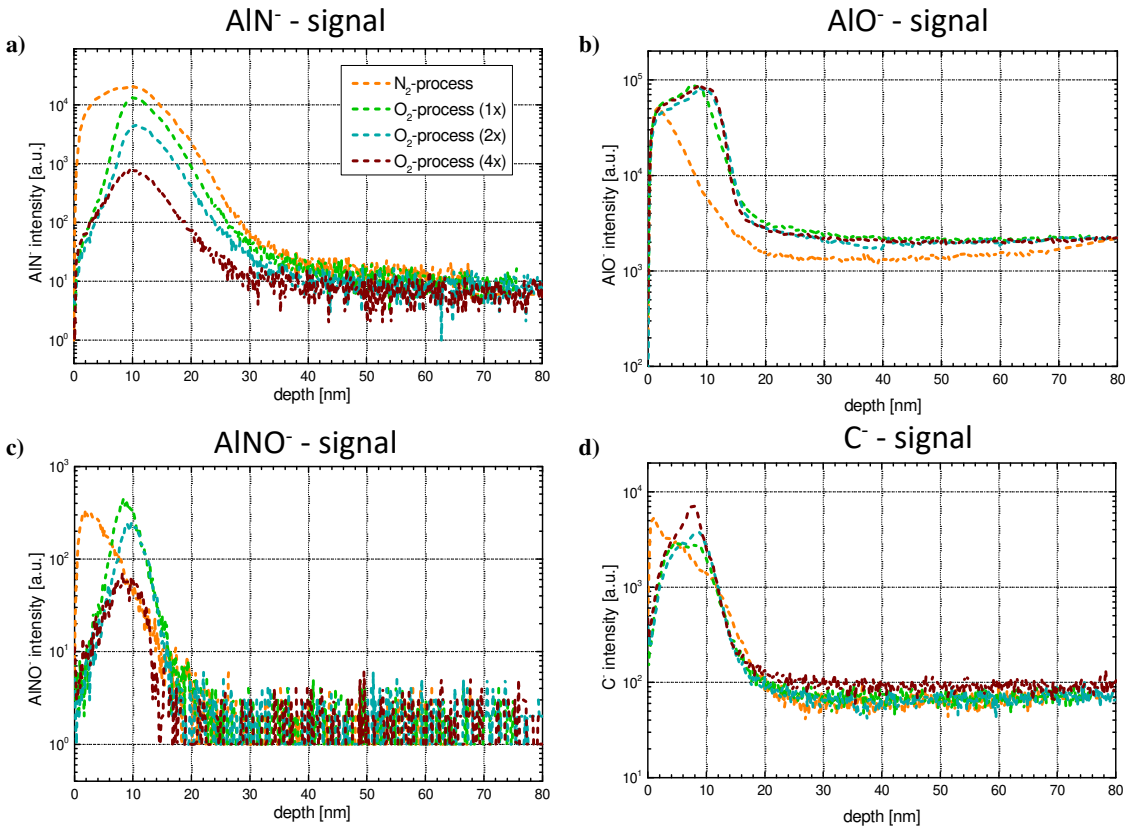


Fig. 4.16: ToF-SIMS depth profiles of RSA Al905 after RIBE machining with nitrogen and after subsequent oxygen finishing at 1x, 2x and 4x repetitions at 0.6 keV beam energy. a) the extent of a nitride surface layer is represented by the $AlN^-$ signal, the surface oxide layer is represented by the $AlO^-$ signal in b), the oxynitride is represented via the $AlNO^-$ intensity in c) and the carbon is represented by the $C^-$ signal in d)

During subsequent $O_2$ finishing, similar oxide enrichment is observed (compare to Fig. 4.13b) with $O_2$ finishing at 1.5 keV. After one repetition the depth of the oxide layer is significantly enlarged to 10.8 nm. Increasing repetition numbers lead to a continuous erosion of the nitride layer formed during $N_2$ machining. In contrast to $O_2$ finishing investigations at 1.5 keV beam energy, the oxide layer is enlarged to 10.8 nm after one scanning repetition and stagnates afterwards at about 12.4 nm and 12.3 nm after 2x and 4x repetitions, respectively.

Indeed, the oxide layer formed during $O_2$ finishing using 1.5 keV beam energy is thicker and the nitride-rich region is decreased to a greater extent for 0.6 keV (see Fig. 4.13a/b and Fig. 4.16a/b). The oxynitride signals are also shifted and reduced with increasing scanning repetitions (see Fig. 4.16c). Furthermore, with increasing scanning repetitions, the $AlN^-$ - signal decreases gradually. The shifting of the carbon signal shown in Fig. 4.16d reveal similarity to the investigations at 1.5 keV beam energy.

Reflectivity measurements indicate similar improvement in the whole measured wavelength range of 400 nm – 800 nm during subsequent oxygen finishing at 0.6 keV (see Fig. 4.17). In contrast to the investigations at 1.5 keV energy, the reflectivity increases with increasing material removal depth, almost reaching the initial value of an untreated Al905 reference after 4 repetitions. The proceeding surface modification due to oxygen - enrichment and nitride - declining might cause the gradual improvement of the reflectivity with increasing $O_2$ finishing repetitions.

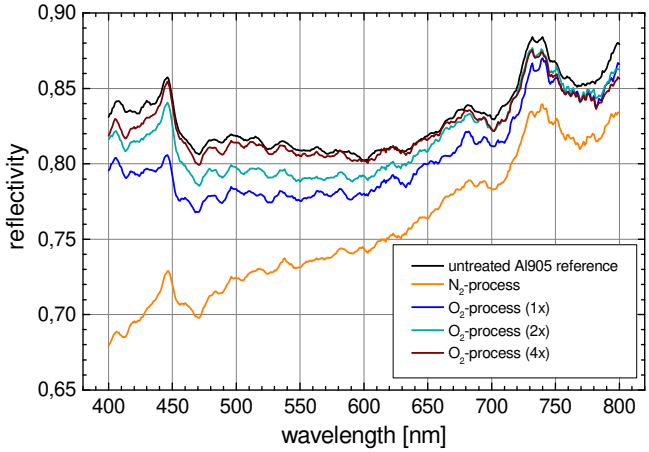


Fig. 4.17: Reflectivity in the visible spectral range after RIBE machining with $N_2$ and $O_2$ finishing at 0.6 keV after 1x, 2x and 4x repetitions

## 4.3 Conclusions

An extension of the RIBE-based model scheme for ion beam figuring of optical aluminium surfaces using nitrogen operating gas was examined. In a former study, a RIBE model scheme was suggested based upon the in situ formation of a surface oxide layer acting as a passivation layer inhibiting aluminium surface mobility and compositional inhomogeneity, thus preserving the initial surface topography during RIBE machining up to a depth of 400 nm [34].

Investigations on RIBE machining with nitrogen operating gas reveal a roughness preservation up to 1 µm machining depth with moderate surface degradation up to 2 µm. PSD analysis showed, that surface topography between 0.0024 $\mu m^{-1}$ – 0.27 $\mu m^{-1}$ remain nearly unchanged. An improvement of the surface topography was found for the turning mark features, which are smoothed out to some extent during ion beam machining. Marginal surface degradation caused by etch pit formation in the spatial frequency range of 0.27 $\mu m^{-1}$ – 2.5 $\mu m^{-1}$ was observed after 1 µm material removal.

The formation of a (14.7 ± 0.9) nm thick aluminium nitride layer seems to act as a passivation layer already observed with oxygen operating gas. The surface nitride layer is eroded and simultaneously newly formed during machining. Hence, the depth range for RIBE processing is significantly increased by using nitrogen compared to oxygen. However, one exception is the increased microroughness during nitrogen machining resulting from the formation of the nanoscopic granular structure over the whole aluminium surface. Once this structure has been formed, it remains almost unchanged up to 2 µm material removal.

Investigations on ion beam smoothing with $O_2$ using two different beam energies of 1.5 keV and 0.6 keV revealed a distinct decrease in microroughness while preserving the surface roughness. The PSD function is decreased in the spatial frequency range of $2.5\ \mu m^{-1}$ – $34.7\ \mu m^{-1}$ up to a machining depth of about120 nm, whereas no distinct surface degradation is observed when 1.5 keV beam energy is used.

The oxide layer formed during RIBE machining has a thickness of about 16 nm already after one repetition and is pretty constant with increasing material removal. Additionally, the reflectivity is improved during oxygen finishing but no longer reaches the value of an untreated aluminium surface before machining. The effect seems to result from the increased carbon content within the surface layer due to the graphite plasma anchor erosion and marginal surface degradation caused by an increased etch pit formation after 120 nm material removal. Though, marginal material removal during subsequent oxygen finishing is demanded to improve the surface quality again.

During $O_2$ RIBE investigations with 0.6 keV beam energy, the microroughness is also reduced in the spatial frequency range of $7.3\ \mu m^{-1}$ – $34.7\ \mu m^{-1}$. Additionally, the reflectivity almost achieves the value of an untreated aluminium surface. A comparison of both beam energies with nearly similar machining depth reveal a reduced oxide layer formation during $O_2$ RIBE machining with 0.6 keV beam energy, since the penetration depth of oxygen within the nitride layer formed during $N_2$ RIBE is reduced when 0.6 keV are applied. The improvement of the microroughness was enhanced during $O_2$ RIBE with 1.5 keV beam energy to a value comparable of the initial microroughness. However, the initial microroughness of the aluminium surface used for investigations with 1.5 keV beam energy during $O_2$ finishing was already higher than for investigations with 0.6 keV beam energy. Assuming that the unexpected surface degradation during $N_2$ machining results among others from the removal of the

modified surface top layer formed during SPTD and a different material composition, comparable results were obtained. In case of the worn cutting tool, the modified surface due to plastic flow might result in the improved microroughness before machining.

The RIBE model scheme can therefore be extended to include the process gas nitrogen requiring two consecutive process steps. In particular, the initial aluminium roughness is exceedingly well preserved up to 1 µm machining depth during the process route. Furthermore, the second process step including ion beam smoothing using oxygen decreases microroughness features formed during $N_2$ operating after short processing time.

# 5 Technological aspects on photoresist preparation for ion beam planarization

In addition to the direct ion beam smoothing procedure discussed in section 4.2, the ion beam planarization process addresses the reduction of the periodical pattern structure formed during SPDT. As already mentioned in section 2.2.2, an optimized selectivity, i.e. nearly identical removal rates of planarizing layer and substrate, is prerequisite for an adequate transfer of the smooth surface of the polymer sacrificial layer into the aluminium surface. Consequently, the process conditions have to be optimized to the specific material combination. Since ion beam etching with reactive process control is used, extended degrees of freedom for process development are available.

Among all the experimental parameters involved, an appropriate photoresist is chosen firstly. Main aspects for this choice are related to the specific behavior under ion irradiation as roughness preservation during ion beam machining and sufficient ion beam resistance of the polymer matrix to achieve an optimized selectivity. To provide an optimum photoresist layer, technological polymer stabilization techniques are considered. Thus, application steps as deep-UV (DUV) exposure and postbaking are optimized for the suitable photoresist. In addition, the dependence on different process parameter, i.e. operating gas and ion energy will be analyzed. Commercially available 2 inch single-side polished p-type Si (100) sample were used as substrates for the photoresist optimization experiments. Parts of this chapter are submitted and currently under review [107].

## 5.1 Selection of a suitable photoresist

The type of sacrificial layer used for ion beam planarization is a critical parameter that affects the surface transfer during ion beam erosion. The smooth surface of the thin planarizing layer is transferred into the substrate via removing the whole layer during ion beam etching. Consequently, five different commercially available photoresist materials were analyzed with a special focus on roughness evolution during ion beam irradiation and the resulting material removal rates. Therefore, all photoresist layers were applied and prepared with respect to the

individual material data sheet [68-71]. The resulting thicknesses of the individual photoresist layers were in the range of some hundreds of nanometers, dependent on the photoresist composition, in particular the amount of organic solvent and the parameter chosen for the application steps. Some selected properties of the photoresist materials are summarized in appendix B. $N_2$ RIBE machining at 1.2 keV on all photoresist layers was performed under identical conditions, scanning the ion beam with a constant velocity of 6 mm/s and a 0.5 mm line pitch within 10 repetitions over the surfaces. Fig. 5.1a represents the observed etch rates of all photoresist materials.

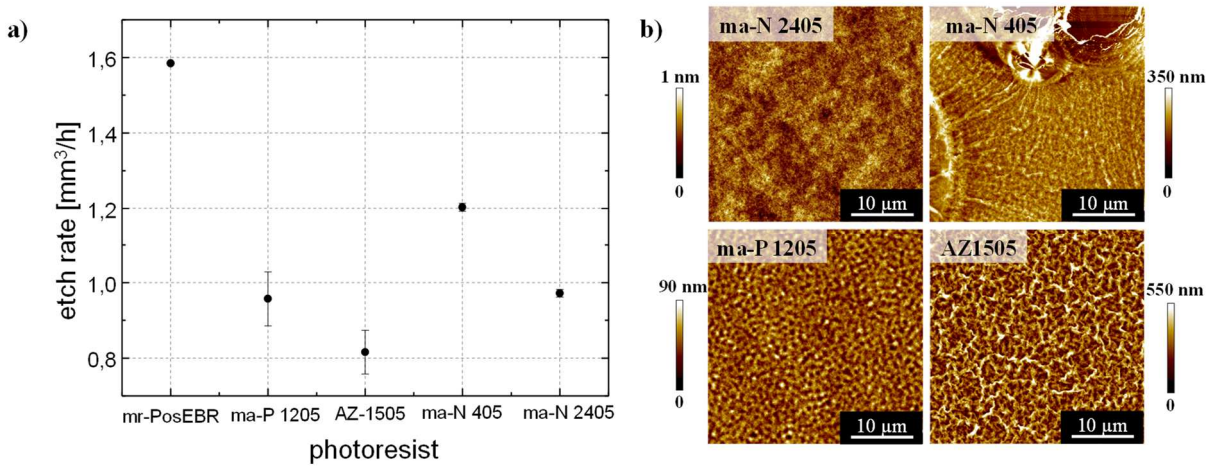


Fig. 5.1: a) Etch rate dependence of different photoresist materials during ion beam etching with N2 operating gas at 1.2 keV. b) AFM measurements of AZ1505, ma-P 1205, ma-N 405 and ma-N 2405 indicating partially photoresist degradation during N2 RIBE at 1.2k keV

The positive tone mr PosEBR0.3 and negative tone ma-N 405 photoresists show the highest etch rates, whereas both positive tone ma-P 1205 and AZ 1505 as well as the negative tone ma-N 2405 have nearly similar etch rates. For an optimized selectivity, a lower photoresist etch rate is prerequisite. Consequently, both photoresist layers exhibiting the highest etch rates are excluded for further investigations. Since both negative tone photoresist are specific compounds of the ma-N series, the differences might be due to the deviant crosslinking behavior and temperature stability of the compounds [140].

When marginal material is removed, the positive tone photoresist materials are mainly roughness preserving. However, in case of reproducibility and roughness preservation during ion beam planarization, the results differ strongly when the material removal depth is increased. $N_2$ RIBE machining was additionally performed within 20 repetitions on the photoresist layers. As it can be observed from Fig. 5.1b, different topographies evolve under given conditions. In

particular, both positive tone photoresists start to degrade during ion beam irradiation. The wavy regular pattern formation observed during RIBE machining has been intensively studied for many types of polymers, like polystyrene [141], 193 and 248 nm photoresist [142,143] and diazonaphthoquinone-based novolak photoresist [144], and has been described as the formation of a thin carbon-like modified layer, which is formed during argon or fluorocarbon plasma exposure [142,145]. Buckling is caused by relaxation of the mechanical stress resulting from the highly compressed, modified surface layer. Indeed, similar surface degradation caused by a wrinkling formation and especially bubble formation is observed during $N_2$ RIBE of ma-N 405 (see Fig. 5.1b).

However, the negative tone photoresist ma-N 2405 showed a low etch rate and a roughness preservation during $N_2$ RIBE processing. The selection of a negative photoresist as planarizing layer has several merits. The resist film can conveniently be applied by industrial standard techniques like spin coating or spray coating, the thickness is controllable by spin speed and dilution, and the crosslinking of the negative working photoresist during exposure to UV light reduces the photosensitivity significantly [66,146,147]. Consequently, the following investigations are carried out with this type of resist.

## 5.2 Photoresist application steps

The DUV-sensitive negative tone photoresist ma-N 2405 is composed of a novolak as polymeric matrix, the biazide as photoactive compound (PAC) and an organic solvent consisting of anisole and cyclopentanone [147,148]. The resist was applied by spin coating on the workpiece, prebaking, exposure in UV light and an optional postbaking. Remaining solvent is reduced by prebaking in order to prevent bubbling by evaporating solvent during subsequent thermal processes and to increase the etch resistance and thermal stability [147,149]. Prebaking was performed at 90° C according to the processing guideline [147]. Postbaking is an optional preparation step to further increase thermal stability and etch resistance (see Fig. 5.2) [147].

To improve the resistance of the negative photoresist ma-N 2405 for ion beam planarization of optical aluminium surfaces, the applications steps DUV exposure and postbaking are examined in detail in the following.

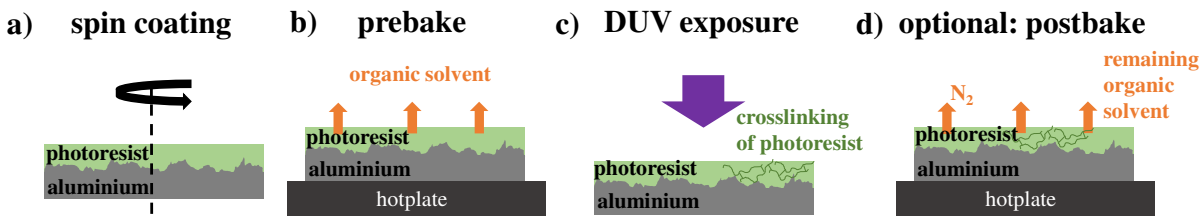


**Fig. 5.2:** Illustration of the processing steps for ma-N 2405 photoresist application

## 5.2.1 DUV exposure of the photoresist layer

During DUV exposure, the azide groups of the PAC (R-N3) release nitrogen and the resulting reactive nitrenes (R-N:) initiate the crosslinking of the resist [146,148,150-152]. In order to assure a proper crosslinking state by the applied exposure routine, infrared spectroscopic measurements were performed before and after UV exposure. For that reason, the following conclusions about the polymer matrix state are drawn from the relevant vibration mode frequency bands as marked in Fig. 5.3.

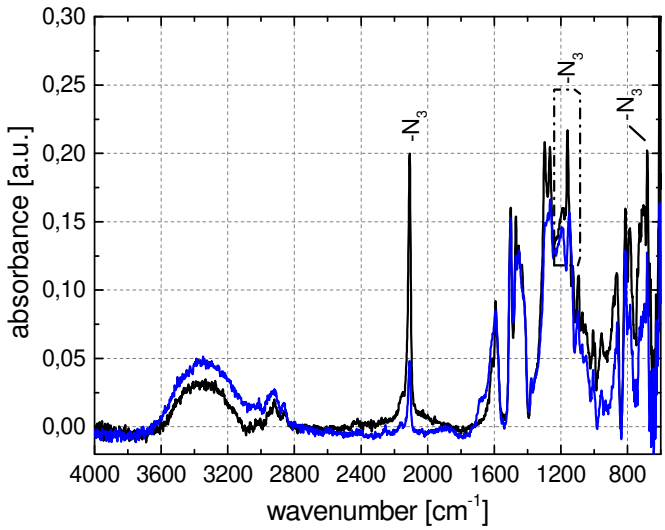


Fig. 5.3: ATR-IR measurements of negative photoresist ma-N 2405 before UV exposure (black curve) and after UV exposure (blue curve) [107]

The measured IR spectra of the negative photoresist ma-N 2405 (black curve in Fig. 5.3) shows the characteristic absorptions of a phenolic structure [145,148,153-155], and of the azide groups ($-N_3$) of the PAC with three characteristic vibrational bands. The strong peak in the region of 2160 – 2090 $cm^{-1}$ corresponds to the asymmetric stretching vibration. The symmetric stretching vibration located at 1340 – 1180 $cm^{-1}$ and the azide bending vibration around 700 $cm^{-1}$ [148,156]. The broad region between 3600 – 3200 $cm^{-1}$, that is characteristic for phenolic -OH

stretching vibrations, overlaps with symmetric -NH stretching vibrations of the PAC. In the relative broad region of 1720 – 1580 $cm^{-1}$ deformation vibrations of $-NH_2$ or -NH of the PAC may also be located. The strong peaks at 1160 $cm^{-1}$, 1266 $cm^{-1}$ and 1296 $cm^{-1}$ may correspond to -CO stretching vibrations of the phenolic resin or the organic solvent, the symmetric stretching vibration of the azide group of the PAC or its -CN stretching vibrations [145,148,151]. After DUV-exposure of ma-N 2405 (blue curve in Fig. 5.3) the peak intensities in the range of 3600 – 2900 $cm^{-1}$ increase. This is attributed to the reaction of the hydroxyl group of the novolak polymer with intermediate of the photo-induced decomposition of the biazide [148]. The peak intensities dedicated to the azide group of the PAC located at 2108 $cm^{-1}$ (asymmetric stretching), 1340 – 1180 $cm^{-1}$ (symmetric stretching) and approximately 700 $cm^{-1}$ (bending) decrease immensely. This behavior is consistent with the crosslinking mechanism of the negative photoresist [148,150,152]. In correlation with the decomposition of the PAC, the peak intensities decrease and therefore the probability of crosslinking within the polymer network is increased.

## 5.2.2 Postbake: the influence of the amount of organic solvent

To provide optimum photoresist layers for ion beam planarization, the thermal stability limits were investigated by TGA, GC/MS and DSC. Prebaking of the photoresist was performed in a compartment dryer at 90 °C for about 10 minutes. Subsequently applied DUV exposure was performed for 2 minutes. The TGA and DTG profiles in Fig. 5.4 show a comparison of the prebaked and DUV exposed negative photoresist ma-N 2405 containing a high amount of organic solvent and after additionally postbaking in a compartment dryer at 90 °C for 360 minutes.

The analyzed photoresist after prebaking and DUV exposure but without subsequently applied postbaking has one rapid mass loss step characterized by an onset temperature of approximately 78 °C and a peak temperature of 147 °C. The subsequent second mass loss step has an onset temperature of 395 °C and a peak temperature of 463 °C. The DTG of profile I indicates a shoulder arising at the first peak at approximately 200 °C. At higher temperatures, the profile reaches a plateau with a nearly constant remaining mass between 600 - 800 °C. After additionally postbaking of the photoresist layer, the first mass loss step decreases strongly with a corresponding increased onset of 154 °C and a peak temperature of 208 °C. The second mass

loss step has an onset of approximately 261 °C and two peak temperatures at 390 °C and 480 °C. Above 600 °C the profile reaches a plateau with a nearly constant remaining mass.

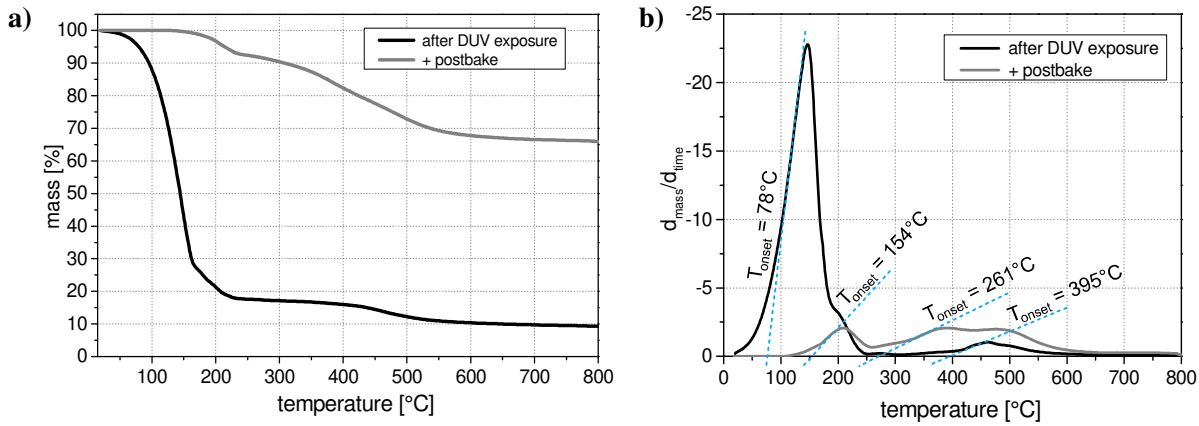


Fig. 5.4: a) Thermogravimetric analysis of the liquid negative tone resist ma-N 2405 after DUV exposure without postbaking and after postbaking in the compartment dryer at 90 °C for 360 minutes. b) Derivative curves (DTG) calculated from a)

Consequently, drying at a low temperature of 90 °C is a relevant step to remove organic solvent. The TGA measurement after drying is in good agreement with results from Jackson and Conley [157], who did a careful resin preparation of phenol formaldehyde polycondensates to ensure no entrapped organic solvent. The profile of the postbaked resist layer shows a nearly identical behavior indicating a strong reduction of the amount of solvent in the resin after postbake. However, to indicate optimum photoresist preparation, additionally postbaking at elevated temperatures was analyzed.

## 5.2.3 Postbake: the influence of the baking temperature

Gutman et al. proposed, that DUV-hardened photoresist via photosensitive stabilizers and additional thermal crosslinking of the bulk afterwards result in an increased thermal stability up to 300 °C [158]. Additionally, Johnson et al. [47] suggested a dependency of the etch rate under ion beam treatment and the previous heating temperature of the resist. They considered a higher etch resistance and therefore a lower etch rate after heating the novolak-based photoresist up to 150 °C before processing.

Thus, the influence of photoresist postbaking on surface roughness was investigated by AFM measurements. The negative photoresist ma-N 2405 was spin coated on a silicon wafer,

prebaked and DUV exposed and is referred to as prepared. The photoresist was postbaked afterwards at 150 °C, 300 °C and 450 °C, respectively.

The deviation of the PSD curve after postbake in comparison to the PSD curve of the as prepared surface is an amount of surface degradation in regard to the spatial frequency. Fig. 5.5 indicates a preservation of the initial surface roughness with about 0.35 nm rms during postbaking at 150 °C. However, for higher temperatures a degradation is observed. In particular, the PSD deviation after 300 °C is slightly and after 450 °C significantly increased over the whole spatial frequency range. The strongest degradation is obtained at 450 °C postbaking. As a consequence, the roughness is increased to values of 0.45 nm rms after 300 °C postbaking temperature and 0.7 nm rms after 450 °C postbaking temperature, respectively.

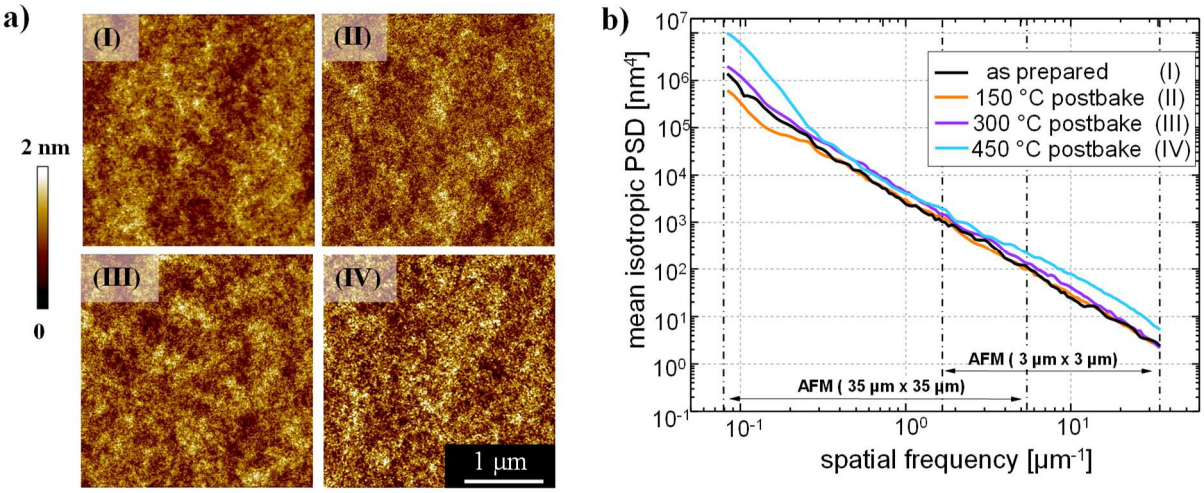


Fig. 5.5: a ) AFM measurements (3 µm x 3 µm) of negative photoresist ma-N 2405 before (I) and after different postbaking temperatures at 150 °C (II), 300 °C (III) and 450 °C (IV), respectively. b) PSD function calculated on the basis of the AFM measurements [107]

Especially above 3 $\mu m^{-1}$ and below 0.3 $\mu m^{-1}$ the PSD deviation of the 450 °C treated sample is strongly increased. These deviations correlate to surface features with sizes below 330 nm and above 3.3 µm, respectively. A maximum deviation of approximately 1 dec is obtained at 0.1 $\mu m^{-1}$. Due to progressive polymer degradation, areas with weaker bonds in the chemical structure of the polymer may preferentially be cracked. Thus, the layer thickness decreases irregularly and consequently surface features of ≥ 3 µm lateral size are formed [143,144,158-162]. The chosen temperature of 300 °C correlates with the beginning of novolak degradation. The primary degradation route of phenol-formaldehyde resins is a thermo-oxidative process, regardless of whether the resin is exposed in air or inert environment [148,163]. During

degradation, oxidative degradation and polymer fragmentation reactions are seemingly in competition [157,163-165]. At that stage the polymeric backbone is cracked and fragments of different sizes start to evolve. With progressive decomposition, the formation of larger fragments increases. These fragments leave voids in the surface of the photoresist layer with different sizes and may cause the roughness increase in the spatial frequency range above 3 $\mu m^{-1}$ [157,166].

This result is of major importance, since the degradation mechanism can also be expected to appear during ion beam treatments, if the heat dissipation is not sufficient. To obtain reliable, reproducible results, ion beam investigations were carried out with a water-cooled sample holder. Furthermore, the samples were mounted with aid of a heat-conducting grease to allow a good thermal contact during ion beam processing. To avoid too high ion current densities, the working distance, i.e. the spacing between ion source and sample, was usually chosen >50 mm. From the results obtained, a postbaking temperature of 150 °C has been identified to be optimal, since the initial roughness is preserved and no novolak degradation occurs.

Additionally, GC/MS measurements were performed to specifically indicate the organic compound releasing during postbaking of the crosslinked photoresist layer (see Fig. 5.6). The strong peak at approximately 78 °C corresponds to the mass spectrum of the organic solvent anisole and is almost completely removed after postbaking. The peak corresponding to the mass spectrum of cyclopentanone is located at approximately 51 °C. Since the change in total ion current intensity for cyclopentanone is small compared to anisole, the section is drawn enlarged as marked in Fig. 5.6a. After postbaking the intensity of cyclopentanone is further decreased. Consequently, remaining amounts of organic solvent after prebake are almost completely removed during postbaking at 150 °C.

DSC measurements shown in Fig. 5.6b indicate two irreversible reactions within the photoresist layer since after the first heating run to 250 °C and subsequent cooling to room temperature both endothermic and exothermic peaks disappear. The endothermic peak of the first heating run has an onset temperature of 21 °C and a peak temperature of approximately 60 °C. The exothermic peak is characterized by a peak temperature of 205 °C and an onset of 170 °C. The endothermic peak may be attributed to solvent evaporation reactions already observed in the TGA and GC/MS measurements (see Fig. 5.4 and Fig. 5.6a) [152,167].

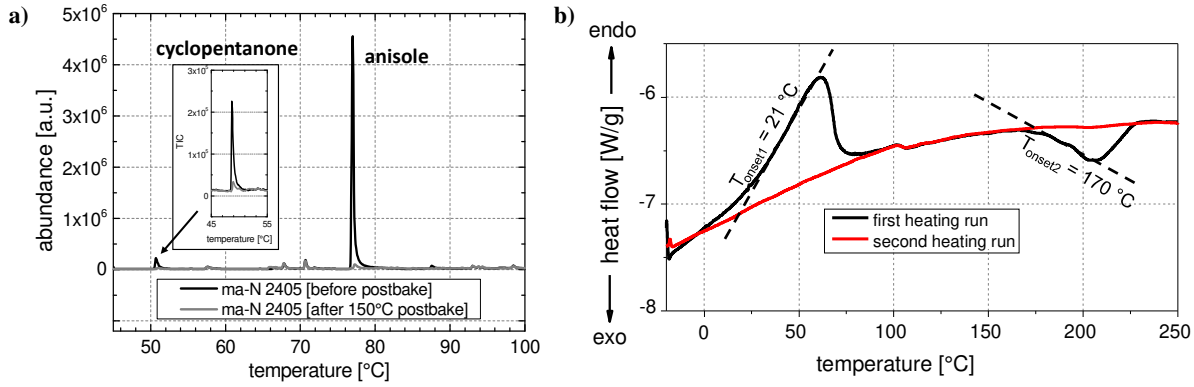


Fig. 5.6: a) Temperature dependent chromatogram of the spin coated, prebaked and UV exposed ma-N 2405 resist film before and after hardbaking at 150 °C. b) DSC measurement of the liquid negative tone resist ma-N 2405 after exposure and after exposure and drying in a compartment dryer at 100 °C for 3h. Both measurements were performed at a heating rate of 10 °C/min

Results of DSC analysis are in good agreement with TGA and GC/MS measurements. Remaining organic solvent evolves below 150 °C. The exothermic peak of the DSC measurement may advert the beginning of the thermo-oxidative degradation mechanism proposed by Conley et al. [157,163] or the decomposition of remaining photoactive compound that did not react during the UV exposure [167].

In the following, the photoresist preparation includes spin coating, prebaking at 90 °C, DUV exposure and postbaking at 150 °C, unless specified otherwise. Hereby prepared photoresist layers are referred to as initial photoresist surface.

## 5.3 Influence of process gas composition

In section 4.1.2 it was shown, that during RIBE machining with $N_2$ the initial roughness of RSA Al905 is exceedingly well preserved up to 1 µm machining depth. Moderate surface degradation was observed after 2 µm machining depth. Additionally, the initial aluminium roughness is preserved up to 400 nm machining depth during irradiation with $O_2$ [34,37].

In the following, the photoresist layer is irradiated using both nitrogen and oxygen gases at normal ion incidence with a special focus on roughness evolution and modification of the polymer structure. Additionally, RIBE investigations with fluorine-containing gases are also examined, since an increased durability resulting from a modification of the polymer structure during irradiation with fluorine-containing species was reported [143,161,168].

### 5.3.1 Influence on roughness evolution during ion beam irradiation of the photoresist layer

Fig. 5.7a shows AFM images of the initial photoresist layer and after irradiation with $O_2$, $N_2$ and $CHF_3$ removing 210 nm, 240 nm and 150 nm material, respectively. The AFM images identify, that no significant difference is observed after RIBE machining with each processing gas compared to the initial surface. However, the PSD functions in Fig. 5.7b indicate a slight increase in both PSD functions in the microroughness regime of the surface irradiated with $O_2$ and $CHF_3$, respectively. The increase seems to be attributed to the formation of small irregularities distributed over the whole surface as illustrated in Fig. 5.7a. However, with nitrogen gas the initial surface roughness is mainly preserved during RIBE machining.

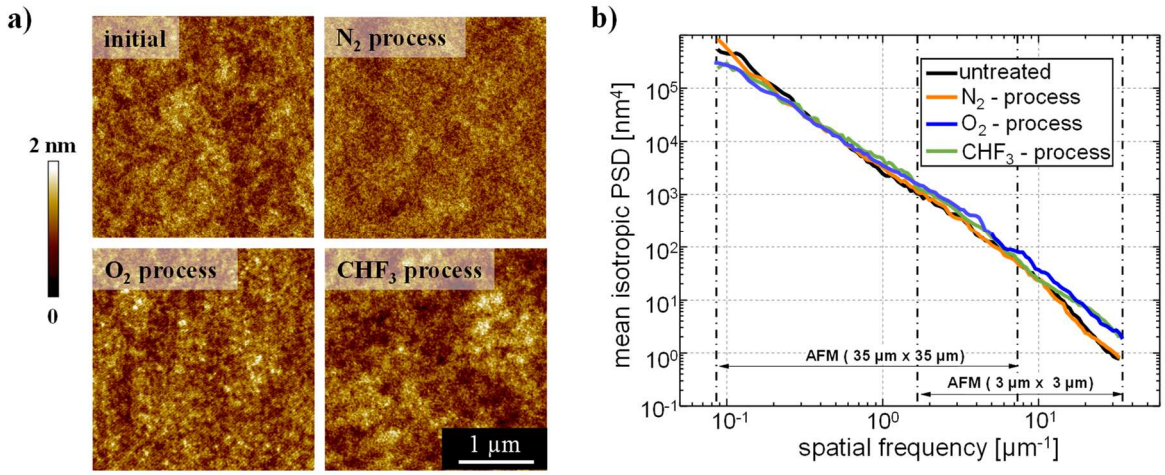


Fig. 5.7: a) AFM images (3 µm x 3 µm) of the initial photoresist surface and after RIBE machining with $N_2$, $O_2$ and $CHF_3$ operating gas with corresponding PSD functions for each operating gas shown in b)

The chemical composition analyzed by XPS measurements (not shown here) reveal a highly modified photoresist surface during RIBE machining. When $N_2$ gas is used, $CN_x$ groups are formed and concurrently $CO_x$ groups are remarkably reduced. In addition, carbon single bonds are partially reorganized to graphitized carbon. During RIBE machining with $CHF_3$ gas, $CO_x$ and $CN_x$ groups are reduced and concurrently $CF_x$ groups are drastically increased. Known from literature, fluorine containing gases are mainly used for photoresist materials since fluorine is strongly bound by covalent bonds within the polymer matrix and therefore the stability against ion beam irradiation is increased [143,168].

However, from a technical point of view, operating with fluorine-containing gases like $NF_3$ or $CHF_3$ causes several problems. During processing, i.e. while the ion source is running, highly stable process conditions are necessary. Though, the ion source, in particular the screengrids, are covered with a thin nonconductive layer leading to flash-arcs and unstable process conditions when the ion source is running longer than 1-2 hours or after once cooled down. Note, a source stabilization period of about 1 hour is usually required after putting the ion source in operation. Hence, stable ion source operation with fluorine-containing process gas is hardly to realize.

### 5.3.2 Dependency of the process gas on the selectivity

Corresponding to the RIBE investigations, the material removal rates of the photoresist layer and aluminium substrate were calculated via equation (2), depending on the process gas used (see Fig. 5.8). In addition, the selectivity is marked in blue. Fig. 5.8 shows, that the material removal rates strongly depend on the operating gas used.

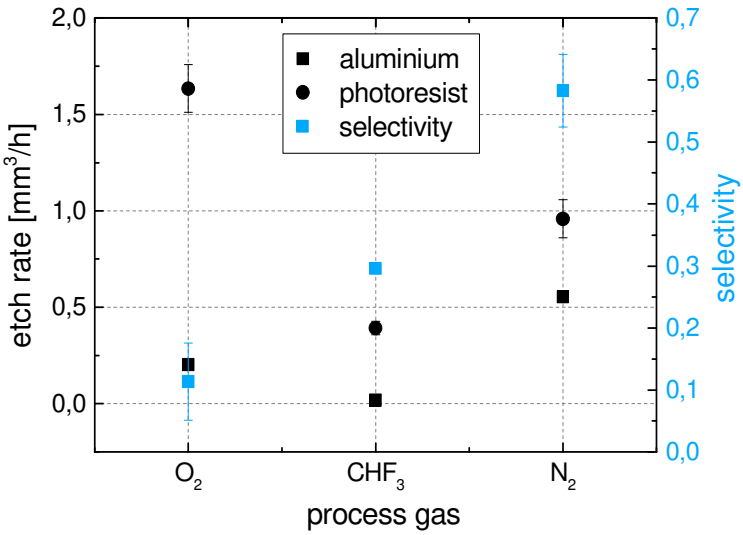


Fig. 5.8: Etch rate dependence of photoresist ma-N 2405 and aluminium alloy RSA Al905 on operating gas $O_2$, $CHF_3$ and $N_2$ and the resulting selectivity values

For $O_2$ gas, the material removal rate of the photoresist layer is approximately eight times higher than for aluminium. The resulting average selectivity is averaged about 0.12. For $CHF_3$ gas both material removal rates of aluminium and photoresist are quite low, and the selectivity is enhanced to about 0.3. The highest selectivity can be achieved using $N_2$ resulting in an achievable range of about 0.55 - 0.65. Additionally, higher material removal rates are

achievable when $N_2$ is used. Consequently, further investigations are carried out with $N_2$ due to the highest selectivity and roughness preservation of both photoresist and aluminium.

## 5.4 Influence of the ion energy on the selectivity

The curve progression of calculated sputtering yields for many ion-target combinations agree mostly well with experimental erosion velocities obtained in a wide range of ion energies from threshold to MeV ranges. During low-energy ion irradiation used within this study (< 2 keV), the etch rate generally increases with increasing ion energy [40-44,169,170]. Fig. 5.9a shows the dependence of the ion beam energy used during $N_2$ RIBE machining on the resulting material removal rates for photoresist and aluminium.

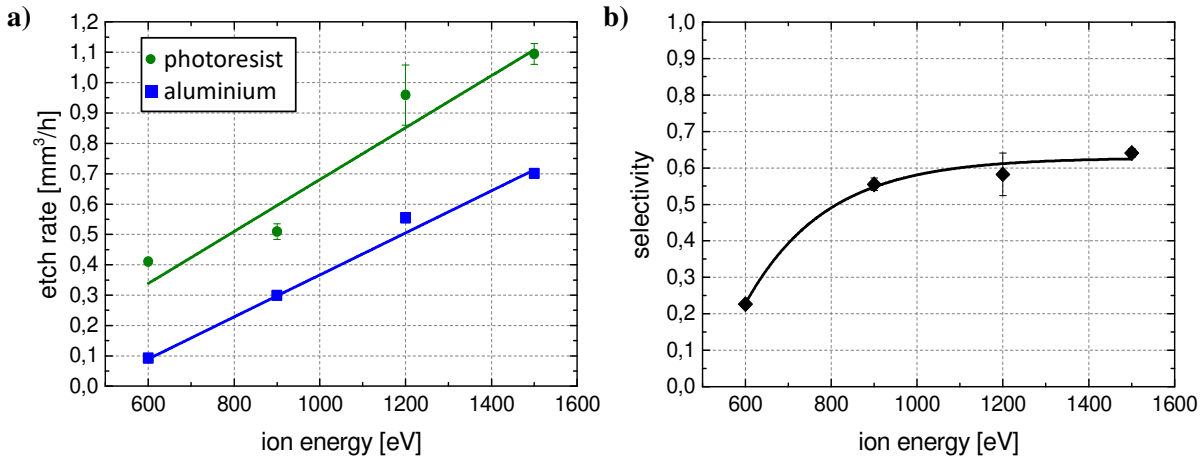


Fig. 5.9: a) Dependence of the ion energy on the etch rate of photoresist and aluminium with the resulting selectivity shown in b)

The photoresist layer and aluminium substrate were bombarded with the energetic ions separately, with a material removal depth of about 500 – 600 nm for aluminium and 60 – 100 nm for the photoresist layer, respectively. The etch rate increases with increasing ion energies for both materials, but with lower values for aluminium. The calculated selectivity shown in Fig. 5.9b reveals an increase with increasing ion energy reaching a plateau at about 1000 eV. At energies >1000 eV the selectivity hardly rises any further. Consequently, ion beam planarization investigations are carried out at higher ion energies of >1000 eV in the following.

## 5.5 Ion beam irradiation of the photoresist layer with nitrogen at different material removal depths

The effect of ion beam irradiation at normal ion incidence on the resist layer is investigated with a special focus on the surface evolution and the temporal stability of the removal process. In Fig. 5.10 AFM measurements and PSD diagrams of the photoresist layer irradiated with $N_2$ at 1.2 keV with stepwise increased material removal depths are presented.

After 76 nm material removal, the formation of particles and a granular structure with some ten nanometers in diameter is observed corresponding to an increased PSD deviation above 8 $\mu m^{-1}$ spatial frequency. The emerging roughness seems to be transferred into the underlying photoresist bulk and intensifies with increasing etching depth. A contrary effect is observed in the spatial frequency range of 0.9 $\mu m^{-1}$ to 8 $\mu m^{-1}$. With increasing material removal, the PSD curve is decreased conforming to a perpetual flattening of the differences in height observed in the AFM images. This effect has also been observed in reactive ion etching (RIE) experiments using $CHF_3$ processing gas performed by Schuster et al. [161]. The AFM images after RIE machining with $CHF_3$ process gas exhibited a similar granular structure. Simultaneously, a smoothing over the whole measured area of 3 µm x 3 µm was observed.

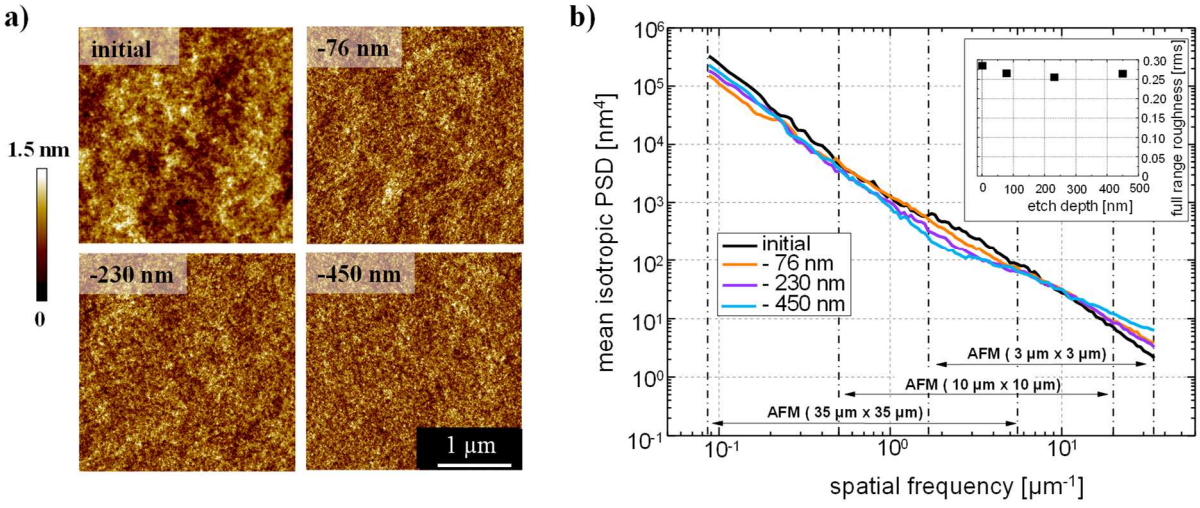


Fig. 5.10: a) AFM measurements (3 µm x 3 µm) of negative photoresist ma-N 2405 before and after RIBE ($N_2$ operating gas, 1.2 keV) with machining depths of 76 nm, 230 nm and 450 nm and b) corresponding PSD functions calculated on the basis of the AFM measurements with scan sizes of 3 µm x 3 µm, 10 µm x 10 µm and 35 µm x 35 µm [107]

Referred to Sumiya et al., the schematic of a two-stage photoresist degradation mechanism is consistent with the present observations [143]. A certain roughness is initially introduced and constantly transferred into the underlying material during subsequent etching (see Fig. 5.10a). In the first stage, a modified layer is formed on top of the photoresist surface. During that period selective oxygen removal occurs and a graphitic layer is formed. In the second period, a steady-state etching takes place where the spatial distribution of the surface roughness changes little. The calculated material removal rates at the various etch depth depicted in Fig. 5.10 are shown in Fig. 5.11. As a result, the material removal rate is nearly constant up to 450 nm material removal, enabling controllable process parameter during the planarization process. Furthermore, the etch rate is independent on the atmosphere of the postbaking conditions. The experiments were repeated on a photoresist layer postbaked in a vacuum oven at 150 °C (not shown here), revealing consistent material removal rates.

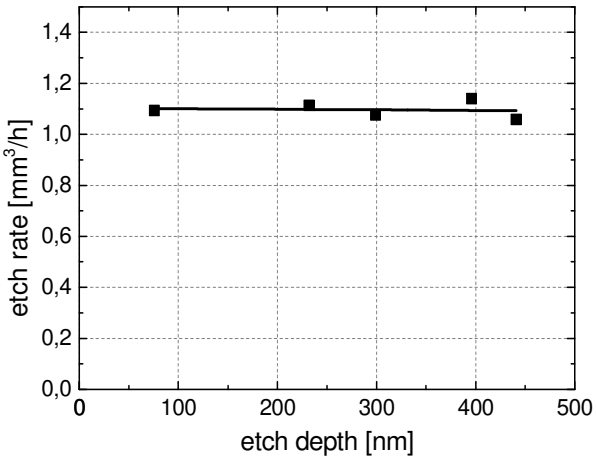


Fig. 5.11: RIBE volume etch rate of negative photoresist ma-N 2405 depending on etching depths [107]

# 5.6 Conclusions

Several commercially available negative and positive tone photoresist layers were examined for ion beam planarization process of aluminium mirror optics. In the beginning of this section, different types of photoresist layers were analyzed in case of roughness evolution and resistivity during the interaction of low energy ion beams with the surface. The most promising results were achieved using the negative tone ma-N 2405 photoresist.

For successful planar surface transfer during IBP, the application steps of the photoresist layer were investigated in detail. In summary the results are:

- Prebaking and postbaking of the photoresist layer are relevant to evaporate remaining organic solvent. During pre- and postbaking the thermal resistance of the photoresist layer is increased to avoid thermal degradation during ion beam irradiation, irrespective of the atmosphere during baking.
- DUV exposure is important to induce the crosslinking of the PAC and novolak matrix to improve the stability during the IBP processing and therefore avoiding an increase in roughness during ion beam irradiation.
- Ion beam irradiation investigations with different process gases revealed a roughness preservation when $N_2$ is used. Additionally, the selectivity for nitrogen operating gas is most promising for IBP process.
- Higher ion energies of > 1000 eV are chosen for improvement of the selectivity. Lower ion energies lead to decreased material removal rates of photoresist and as well as lower selectivity values.
- Proper photoresist preparation with prebaking at 90 °C, DUV exposure, and postbaking at 150 °C enabled steady-state material removal rates and roughness preservation during ion beam irradiation.

# 6 Ion beam planarization of optical aluminium surfaces RSA Al6061 and RSA Al905

Ion beam planarization with the aid of a sacrificial layer is examined for surface smoothing in the waviness/roughness regime. In the following section 6.1 the optimized photoresist preparation sequence shown in section 5 is applied on aluminium alloys RSA Al905 and RSA Al6061 in order to investigate the ion beam planarization capability of SPDT aluminium alloys. A two-step process route is applied including iteratively $N_2$ IBP and direct ion beam smoothing with $O_2$. The influence of potentially photoresist residues resulting from the eroded layer on the subsequently applied $O_2$ finishing procedure is analyzed. In addition, RSA Al6061 showed an enhanced surface degradation during ion beam irradiation with $N_2$ in comparison to RSA Al905 (section 4.1.1). Hence, the influence of the different alloying elements on the microroughness evolution and the formation of the modified surface layer is investigated. The described two-step process route is under revision in [107] and is described within the patent application for “Verfahren zum Glätten von Oberflächen”.

## 6.1 Photoresist application on SPDT aluminium alloys

In order to find optimum photoresist preparation conditions in section 5, the photoresist layer was applied on smooth silicon wafers. In contrast, diamond turned aluminium samples RSA Al905 and RSA Al6061 reveal surfaces with periodical turning structures. To achieve the best planarization results, the photoresist should fill out the open spaces between those structures and form an ultra-smooth top surface without any residual topography. Following the planarization behavior of 500 – 600 nm thick photoresist layers after deposition by spin coating is investigated. Fig. 6.1 shows AFM images and PSD functions of the thin photoresist layer coated on an aluminium substrate before and after postbaking.

The 3 µm spaced turning marks present on the initial aluminium surface correspond to the PSD deviation at 0.3 $\mu m^{-1}$. When the photoresist layer is applied, the turning structures are almost fully embedded and a smooth surface is revealed as it is proven by the PSD curve where the deviations corresponding to the turning marks are almost completely removed. In contrast, the periodical structures become apparent to some extent again when postbaking is applied. This is

due to the shrinkage of the 560 nm thick layer to about 500 nm during postbake, the turning structure is regained into the thin layer topography.

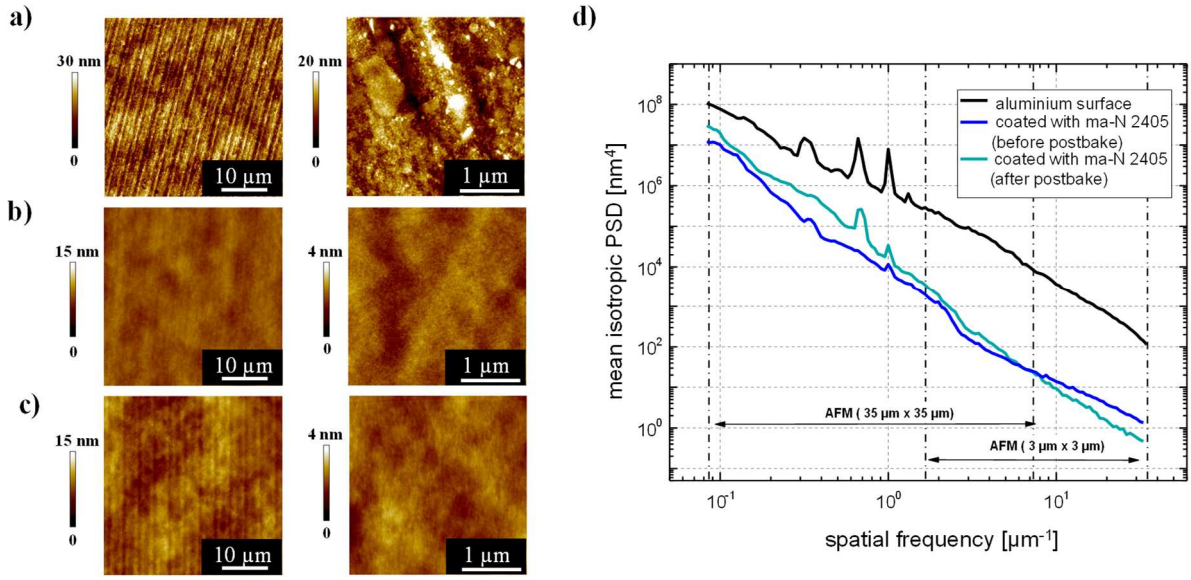


Fig. 6.1: a) AFM measurements of a) RSA Al905 sample surface, b) additionally spin-coated with 560 nm negative photoresist ma-N 2405, prebaked and UV exposed and c) after postbaking at 150 °C for 10 minutes. d) PSD function calculated on the basis of AFM measurements. Note, the height ranges for the AFM images differ before and after coating [107]

## 6.2 Ion beam planarization

Hereafter, ion beam planarization of RSA Al905 and RSA Al6061 are elucidated. Since the selectivity is not ideally 1, but about 0.55-0.66 (section 5.4), a sequence of two subsequent IBP runs was examined to improve the smoothing result.

Additionally, direct ion beam etching experiments were performed on both aluminium alloys before IBP to calculate the volume etch rates. Moreover, before each planarization run the etch rate of the photoresist layer, coated on a silicon wafer, was examined to calculate the selectivity. The maximum etch depth during IBP was chosen with respect to the initial photoresist thickness of about 500 nm and the height of the turning mark structures. Hence, a maximum aluminium removal of 50 nm was not exceeded during processing.

The ion beam process parameter for ion beam planarization investigations are summarized in Table 6.1. The untreated aluminium surfaces are referred to as initial surface and the surfaces after the first and second ion beam planarization process are referred to as first and second run, respectively.

Table 6.1: Ion beam process parameters with corresponding etch rates and selectivity of RSA Al905 and RSA Al6061

| Material/process | | Process gas | Process pressure [Pa] | FWHM [mm] | Beam current [mA] | Etch rate [mm³/h] | Selectivity |
|---|---|---|---|---|---|---|---|
| RSA Al905 | | $N_2$ | $3.8 \times 10^{-3}$ | 9.9 | 1.94 | 0.54 | |
| RIBE planarization | 1st run | $N_2$ | $3.8 \times 10^{-3}$ | 9.8 | 1.97 | | 0.52 |
| | 2nd run | $N_2$ | $1.6 \times 10^{-3}$ | 8.4 | 1.89 | | 0.55 |
| RSA Al6061 | | $N_2$ | $1.5 \times 10^{-3}$ | 9.0 | 1.89 | 0.68 | |
| RIBE planarization | 1st run | $N_2$ | $1.5 \times 10^{-3}$ | 8.6 | 2.02 | | 0.63 |
| | 2nd run | $N_2$ | $1.7 \times 10^{-3}$ | 9.4 | 2.14 | | 0.59 |

## 6.2.1 Iterative nitrogen processing of RSA Al905

The topography measurements in Fig. 6.2a represent the initial RSA Al905 aluminium surface. Fig. 6.2b/c represent the surface after first run and second run, respectively. The dashed lines in the AFM images represent the positions for the midline of the cross-section profiles illustrated in Fig. 6.3b. The effect of the planarization process on RSA Al905 surface roughness, segmented into waviness/roughness and microroughness is summarized in Table 6.2, and the corresponding spatial wavelength ranges are marked in the PSD diagrams in Fig. 6.3a.

The initial surface is dominated by a periodic waviness pattern caused by SPDT tool including turning marks with an average height of (23.6 ± 0.8) nm and mid-spatial frequency errors with a spatial wavelength of approximately 220 µm (see Fig. 6.2a WLI image). By way of illustration, relevant turning mark spaces and etch pit surface density is marked in Fig. 6.2. Whereas the mid-spatial frequency errors are not fully embedded by the thin photoresist layer, a distinct improvement of these surface errors during ion beam planarization was barely expected. Hence, the 220 µm spaced surface errors are slightly smoothed during processing but remain almost unchanged (see Fig. 6.2a-c WLI images). As a result, the bump in the PSD spectrum in the spatial frequency range of 0.0024 $\mu m^{-1}$ to 0.007 $\mu m^{-1}$ is barely reduced after one planarization run. The deviation after the second planarization run is negligible. The turning marks located in the high-spatial frequency range are characterized by a period of 3 µm with several superstructures of 1.4 µm, 1 µm and 0.7 µm. These turning marks are considerably reduced in height to average (7.9 ± 0.7) nm with smoothed edges after the first run. As a consequence, the strong deviations in the spatial frequency range of about 0.3 $\mu m^{-1}$ to 2 $\mu m^{-1}$ with several maxima at 0.3 $\mu m^{-1}$, 0.7 $\mu m^{-1}$, 1 $\mu m^{-1}$ and 1.4 $\mu m^{-1}$ are significantly decreased. The PSD deviation at 1.4 $\mu m^{-1}$, reflecting one superstructure, is almost completely removed.

Additionally, the formation of single etch pits with sizes of a few hundred nanometers and particles with a mean diameter of 90 nm are observed. The turning marks are further reduced to an average height of (4.2 ± 0.5) nm after the second run, but the formation of etch pits is increased with slightly enhanced diameters in the sub-micrometer range (see Fig. 6.2c).

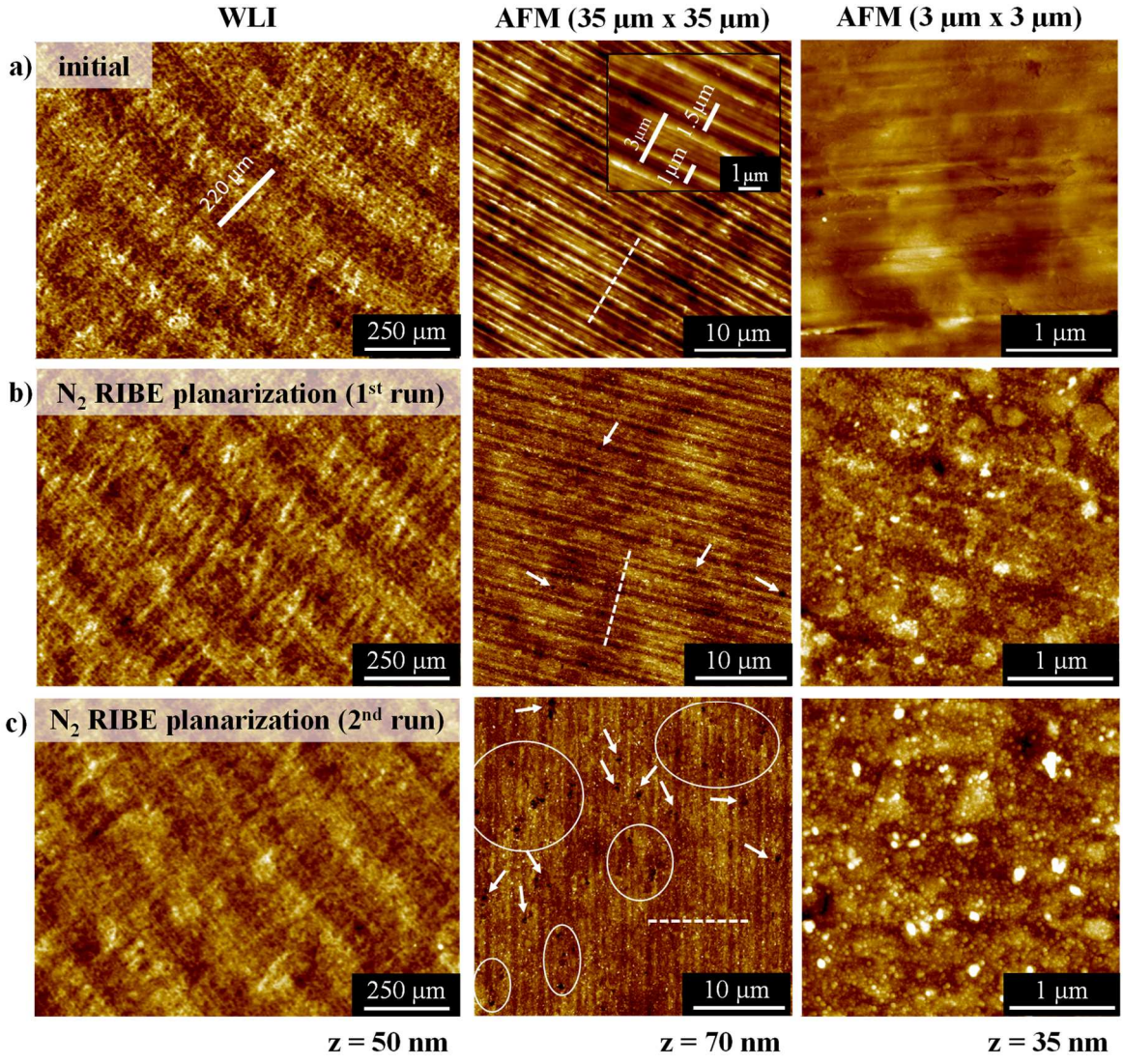


Fig. 6.2: WLI (5x objective) and AFM (3 µm x 3 µm and 35 µm x 35 µm) measurements of surface topography of RSA Al905 sample of the a) initial surface and after b) the first run and c) second run RIBE planarization. The image height scale is indicated by the z-value [107]

Fig. 6.3b shows an average cross section profile of the initial surface and after the first and second run, respectively. For a more detailed discussion of turning mark evolution, averaged cross section profiles are generated by defining an average area of about 300 parallel cross-sections. During the first run, the turning marks are reduced in height by about 66.5 % with smoothed edges. Due to a selectivity of 0.52 of the first planarization run, the height reduction

is indeed larger than expected. During the second run, a further reduction of 44.5 % in height is observed, which corresponds to a selectivity of 0.55. The increased formation of statistically distributed particles and pits on the surface may be one reason for the slightly decrease in height reduction. Additionally, the second planarization run was performed on an aluminium surface already irradiated with $N_2$ during the first run. As shown in section 4.1.2, instantly during the first 50 nm material removal an about 15 nm thick nitride layer is formed. Consequently, the etch rate of the aluminium and the resulting selectivity might have changed.

Nevertheless, as summary of the planarization behavior of RSA Al905 surfaces by RIBE with 1.2 keV nitrogen ions it can be stated, that the turning marks are successfully reduced by overall 82 % after two planarization runs.

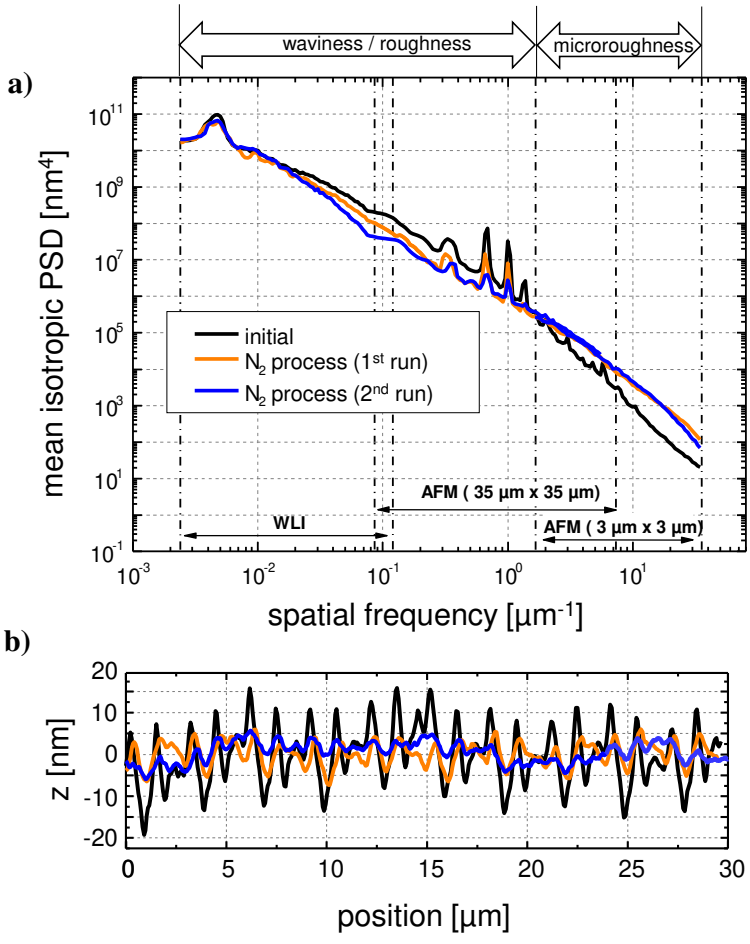


Fig. 6.3: a) PSD spectra before and after two planarization runs on RSA Al905 sample. b) Averaged cross section profiles of Aluminium RSA Al905 sample calculated on the basis of AFM images of the initial surface (black), after the first run (orange) and the second run (blue) [107]

In contrast, the PSD spectrum is increased in the spatial frequency range above 1.6 $\mu m^{-1}$. A maximum deviation of about 1 dec is obtained, correlating to a formation of a nanoscopic

granular structure with several distributed particles. Some of these larger particles appear to have been caused by the aggregation of the granules. Consequently, the microroughness is increased after IBP to (3.2 ± 0.3) nm rms after the first run and (3.3 ±0.3) nm rms after the second run compared to the initial roughness values of approximately (2.2 ± 1.2) nm rms.

The microroughness remains unchanged after the second run compared to the first run. Note, that similar nanoscopic granules were observed after removing 50 nm during direct $N_2$ RIBE machining of RSA Al905, which was discussed in section 4.1.2. Consequently, irrespective of the ion beam finishing technique applied, one has to deal with the specific structure formed when $N_2$ gas is used.

Table 6.2: Surface roughness values of Al905 divided into waviness/roughness and microroughness and the full range roughness as well as the corresponding heights of the turning mark structures

| RSA Al905 | Microroughness [nm rms] | Roughness + waviness [nm rms] | Full range [nm rms] | Turning mark height [nm] |
|---|---|---|---|---|
| Untreated | 2.2 ± 1.2 | 9.5 ± 1.4 | 9.7 ± 1.6 | 23.6 ± 0.8 |
| $N_2$ planarization (1st run) | 3.2 ± 0.3 | 5.9 ± 0.7 | 6.8 ± 0.8 | 7.9 ± 1.3 |
| $N_2$ planarization (2nd run) | 3.3 ± 0.3 | 5.1 ± 1.1 | 5.9 ± 1.1 | 4.3 ± 0.5 |

For further analysis of the particulates, that are observed on RSA Al905 after ion beam planarization process, the local composition distribution after RIBE machining was monitored by SEM-EDX mapping (see Fig. 6.4). After the first processing run, particularly Cu and Ni precipitates are revealed irregularly distributed over the aluminium surface. Preferential sputtering of Al in Al-Cu alloys was also observed by Whetten et al. [171], Chu et al. [172] or Betz [173]. An enrichment of Ni during sputtering of Al-Ni alloys was found by Stefanov et al. [174]. Consequently, the particle formation observed in the present study is assumed to result from the reduced sputter erosion of these precipitates compared to the aluminium matrix [171].

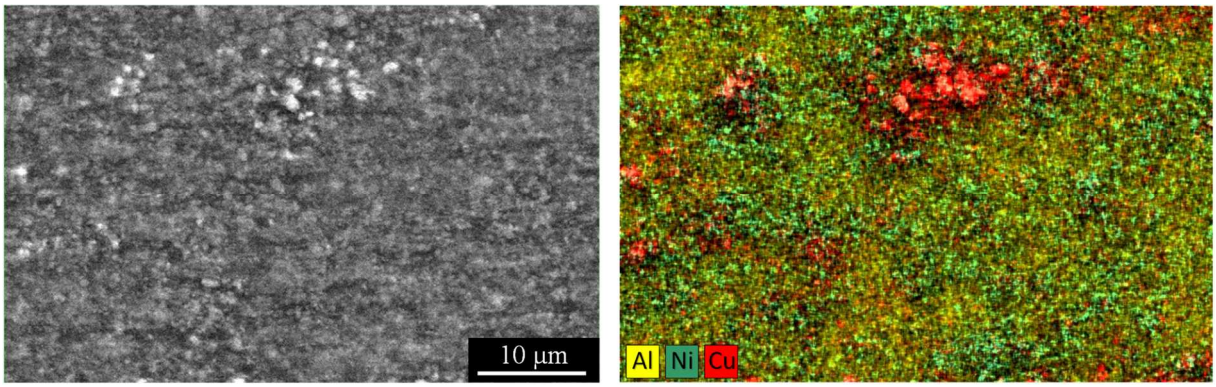


Fig. 6.4: SEM and SEM-EDX mapping image of an aluminium RSA Al905 alloy after the first run ion beam planarization revealing significant Cu and Ni precipitations [107]

## 6.2.2 Iterative nitrogen processing of RSA Al6061

The same process route as described above was applied on a RSA Al6061 surface. The initial surface is dominated by approximately 1.3 µm spaced turning marks with (2.9 ± 0.3) nm in height, corresponding to the PSD deviations with maxima at 0.8 $\mu m^{-1}$, 1.2 $\mu m^{-1}$ and 1.6 $\mu m^{-1}$ (Fig. 6.5 and Fig. 6.6a).

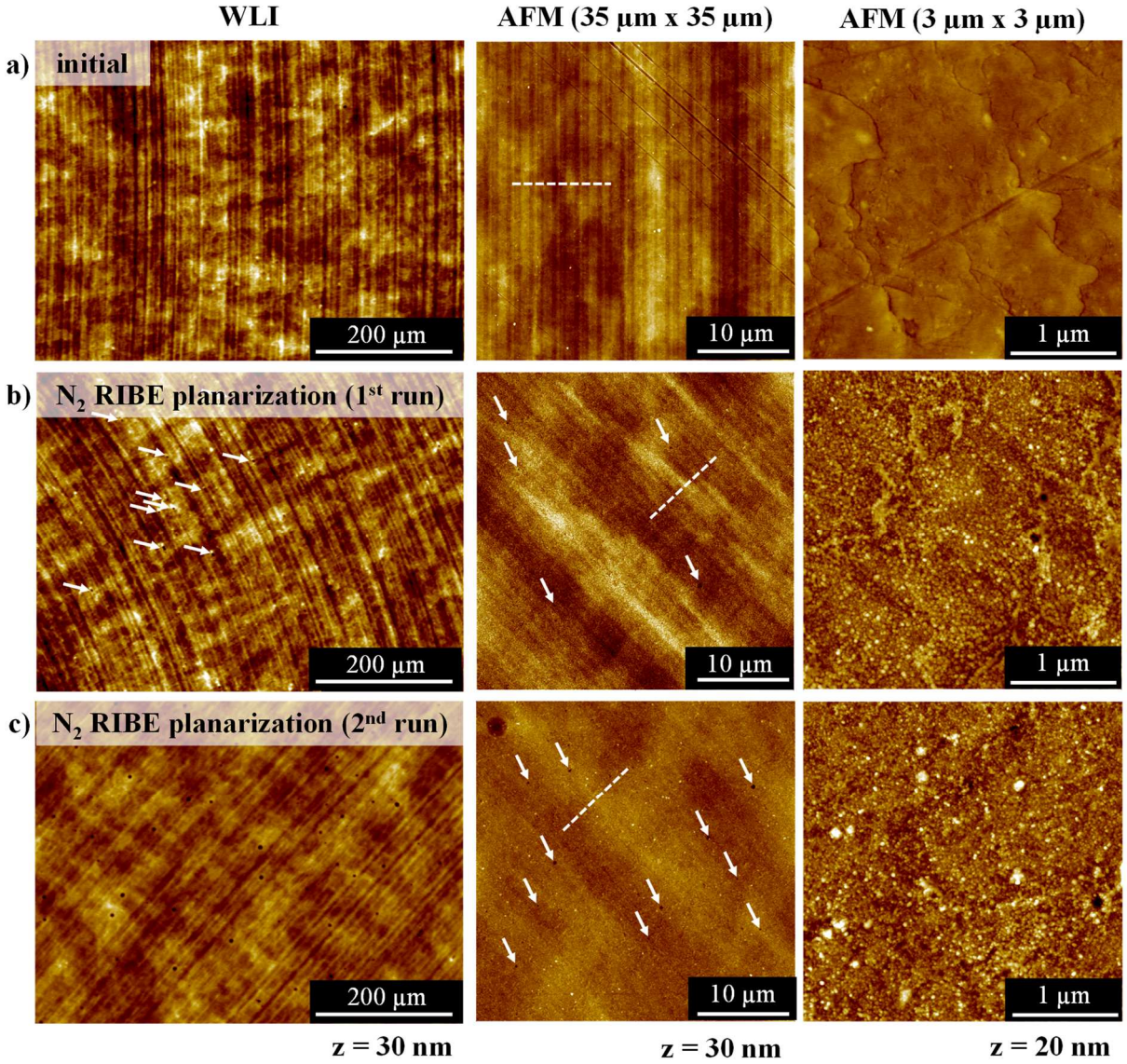


Fig. 6.5: WLI (10x objective) and AFM (3 µm x 3 µm and 35 µm x 35 µm) measurements of RSA Al6061 sample a) before and after b) the first run and c) second run RIBE planarization. The image height scale is indicated by the z-value [107]

Furthermore, larger spaced turning marks with several nanometers in height correlate to the PSD deviations in the spatial frequency range of approximately 0.024 $\mu m^{-1}$ to 0.1 $\mu m^{-1}$. The initial surface roughness of the RSA Al6061 surface is already smaller compared to RIBE

investigations on RSA Al905 (section 6.2.1). The effect of the planarization process on RSA Al6061 surface roughness, segmented into waviness/roughness and microroughness is summarized in Table 6.3 and the corresponding spatial wavelength ranges are marked in the PSD diagrams in Fig. 6.6a. Fig. 6.5 shows, that after the first run the formation of a few etch pits concentrated along the turning marks with diameter of a few micrometer is observed. Additionally, the etch pit formation is increased after the second run with similar mean diameter. The turning marks are reduced in height to an average value of (1.8 ± 0.3) nm after the first run.

Table 6.3: Surface roughness values of aluminium Al6061before and after one and two runs ion beam planarization divided into waviness/roughness and microroughness, and the full range roughness as well as the corresponding heights of the turning mark structures

| RSA Al6061 | Microroughness [nm rms] | Roughness + waviness [nm rms] | Full range [nm rms] | Turning mark height [nm] |
|---|---|---|---|---|
| Untreated | 1.3 ± 0.6 | 4.7 ± 0.8 | 4.9 ± 0.9 | 2.9 ± 0.3 |
| $N_2$ planarization (1st run) | 2.6 ± 0.2 | 4.2 ± 0.6 | 4.9 ± 0.7 | 1.8 ± 0.3 |
| $N_2$ planarization (2nd run) | 2.5 ± 0.3 | 3.2 ± 0.6 | 4.0 ± 0.7 | < 1 |

As a consequence, the corresponding PSD deviations shown in Fig. 6.6 are decreased in the spatial frequency range of 0.7 $\mu m^{-1}$ to 1.8 $\mu m^{-1}$. The first planarization run reveals a reduction of the roughness in the waviness/roughness regime to (4.2 ± 0.6) nm rms and a contrary increase in the microroughness regime to (2.6 ± 0.2) nm rms. Consequently, the full range roughness of (4.9 ± 0.9) nm rms remains unchanged after the first planarization run. After the second planarization run, the turning marks are strongly reduced to height values in the sub-nanometer range. Hence, the PSD deviation at 0.8 $\mu m^{-1}$ is remarkably decreased. Additionally, the PSD deviations at 1.2 $\mu m^{-1}$ and 1.6 $\mu m^{-1}$ almost disappeared after the second planarization run.

The PSD spectrum in the spatial frequency range of 0.01 $\mu m^{-1}$ to 1.6 $\mu m^{-1}$ is decreased during the second run. As a consequence, the waviness is remarkably reduced to (3.2 ± 0.6) nm rms. Fig. 6.6b shows an average cross section profile of the initial surface and after the first and second run, respectively. The 1.3 µm spaced turning marks with (2.9 ± 0.3) nm height on RSA Al6061 are almost completely removed after two planarization runs. However, larger-spaced waviness is still apparent on the surface, since this is situated outside the effective planishing range of the photoresist. In the microroughness range a similar PSD deviation of maximum about 1 dec is obtained, as already observed on RSA Al905 (chapter 6.2.1). The

nanogranular structure of RSA Al6061 represented in AFM measurements with the small scan size of 3 µm x 3 µm is still apparent after the second planarization run. The small particles seem to accumulate together at the grain boundaries. The particles formed after the second run are increased in size and additionally some consist of smaller particles clumped together, resulting in several hundred nanometer size.

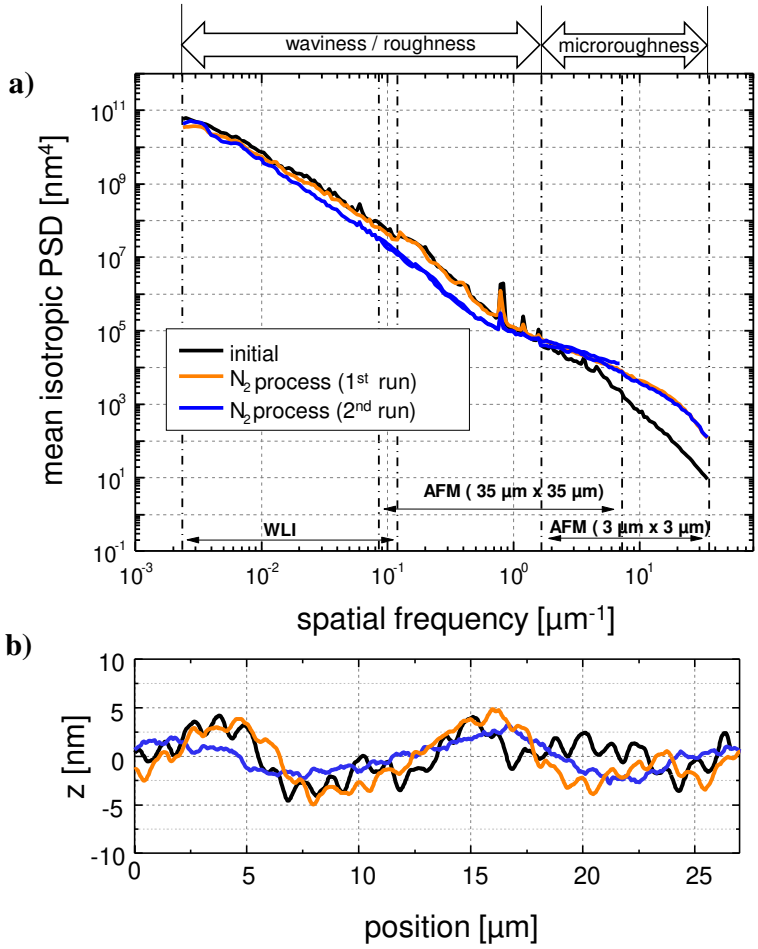


Fig. 6.6: PSD spectra before and after both RIBE planarization runs of RSA Al6061 sample. b) Averaged cross section profiles of RSA Al6061 sample calculated on the basis of AFM images of the untreated surface (black), after the first run (orange) and the second run (blue) [107]

As a result of the planarization behavior of RSA Al6061 surfaces by RIBE with 1.2 keV nitrogen ions, the turning marks are also successfully reduced in a comparable ratio as already observed during ion beam planarization of RSA Al905. However, the turning marks on the untreated RSA Al6061 surface were already smaller in height. Consequently, these structures are almost completely removed during processing. In consideration of the different surface qualities of the aluminium samples used for ion beam planarization investigations, comparable results are obtained.

## 6.3 Ion beam direct smoothing

Based on the investigations in chapter 4.2, an optimized ion beam finishing process using oxygen is applied consecutively at two different ion beam energies on both samples depicted in Fig. 6.2 and Fig. 6.5. The ion beam was scanned in a raster path over the surface with a constant velocity of 4 mm/s and 1 mm line pitch within one repetition at 1.5 keV. 4 repetitions are chosen at 0.6 keV on RSA Al905 and at 1 keV on RSA Al6061, respectively. For 1.5 keV RIBE investigations one repetition is chosen, since the detailed analysis in chapter 4.2.2 showed, that the oxide layer formed has already achieved the steady-state thickness of about 16 nm and the reflectivity improvement up to 10 repetitions was similar. For the lower ion energy of 0.6 keV, the penetration depth of oxide within the nitride layer is reduced and oxygen - enrichment at the surface is increased with increasing repetitions reaching steady-state conditions after 3 and 4 repetitions. Additionally, the reflectivity is further improved with increasing scanning repetitions achieving a maximum after 4 repetitions.

The FWHM of the ion beam analyzed before both $O_2$ finishing procedures, is 4.3 mm (RSA Al905) and 3.6 mm (RSA Al6061) with a beam current of 1.68 mA and 1.59 mA, respectively. The effect of the oxygen machining on surface roughness of RSA Al905 and RSA Al6061 is summarized in Table 6.4 and Table 6.5, respectively.

### 6.3.1 RIBE $O_2$ smoothing of RSA Al905

The AFM measurements in Fig. 6.7a represent the RSA Al905 initial surface, after two runs ion beam planarization and after the subsequent oxygen finishing processes. In Fig. 6.7b, the corresponding PSD functions are illustrated. The roughness evolution segmented into microroughness and waviness/roughness as well as the full range roughness is summarized in detail in Table 6.4. After RIBE machining with oxygen, the turning marks corresponding to the deviations in the spatial frequency range of 0.3 $\mu m^{-1}$ - 2 $\mu m^{-1}$ remain almost unchanged. However, their height is slightly increased from (4.3 ± 0.5) nm to (6.6 ± 0.6) nm and (7.0 ± 1.0) nm after the $O_2$ finishing process with 1.5 keV and 0.6 keV beam energy, respectively. No distinct enhanced etch pit formation can be observed, since the etch depth is chosen small. Hence, the RMS roughness in the roughness/waviness regime is kept constant after oxygen finishing at 1.5 keV beam energy. Indeed, the roughness/waviness is slightly increased to (6.2 ± 0.7) nm rms during $O_2$ finishing at 0.6 keV, which might be assumed to

result from marginal surface degradation and slightly more pronounced turning marks after finishing, compared to RIBE investigations at 1.5 keV ion energy.

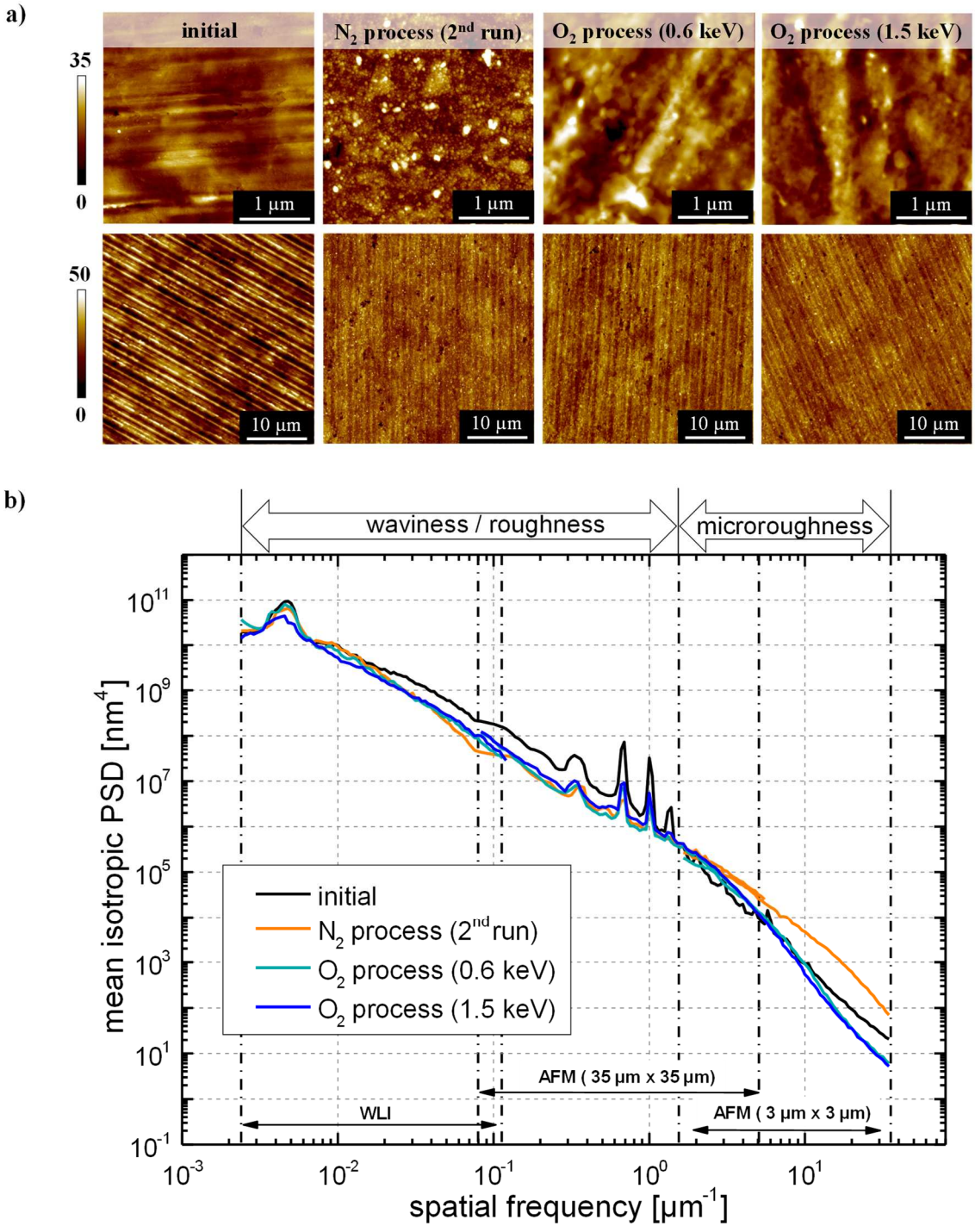


Fig. 6.7: a) AFM measurements (3 µm x 3 µm and 35 µm x 35 µm) of the initial RSA Al905 surface, after the second planarization run and after subsequently applied oxygen process at 0.6 keV and 1.5 keV, respectively. The z-scale is in nm. The corresponding PSD functions are shown in b). Modified in [107]

In contrast, the PSD spectrum is decreased in the spatial frequency range above 2 $\mu m^{-1}$ to maximum 1.5 dec for both ion energies applied, resulting in a remarkably reduction of the microroughness to (2.2 ± 0.6) nm rms and (2.5 ±0.2) nm rms, respectively. Above 10 $\mu m^{-1}$ spatial frequency, the PSD curves are even below the untreated surface. Irrespective of the ion beam energy, the microroughness is drastically reduced while mainly preserving the improved roughness in the waviness/roughness regime as a result of ion beam planarization.

Table 6.4: Surface roughness values of RSA Al905 before machining, after two runs ion beam planarization and subsequent $O_2$ finishing at 0.6 keV and 1.5 keV, respectively. The roughness values are divided into waviness/roughness, microroughness, and the full range roughness

| RSA Al905 | Microroughness [nm rms] | Roughness/waviness [nm rms] | Full range [nm rms] | Turning mark height [nm] |
|---|---|---|---|---|
| untreated | 2.2 ± 1.2 | 9.5 ± 1.4 | 9.7 ± 1.6 | 23.6 ± 0.8 |
| N2 process (2nd run) | 3.3 ± 0.3 | 5.1 ± 1.1 | 5.9 ± 1.1 | 4.3 ± 0.5 |
| O2 process (0.6 kV) | 2.5 ± 0.2 | 5.6 ± 0.7 | 6.2 ± 0.7 | 7.0 ± 1.0 |
| O2 process (1.5 kV) | 2.2 ± 0.6 | 5.2 ± 0.9 | 5.7 ± 1.1 | 6.6 ± 0.6 |

In order to analyze, if photoresist residuals are revealed on the surface and if alloy constituents affect the progress of microroughness evolution and reflection properties, ToF-SIMS experiments are performed. Measurements made in positive mode (not shown here), exhibit similar constituents beyond the surface region after $N_2$ planarization like before machining. However, Cu and Ni precipitates observed after $N_2$ ion beam planarization are reduced during RIBE finishing when oxygen gas is used, since negative mode ToF-SIMS depth profiling reveal $Ni^-$ and $Cu^-$ declining within the $AlO^-$ - rich layer shown in Fig. 6.8. In particular, during $O_2$ RIBE investigations at 1.5 keV, both $Ni^-$ and $Cu^-$ - signals are reduced in the near-surface region. Within the so-called altered top layer, the sputtering behavior of oxides seem rather more complex than sputtering of metals, especially in a multicomponent system such as an alloy [173-176]. Lots of results include the conversion of Cu to $Cu_2O$ [177,178] and Ni to NiO [176,179]. The presence of a thin oxide layer seems to affect the partial sputter erosion of Cu and Ni [180]. Stefanov et al. [174] showed Ni enrichment on the top surface layer during $Ar^+$ ion bombardment and an Al enrichment at the outermost surface during subsequent oxidation experiments at room temperature.

However, the main fractions of Cu and Ni are buried at a depth of about 8 – 16 nm within the nitride as well as in the oxide layers. The changes of those main fractions are negligible between the situation after $N_2$ IBP and after any of both $O_2$ processes. Hence, the influence of the alloy constituents is suggested to be of minor importance for microroughness evolution and the

changes in the optical properties. In accordance, there is no significant etch pit formation observed in the AFM investigations (Fig. 6.7a).

Additionally, the granular structure that occurred after nitrogen machining is removed resulting in the large decrease in the high-spatial frequency range. Consequently, a few nanometers material removal is sufficient to eliminate the nanoscopic granules formed during $N_2$ IBP.

ToF-SIMS measurements shown in Fig. 6.8 additionally indicate a similar oxide - enrichment and nitride - declining transition layer formation during $O_2$ finishing as discussed in chapter 4.2.2. The 15.3 nm thick nitride layer formed during iteratively IBP is similar to direct RIBE investigations with $N_2$. The nitride layer overlapping with an about 7.9 nm thick oxide layer are not independently present on the surface but are existent in an oxynitride combined surface layer with 9.0 nm in thickness. Note, during $O_2$ finishing the oxide layers are significantly enlarged to 14.4 nm (0.6 keV ion energy) and 16.8 nm (1.5 keV ion energy).

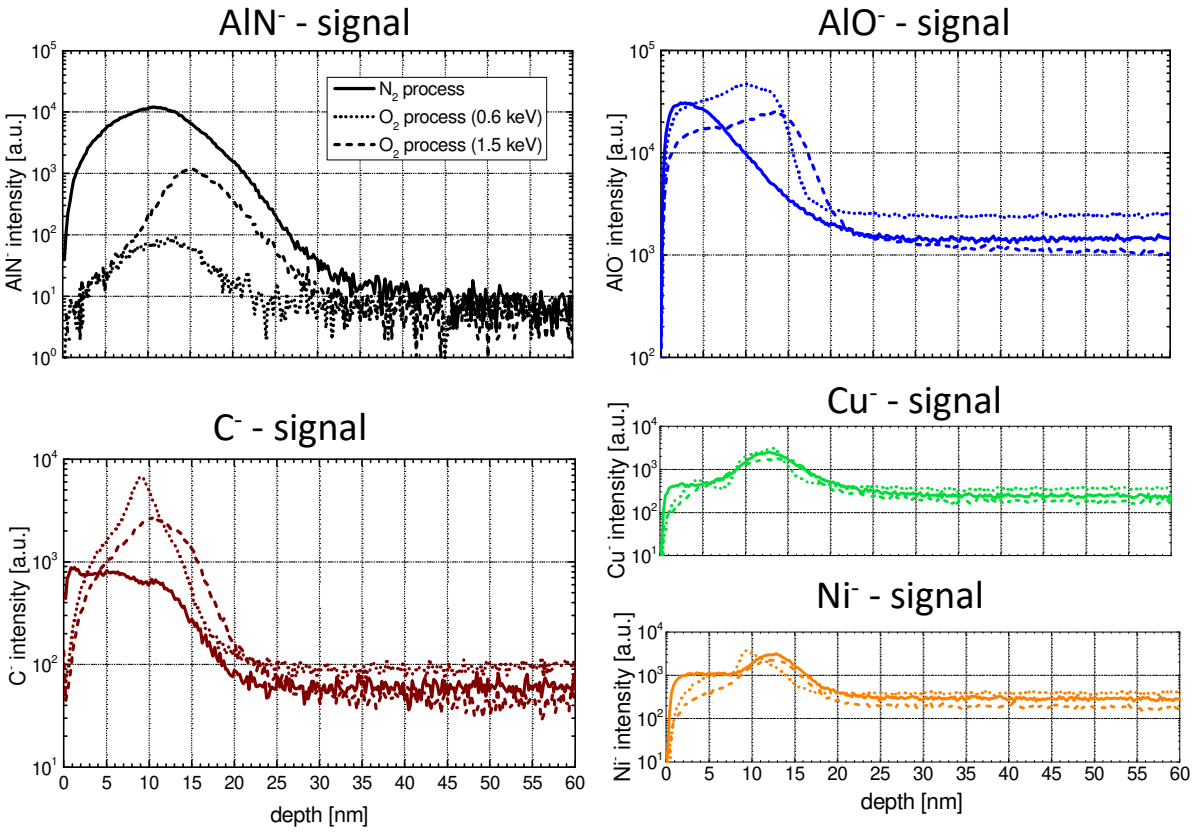


Fig. 6.8: ToF-SIMS depth profiles of RSA Al905 after two planarization runs with nitrogen and after oxygen machining. The extent of a nitride surface layer is represented by the $AlN^-$ signal and the surface oxide layer is represented by the $AlO^-$ signal. Carbon, Ni and Cu are represented by the $C^-$ signal, $Ni^-$ signal and $Cu^-$ signal, respectively. Modified in [109]

Moreover, the measurements shown in Fig. 6.8 reveal no enhanced carbon intensity at the surface, which might indicate photoresist residuals. After direct RIBE investigations on RSA Al905 (section 4.2.2.1), a distinct maximum carbon intensity was detected directly at the surface and decreased with increasing depth within the surface layer. The carbon intensity shown in Fig. 6.8 after IBP is about one order of magnitude lower and hardly changes within the nitride layer. Therefore, the results reveal that no distinct photoresist residuals are detected on the surface. However, similar carbon implantation deeper within the surface layer during subsequent $O_2$ finishing experiments is observed.

Consequently, similar evolution of the local chemical surface composition is observed during $O_2$ finishing subsequently applied to ion beam planarization. The incorporation of carbon within the oxide surface layer seems to be a driving force for the reduced reflectivity after $O_2$ finishing in comparison to an untreated aluminium surface observed in Fig. 6.9, since the roughness features in the microroughness regime are strongly reduced during processing and SIMS depth profiling investigations additionally reveal an increased carbon signal within the oxide layer (Fig. 6.8).

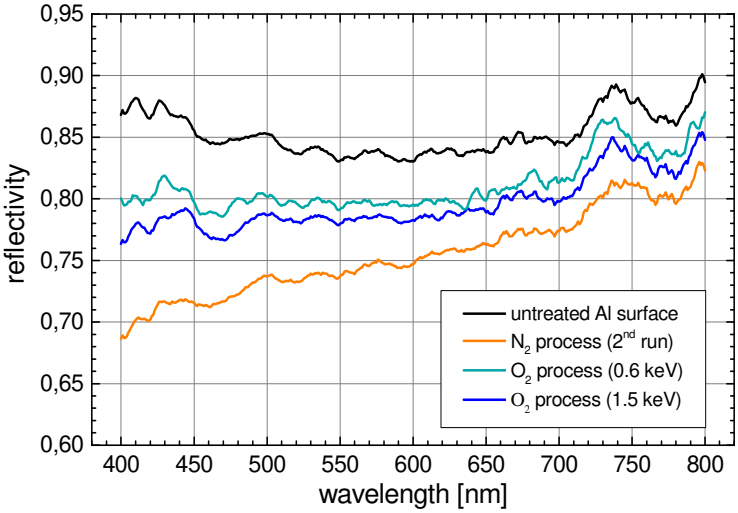


Fig. 6.9: Reflectivity in the visible spectral range of an untreated RSA Al905 surface, after two runs ion beam planarization with $N_2$ and after subsequent $O_2$ finishing at beam energies of 0.6 keV and 1.5 keV, respectively [109]

## 6.3.2 RIBE $O_2$ smoothing of RSA Al6061

The same $O_2$ finishing process routine after two runs ion beam planarization was also applied on RSA Al6061.However, the experiments are conducted at 1 keV and 1.5 keV, respectively.

The AFM measurements depicted in Fig. 6.10a represent the initial surface, after two runs ion beam planarization and after a subsequent oxygen process. The roughness evolution divided into microroughness and waviness/roughness is summarized in detail in Table 6.5. Note, that the turning marks are already <1 nm in height after the second IBP run (section 6.2.2) and thus also not measurable in the subsequent $O_2$ ion treatment steps. Hence, the turning mark height is not given in Table 6.5.

Table 6.5: Surface roughness values of aluminium Al6061before machining, after two runs ion beam planarization and subsequent $O_2$ finishing at 1 keV and 1.5 keV, respectively. The roughness values are divided into waviness/roughness, microroughness and the full range roughness

| RSA Al6061 | Microroughness [nm rms] | Roughness + waviness [nm rms] | Full range [nm rms] |
|---|---|---|---|
| Untreated | 1.3 ± 0.6 | 4.7 ± 0.8 | 4.9 ± 0.9 |
| $N_2$ planarization (2nd run) | 2.5 ± 0.3 | 3.2 ± 0.6 | 4.0 ± 0.7 |
| $O_2$ process (1 keV) | 1.3 ± 0.1 | 3.3 ± 0.6 | 3.5 ± 0.6 |
| $O_2$ process (1.5 keV) | 1.4 ± 0.2 | 3.3 ± 0.5 | 3.6 ± 0.6 |

After subsequent $O_2$ RIBE machining at 1 keV and 1.5 keV beam energy, the RMS roughness in the waviness/roughness regime remains almost unchanged. In contrast, the formation of etch pits is increased with sizes up to several hundred nanometers. They seem to preferentially form at the grain boundaries and along the turning marks of the RSA Al6061 material. This observation is equal to the recently reported work [34], where a series of ordered etch pits is formed after 400 nm material removal with oxygen process gas. Due to the low machining depth in these experiments, the etch pit formation is comparably sparse. The etch pit density is assumed to be enhanced with increasing processing time, due to coagulation of neighboring etch pits and the formation of new pits resulting from statistically distributed precipitates within the aluminium matrix.

In contrast, the PSD spectrum is remarkably decreased in the spatial frequency range above 3 $\mu m^{-1}$ to maximum 2 dec. Above 10 $\mu m^{-1}$ the PSD curve is even below the initial surface roughness (see Fig. 6.10b). As a consequence, the RMS roughness in the microroughness regime is remarkably decreased after $O_2$ finishing at 1 keV and 1.5 keV beam energy to (1.3 ±0.1) nm and (1.4 ±0.2) nm rms, respectively. The granular structure is removed after subsequent oxygen machining, but single particles in the sub-micrometer range are still apparent. In summary, the full range roughness decreases to (3.5 ± 0.6) nm rms and (3.6 ± 0.6) nm rms, respectively.

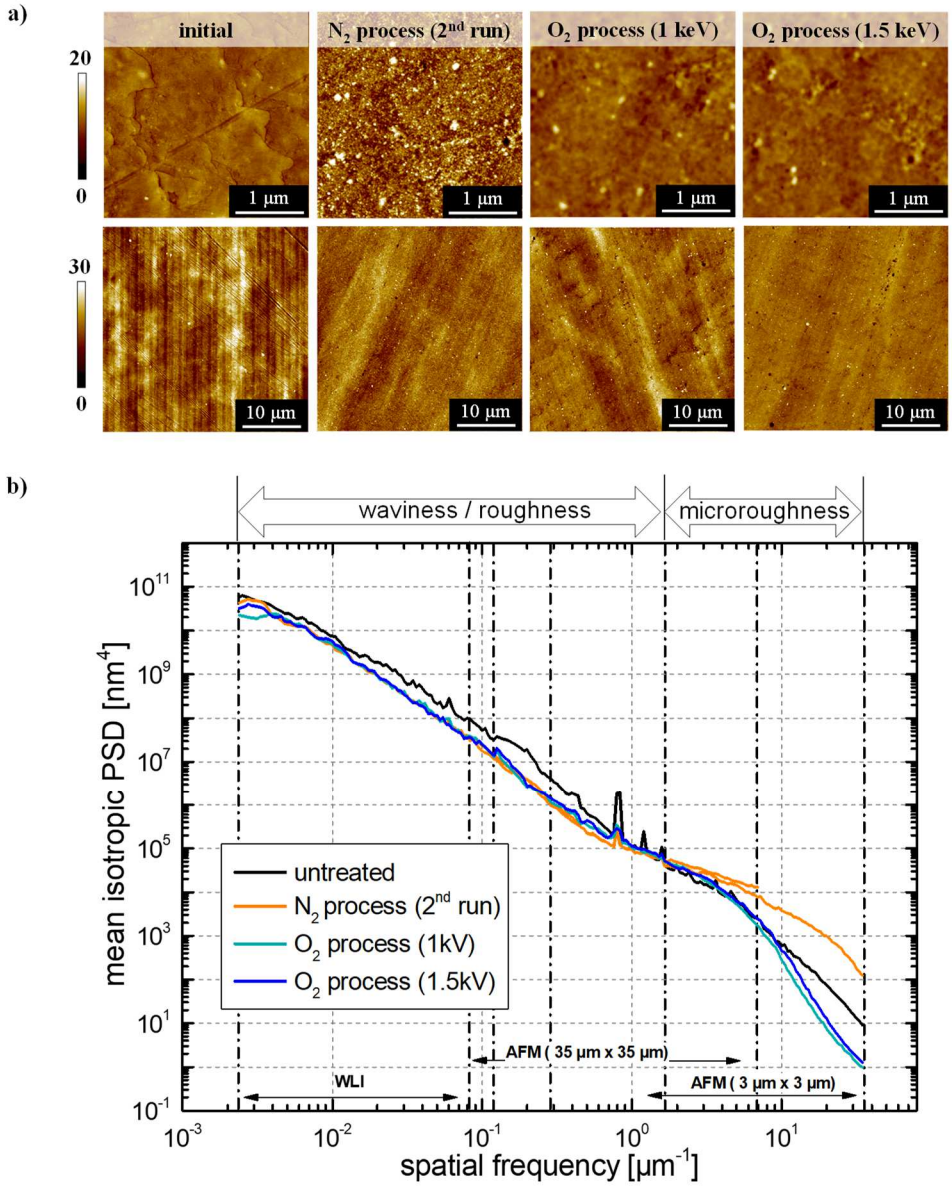


Fig. 6.10 a) AFM measurements of the RSA Al6061 (3 µm x 3 µm and 35 µm x 35 µm) initial surface, after the second planarization run and after oxygen finishing process at 1 keV and 1.5 keV, respectively. The z-scale is in nm. The corresponding PSD functions are shown in b). Modified in [107]

The local composition distribution after oxygen finishing at 1.5 keV beam voltage was monitored by SEM-EDX mapping (see Fig. 6.11). Similar observations were made during direct aluminium machining investigations with $N_2$ after 300 nm material removal (compare to Fig. 4.2). Mg and Si fractions are found to accumulate together within the etch pits after ion beam planarization and subsequent oxygen processing [34,63,112]. Indeed, the formation of etch pits after nitrogen processing of the sample depicted in Fig. 6.5 is comparably low, despite the strikingly decreased material removal during machining. The particles formed on the surface are mainly due to Si, Cr, Cu and partially Fe.

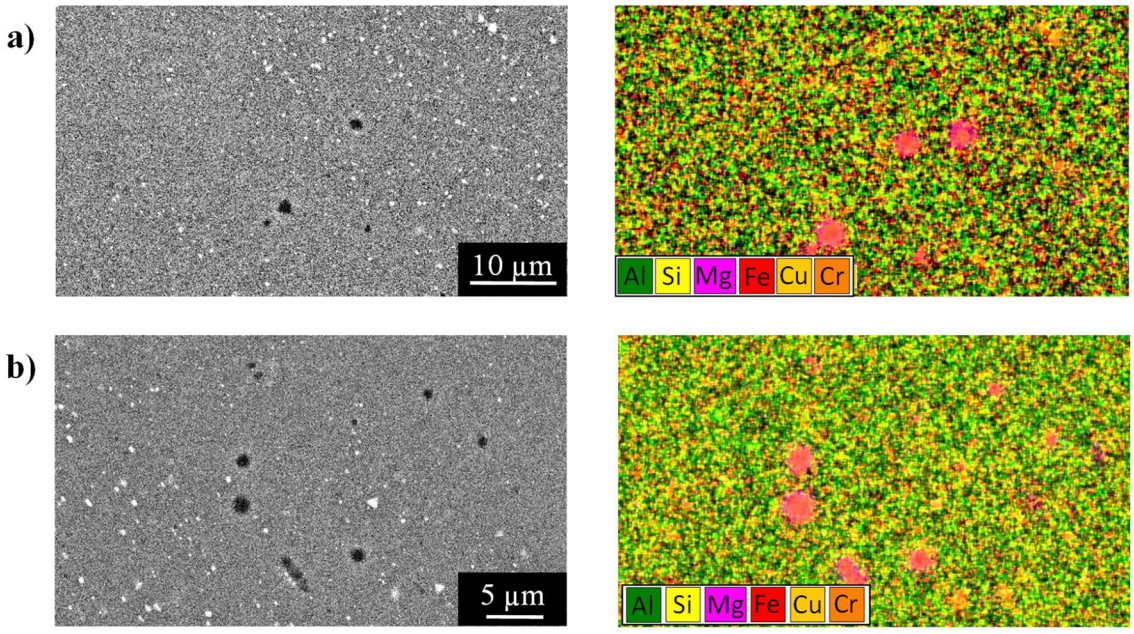


Fig. 6.11: a) SEM and SEM-EDX analysis of RSA Al6061 after two runs ion beam planarization and b) after subsequent oxygen machining at 1.5 keV beam energy revealing significant Mg and Si precipitations within the etch pits and particle formation due to Si, Cr and Fe. No distinct difference in local composition distribution is observed before and after RIBE machining with oxygen [107]

During two $N_2$ planarization runs, the reflectivity is decreased over the whole measured wavelength range of 400 – 800 nm (see Fig. 6.12).

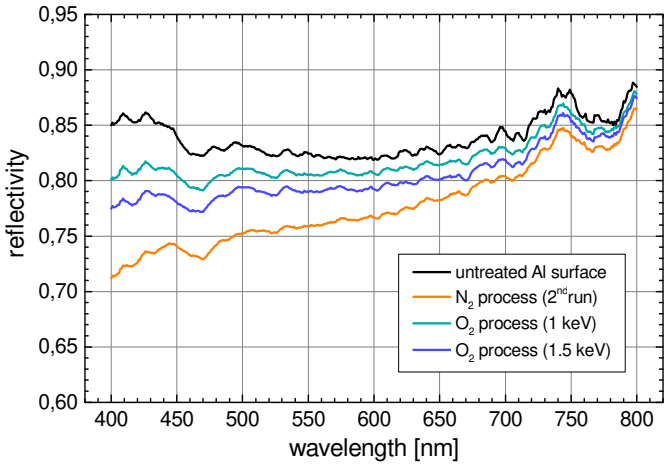


Fig. 6.12: Reflectivity in the visible spectral range of an untreated RSA Al6061 surface, after two runs ion beam planarization with $N_2$ and after subsequent $O_2$ finishing at beam energies of 1 keV and 1.5 keV, respectively

After subsequent $O_2$ finishing, irrespective of the ion beam energy used, the reflectivity increases over the whole wavelength range, but no longer reaches the value of an untreated aluminium surface. Same observations are made during $O_2$ finishing of the RSA Al905 sample

(see Fig. 6.9). Similar surface oxidation process is observed in ToF-SIMS measurements (not shown here) during ion beam smoothing of RSA Al6061 as already observed in section 6.3.1. Additionally, no enhanced carbon intensity at the surface was found which might indicate photoresist residuals. Consequently, comparable results are determined during $O_2$ RIBE finishing of Al6061.

## 6.4 Conclusions

Ion beam finishing of aluminium RSA Al6061 and RSA Al905 surfaces is based upon a two-step process including ion beam planarization with the aid of a sacrificial layer using nitrogen and subsequently applied aluminium machining with oxygen. The postbaking of ma-N 2405 photoresist used as sacrificial layer, is necessary to evaporate the majority of organic solvent, therefore increases the thermal stability and etch resistance to realize steady-state conditions during ion beam planarization. When applied on single-point diamond turned RSA Al905, the periodical structures regain appearance. Due to the shrinkage of the thin layer, the turning structure is transferred into the thin layer.

However, the surface roughness of technical aluminium RSA Al905 is decreased in the spatial frequency range of approximately 0.024 $\mu m^{-1}$ to 2 $\mu m^{-1}$ after two planarization runs and the turning mark height is successfully reduced by 82 %. The turning marks of RSA Al6061 are similarly strongly reduced in height to values in the sub-nanometer range indicating comparable improvement. The surface roughness is decreased in the spatial frequency range of 0.01 $\mu m^{-1}$ to 1.6 $\mu m^{-1}$. In direct comparison, RSA Al905 shows lower etch pit formation with sizes in the sub-micrometer range during machining, resulting in an optimized roughness preservation. Due to Si and Mg precipitates within RSA Al6061, the etch pit formation is increased.

In contrast, the surface roughness in the microroughness regime increases during ion beam planarization with nitrogen. The microroughness is increased during the first ion beam planarization run and is kept steady-state during the second planarization run. The precipitate structures within the aluminium base material and the formation of an about 14 - 15 nm thick nitride surface layer may be a key contribution for the increase in microroughness during nitrogen machining.

Indeed, an effective enhancement of the surface roughness in the microroughness regime and the reflectivity is observed during subsequently applied $O_2$ finishing. The surface errors situated

in the microroughness regime are drastically reduced to values of the initial aluminium surface and even smoother, while preserving the improved RMS roughness in the waviness/roughness regime as a consequence of $N_2$ planarization. Therefore, an overall reduction in the full range roughness is enabled. For both aluminium alloys RSA Al905 and RSA Al6061, the native oxide layer is enlarged during $O_2$ RIBE machining to about 14 - 18 nm thickness. The reflectivity is improved to values as already observed in chapter 4.2.2. Ion beam irradiation at reduced ion energy as 0.6 keV or 1 keV result in similar microroughness reduction, but an enhanced reflectivity for both aluminium alloys. RSA Al905 exhibits less etch pit formation with smaller pit sizes than RSA Al6061 during RIBE machining, which is suggested to result from the different precipitate composition. The particles observed after $N_2$ planarization of RSA Al905 resulting from Cu and Ni precipitates are drastically reduced during subsequent $O_2$ machining. In contrast, minor formation of etch pits on RSA Al6061 is observed during $N_2$ planarization and $O_2$ processing. In addition to the RIBE-based surface figuring technique, that preserves the initial roughness during machining [34], this promising two-step technology enables the smoothing of high-spatial frequency errors of single-point diamond turned aluminium alloys while preserving or even improving the initial microroughness.

# 7 Process transfer to a Kaufman-type broad beam ion source

The ion beam investigations described in the latter chapters 4-6 are additionally transferred to an ion beam plant ISA200 (NTG Neue Technologien GmbH) employing a Kaufman-type (filament-based discharge) broad beam source. With regard to ion beam planarization and direct smoothing technologies, the use of broad-beam ion sources with appropriate beam dimensions are a time-efficient and consequently cost-efficient alternative to a scanning ion beam [181]. The ion beam plant is equipped with a three-axis motion system. The base pressure is $2 \times 10^{-5}$ Pa and the working pressure with a mass flow of 4 standard cubic centimeters per minute (sccm) $O_2$ is $5 \times 10^{-3}$ Pa. Additionally, the sample was mounted on a rotating water-cooled (15 °C) sample holder. The RIBE investigations discussed in section 7.1 and 7.2 were performed at normal ion beam incidence angle.

## 7.1 RIBE machining investigations on RSA Al905

Reactive ion beam etching investigations with $N_2$ and $O_2$ were performed within a defined machining area on a RSA Al905 sample with material removal depths of 260 nm for $N_2$ processing and 160 nm for $O_2$ processing, respectively. Fig. 7.1 shows the roughness evolution of the RSA Al905 sample during irradiation with $N_2$ and $O_2$.

During $N_2$ RIBE machining, the full range roughness is enhanced to (8.4 ± 1.5) nm compared to (6.5 ± 1.7) nm before $N_2$ processing. The PSD functions shown in Fig. 7.1 reveal no change in the spatial frequency range below 0.45 $\mu m^{-1}$. However, the PSD function in the spatial frequency range of 0.45 $\mu m^{-1}$ – 34.7 $\mu m^{-1}$ is increased up to maximum 1 dec resulting in an enhanced microroughness of (4.2 ± 0.6) nm rms (see Fig. 7.1b and Table 7.1). Comparable calculated roughness values during $N_2$ RIBE machining were observed in chapter 4.1.2. Additionally, the increased PSD function up to 1 dec was also observed during ion beam planarization with $N_2$. However, during ion beam planarization and $N_2$ RIBE machining, the PSD spectrum is increased in the spatial frequency range above 1.6 $\mu m^{-1}$ and 2.5 $\mu m^{-1}$, respectively, corresponding to the formation of surface error features up to 625 nm and 400 nm, respectively. During RIBE investigations shown in Fig. 7.1, larger particles are formed due to

granules which seem to accumulate together but also a series of larger particles in the micrometer range without any granule structure.

The local composition distribution was monitored by SEM-EDX measurements (see Fig. 7.2). Significant Cu and Ni fractions, but also Mo, Fe, Mg and Si are found irregularly distributed over the aluminium surface. Consequently, the formation of etch pits with sizes in the sub-micrometer range up to 2 µm might be promoted by Mg and Si precipitates [34,63,112].

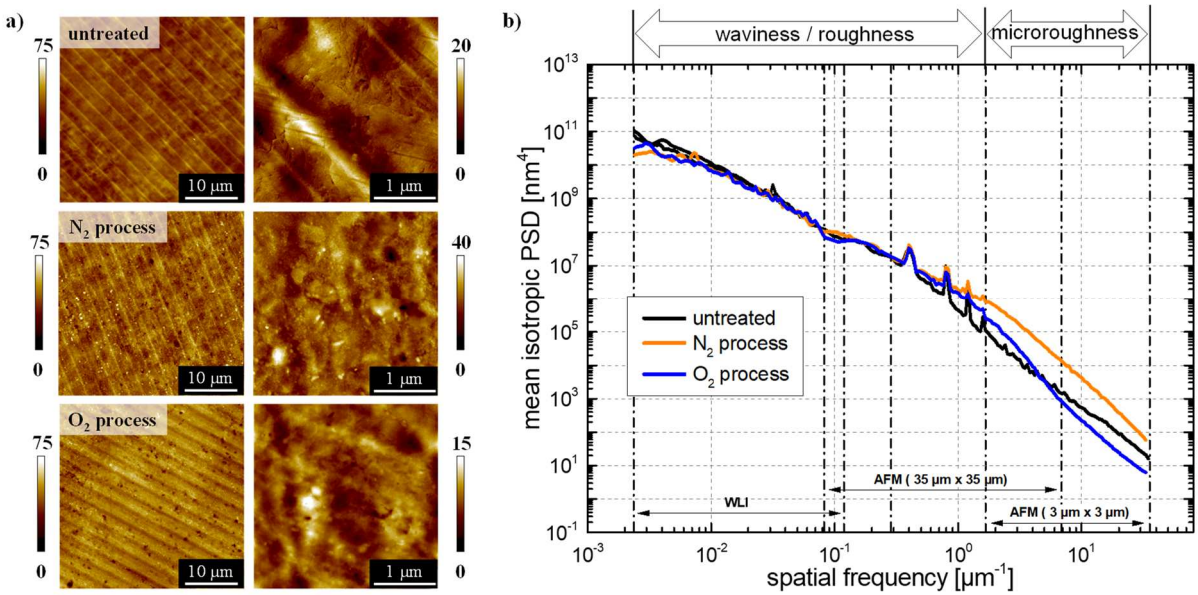


Fig. 7.1: a) AFM measurements of the untreated RSA Al905 surface (top) and after $N_2$ (middle) and $O_2$ (bottom) RIBE machining. The material removal depth is about 260 nm for $N_2$ processing and 160 nm for $O_2$ processing. The corresponding PSD functions are illustrated in b). Please note the different height scales in nm for the individual images in order to clarify the topography characteristics

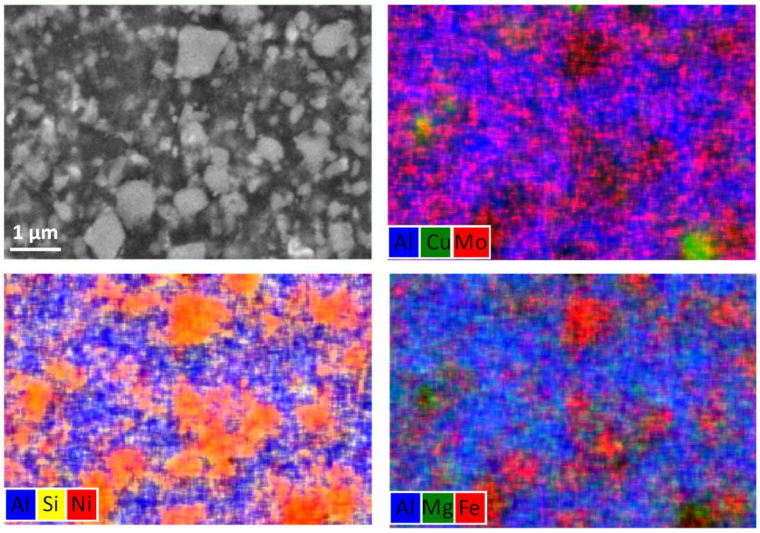


Fig. 7.2: SEM and SEM-EDX mapping image of an aluminium RSA Al905 alloy after $N_2$ processing using an ion beam plant ISA200 employing a Kaufman-type broad beam source

Consequently, deviations within the composition of RSA materials might have a considerable impact on the formation of pits and particles during processing.

Table 7.1: Surface roughness values of aluminium RSA Al905 divided into microroughness, waviness/roughness, and the full range roughness

| RSA Al905 | Microroughness [nm rms] | Roughness + waviness [nm rms] | Full range [nm rms] |
|---|---|---|---|
| Untreated | 1.3 ± 0.3 | 6.4 ± 1.5 | 6.5 ± 1.7 |
| $N_2$ process | 4.2 ± 0.6 | 7.3 ± 1.5 | 8.4 ± 1.5 |
| $O_2$ process | 1.6 ± 0.3 | 6.8 ± 1.2 | 7.0 ± 1.2 |

In contrast, $O_2$ RIBE machining reveals similar aluminium roughness evolution, independent on the ion source and plant used. In particular, the PSD function in the spatial frequency range of 0.45 $\mu m^{-1}$ – 5 $\mu m^{-1}$ is increased due to the formation of etch pits with diameter up to a few micrometer distributed over the whole surface (see Fig. 7.1). Hence, the roughness in the waviness/roughness regime is slightly increased to (6.8 ± 1.2) nm. Additionally, the PSD function is decreased in the spatial frequency range above 5 $\mu m^{-1}$, which is attributed to the gradient-dependent erosion process discussed in section 4.2 (see Fig. 7.1b). Since $O_2$ machining experiments performed with the TCP-type ion source and Kaufman-type ion source are conducted on the same aluminium disc sample but at different positions, a direct comparison of both investigations is shown in Fig. 7.3. The material removal depth after ion beam irradiation using the TCP-type ion source is about 250 nm, which might cause the slightly enhanced PSD function. However, similar surface degradation due to the formation of etch pits is observed and similar results are achievable.

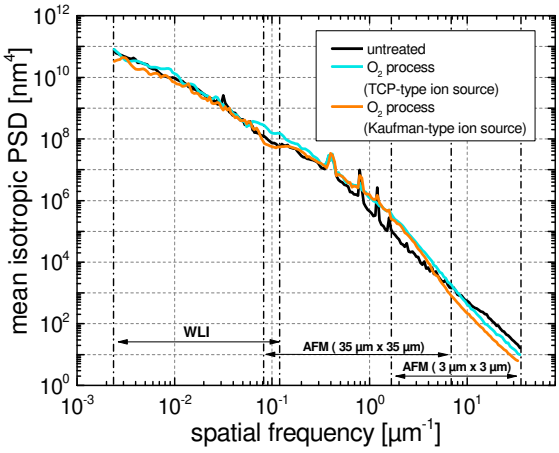


Fig. 7.3: PSD function of an untreated RSA Al905 surface and after $O_2$ ion beam irradiation using a TCP ion source and a Kaufman-type ion source

In summary, the investigations on RIBE machining using a broad beam Kaufman-type ion source conform to the results using a TCP-type ion source. Similar roughness evolution is observed using $N_2$ and $O_2$ gases. The microroughness is increased during RIBE machining with $N_2$ due to the formation of a granular structure, particles and etch pits. Additionally, etch pit formation is observed for both operating gases, resulting from the precipitate structure within the alloy.

## 7.2 Ion beam planarization of RSA Al6061

Ion beam planarization investigations with the aid of a sacrificial layer were performed on a RSA Al6061 disc sample shown in Fig. 7.4. In preliminary experiments performed on ma-N 2405 spin coated silicon wafers, the etch rate of the photoresist layer and the roughness evolution during machining were determined prior to ion beam planarization. The etch rate of ma-N 2405 is in the range of about 8 - 9 nm/min and of RSA Al6061 about 5 nm/min. The resulting selectivity of approximately 0.6 is similar to the investigations discussed in section 6.2.1. The applied ma-N 2405 planarization layer had a thickness of about 520 nm.

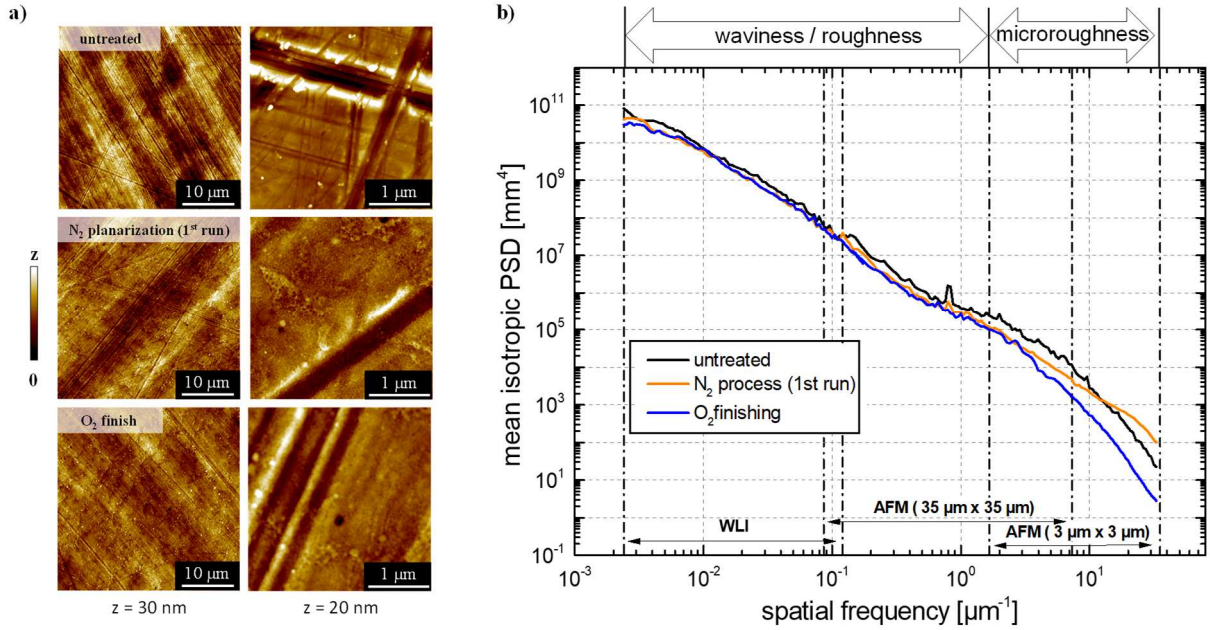


Fig. 7.4: a) AFM measurements of the untreated RSA Al6061 surface (top), after the first planarization run (middle) and after the subsequent oxygen process (bottom). The corresponding PSD functions are shown in b)

Table 7.2: Surface roughness values of aluminium RSA Al6061 divided into waviness/roughness and microroughness, respectively, and the full range roughness

| RSA Al6061 | Microroughness [nm rms] | Roughness + waviness [nm rms] | Full range [nm rms] |
|---|---|---|---|
| untreated | 3.0 ± 1.4 | 5.0 ± 1.0 | 5.9 ± 0.9 |
| $N_2$ planarization | 2.2 ± 0.6 | 4.0 ± 1.0 | 4.5 ± 1.1 |
| $O_2$ process | 1.5 ± 0.5 | 3.7 ± 0.9 | 4.0 ± 1.2 |

The 1.25 µm spaced turning marks, corresponding to the peak in the PSD function at a spatial frequency of 0.8 $\mu m^{-1}$, are distinctly reduced during ion beam planarization with $N_2$ gas. The PSD function is decreased in the spatial frequency range of 0.12 $\mu m^{-1}$ – 12.5 $\mu m^{-1}$ resulting in a decreased full range roughness of (4.5 ± 1.1) nm. Above 12.5 $\mu m^{-1}$ the PSD function is increased in maximum to about 0.5 dec due to the formation of granules distributed over the whole surface. Fig. 7.4 indicates, that the granular structure formed during ion beam planarization is reduced during subsequently applied $O_2$ finishing, resulting in the strong decreased PSD function above 3 $\mu m^{-1}$ and a RMS roughness of (1.5 ±0.5) nm. As a result of the two-step smoothing procedure, the full range roughness is decreased to (4.0 ±1.2) nm.

However, small scratches were irregularly distributed over the whole surface of the untreated sample. After the ion beam smoothing procedure, deeper scratches are still apparent on the surface, while scratches with smaller depth are removed. These scratches could indicate a possible pre-polishing process. In addition, the cleaning process of the aluminium optics within the IOM needs also to be examined in detail. Cleaning is carried out with isopropanol using an optical cloth. Excessive pressure or impurities on the surface could also result in superficial scratches. The samples are usually measured after cleaning.

The results indicate, that ion beam planarization and subsequently applied $O_2$ smoothing can be performed on different types of ion sources and can be deployed on facilities used on an industrial scale. The processing time of ion beam planarization with the aid of a sacrificial layer is remarkably reduced by about 50 % with the broad-beam Kaufman-type ion source.

## 7.3 Ion beam incidence angle dependent sputtering

In addition to RIBE investigations at normal ion beam incidence, the dependence of RSA Al905 surface roughness evolution on different ion beam incidence angles is analyzed.

So far, the RIBE investigations in this work were performed at normal ion beam incidence. However, with view to the next steps for further improvement of RIBE process control,

machining under inclined ion incidence may be of considerable interest. To give a first estimate of the possible future potential, the dependence of RSA Al905 surface roughness evolution on different ion beam incidence angles is analyzed. The basis are the experiments carried out in section 4.2.1 to determine the incidence angle sputter yields and oxide thicknesses (Fig. 4.7c, Fig. 4.8, and Fig. 4.9b). During low-energy ion beam incidence angle dependent irradiation with oxygen, the sample was rotating with 8 $min^{-1}$ positioned under the specific angle to the ion source for 80 minutes.

The surface topography evolution as a function of the varying sputter yield $Y(\Theta)$, dependent on the (local) ion incidence angle is a well-known phenomenon leading to surface smoothing, roughening or preferred spatial structuring with beneficial application consequences. Beside the erosion of solid surfaces during ion beam irradiation with energetic ions, numerous changes in surface topography evolution were observed [104,55,57,181-184]. A number of different approaches can be found in literature, for instance the formation of microscopic conical protrusion by Stewart and Thompson [182], or Nobes et al. [104], the phenomenon of the formation of periodic nanoscale patterns during sputtering of amorphous or crystalline materials under specific process conditions [181,183-188] and surface smoothing mechanism [55,57]. However, roughening can also be contributed by contaminations, grain boundaries or orientation dependent sputtering in polycrystalline materials and preferential sputtering of precipitates within alloys [57].

Thus, the aim of this chapter is a discussion of surface roughness evolution of RSA Al905 alloys during ion incidence dependent erosion. The surface error topography is analyzed in detail during ion beam irradiation with $O_2$ at different ion beam incidence angles. The initial aluminium surface is characterized by 2.5 µm spaced turning marks corresponding to the PSD deviation at 0.4 $\mu m^{-1}$ (see Fig. 7.5a). The spatial frequency range, where the turning marks are situated, is illustrated enlarged by means of an inset in Fig. 7.5a. The material removal depths and corresponding material removal rates are summarized in Table 7.3.

During ion beam irradiation with $O_2$ at normal incidence, the PSD function is increased in the spatial frequency range of about 0.45 $\mu m^{-1}$ – 4.8 $\mu m^{-1}$, which seems to correspond to the formation of etch pits. SEM-EDX measurements reveal significant Cu, Mo, Ni, Si, Fe and Mn fractions irregularly distributed over the whole surface. During machining with off-normal ion incidence angle, no distinct change of the turning mark structure can be observed. However, in

the spatial frequency range, where the turning marks are situated, the corresponding peaks seem to be partially decreased. However, this effect is assumed to result from superimposition of an enhanced etch pit formation resulting in an increased background in the PSD spectrum.

Table 7.3: Etch depth and corresponding material removal rates of ion beam machining investigations for the purpose of comparison of increasing ion beam incidence angle with almost retained ion beam processing parameter is presented. The max slope angle results from gradient distribution analysis in Fig. 7.6

| Incidence angle of ion beam [°] | Process gas | Etch depth [nm] | Material removal rate [nm/min] | Microroughness [nm rms] |
|---|---|---|---|---|
| 0 | $O_2$ | 144 | 1.8 | 1.6 ± 0.3 |
| 20 | $O_2$ | 176 | 2.2 | 1.7 ± 0.3 |
| 40 | $O_2$ | 250 | 3.1 | 2.5 ± 0.3 |
| 50 | $O_2$ | 266 | 3.3 | 2.6 ± 0.4 |
| 60 | $O_2$ | 291 | 3.6 | 2.9 ± 0.5 |
| 70 | $O_2$ | 235 | 2.9 | 2.1 ± 0.3 |

With increasing ion beam incidence angle of 20°, the PSD function is marginally increased in the spatial frequency range of 0.45 $\mu m^{-1}$ – 8.7 $\mu m^{-1}$. This may be attributed to the reduced etch pit formation compared to normal ion incidence (see Fig. 7.5b). Additionally, the material removal depths of RIBE investigations at normal ion incidence and at 20° are quite similar (Table 7.3). Exceptionally strong etch pit formation is observed during ion beam irradiation at 40°. The material removal depth of 250 nm is larger in comparison to the RIBE investigations at normal ion incidence angle. However, ion beam irradiation investigations with $O_2$ at normal ion incidence shown in Fig. 7.3 and presented in [34] reveal less distinct etch pit formation up to 400 nm. However, the alloy composition of RSA Al905 material can vary considerable for different production batches. The influence of preferential sputter erosion of the precipitates and the statistical distribution over the surface might be influencing factors. With further increasing ion incidence angle (>50°), the PSD deviations in the spatial frequency range, where the turning marks are situated, are gradually decreased.

Additionally, the etch pits are partially deformed when ion beam incidence angles of 20°, 40° and 50° are used. To some extent, a preferred deformation in direction of the incoming ion beam can be expected. However, since sample rotation is applied, the etch pit crater are irregularly deformed. Moreover, the formation of particles in the sub-micrometer range is observed after ion beam irradiation at incidence angles larger than 50°.

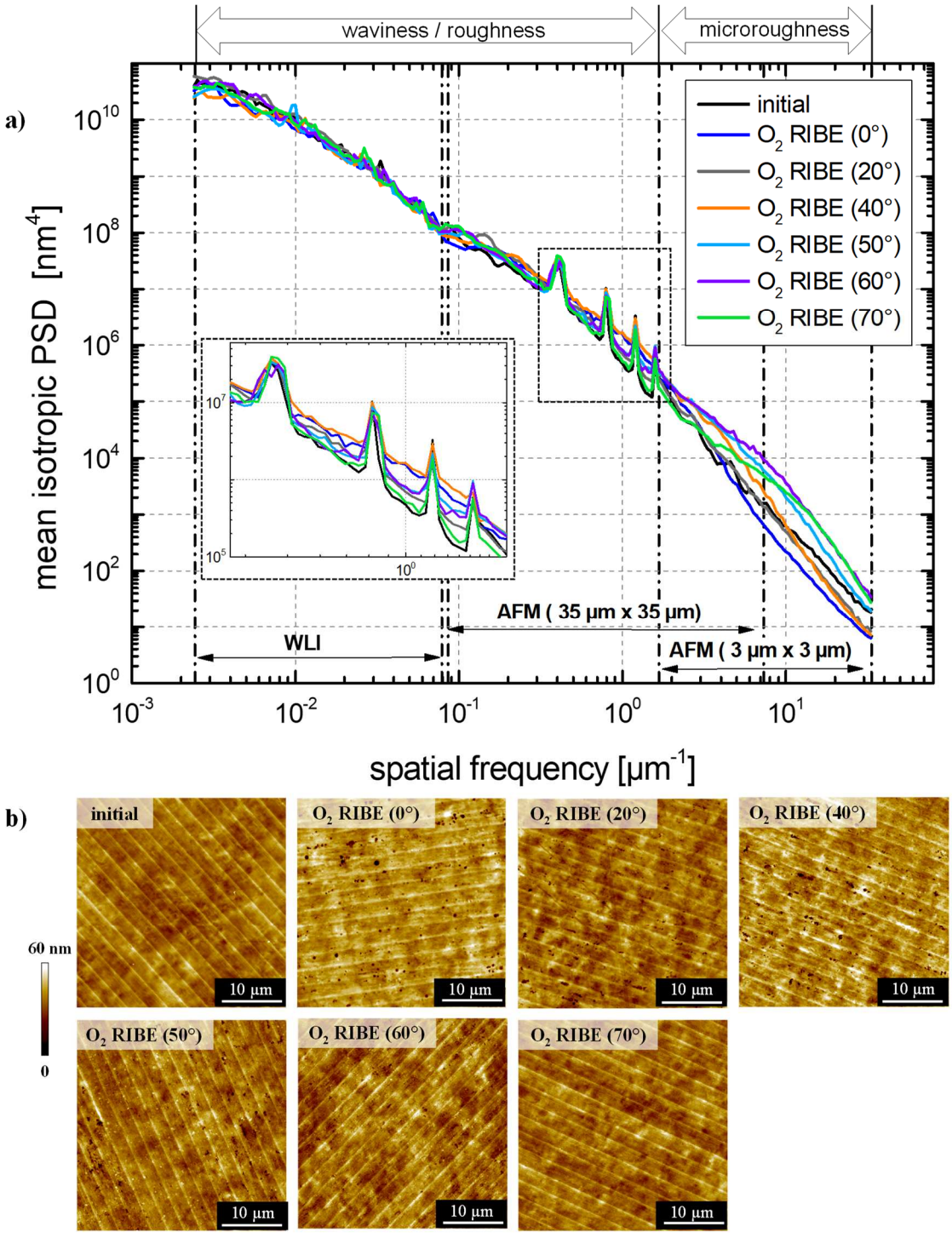


Fig. 7.5: Ion beam incidence angle dependent roughness evolution of RSA Al905 with a) corresponding PSD functions of the initial surface and after ion beam irradiation at 0° - 70°. The topography evolution is illustrated via AFM measurements in b)

TOF-SIMS depth profiling is performed, whereby no clear enrichment of specific alloying elements at the surface could be proven. Consequently, these bumps might be a result of self-organization during off-angle irradiation. The formation of etch pits is remarkably reduced at

ion incidence angles of ≥ 60°. The AFM measurements in Fig. 7.5b exhibit almost no etch pit formation after ion beam etching at 70° removing about 235 nm. Increasing ion beam incidence angles near glancing incidence might result in a smoothing of the surface [189-191].

However, with increasing angle of incidence, the PSD deviations are additionally shifted to higher spatial frequency regimes, i.e the microroughness increases with the incidence angle. During irradiation at 50° and 60°, the PSD functions nearly merge, except the distinct increase above 0.7 $\mu m^{-1}$ spatial frequency. Further increasing of the ion incidence angle to 70° results in preservation of the initial roughness in the spatial frequency range of 0.0024 $\mu m^{-1}$ - 2.9 $\mu m^{-1}$. However, a considerable increase in microroughness at > 2.9 $\mu m^{-1}$ is observed. For a more detailed analysis of surface error feature evolution in the microroughness regime during irradiation at different ion incidence angles, AFM measurements and corresponding gradient distributions are shown in Fig. 7.6.

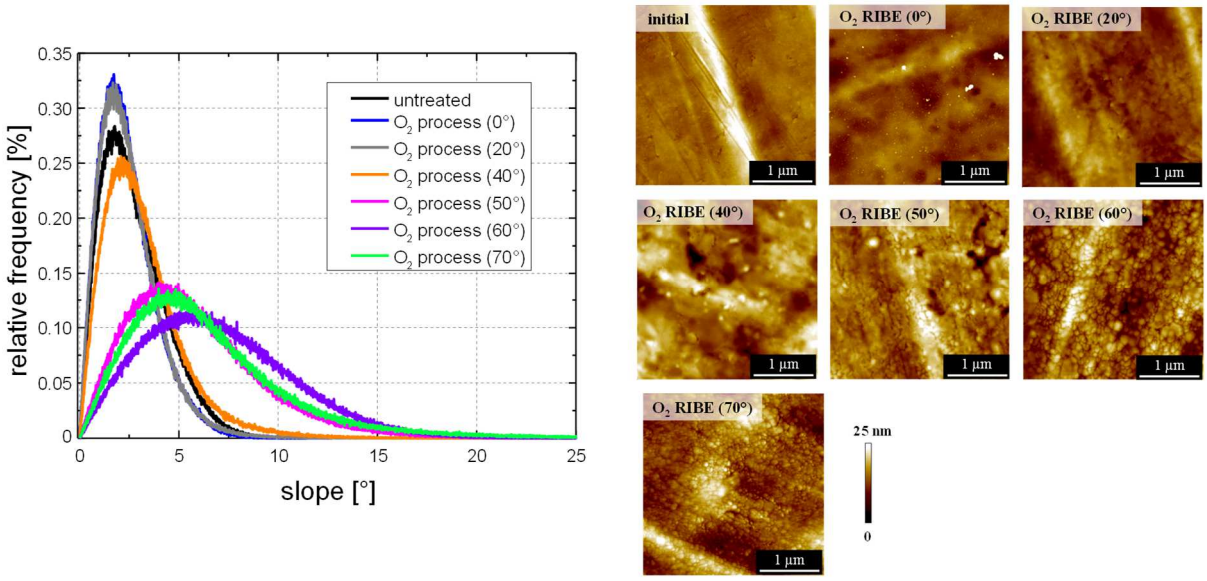


Fig. 7.6: Ion beam incidence angle dependent surface error evolution in the microroughness regime with corresponding AFM measurements

After irradiation at 20°, an incipient change of the surface structure can be detected. In particular, craters begin to form which are clearly visible after 40° irradiation. Moreover, nanometer-sized particles begin to form, corresponding to a slight broadening of the gradient distribution shown in Fig. 7.6. The development of these etch crater and particles is further intensified after ion beam irradiation at 50°. The effect of the formation of this surface structure intensifying with increasing ion incidence angle resulting in an enhanced microroughness might additionally be enhanced due to the gradually increasing etch depth up to 60°.

With increasing ion incidence angle the resulting microroughness increases gradually to (2.9 ± 0.5) nm after 60° ion irradiation (Table 7.3). Indeed, a correlation between increasing microroughness and the etch depth respective the removal rate might be suggested. According to the angle dependence in sputter yield (Fig. 4.9b) the etch depth changes in a distinct manner. The highest microroughness correlates with the highest material removal depth at 60°. However, with increasing ion incidence angle of 70°, the microroughness decreases again to (2.1 ± 0.3) nm corresponding to a decreased material removal depth (Table 7.3). In addition, the microroughness after 70° ion irradiation would compare to an ion incidence angle between 20° - 40°. However, as shown in Fig. 7.6, the surface topography after 70° ion irradiation and 20° - 40° considerably differ. The slope distribution maximum at 70° is about 4.5°, while it emerges to about 2° in the 20°-40° range. The reason is related to the microstructures formed, because at 20°-40° there are low-density particles of 30-100 nm size while particles with a size of 10 nm and below are obtained with a high-density at 70°. Hence, the microroughness formed under inclined $O_2$ ion irradiation is not suggested to be a sole etch depth effect.

The effect of self-organized surface topography evolution during low-energy ion beam irradiation is a well-known phenomenon traced back to a kinetic roughening of the surface. During irradiation, many atomistic processes and mechanisms become effective since the solid surface is far from equilibrium. Beside the material removal, resulting from atomic recoils and sputtered atoms, a pronounced surface topography evolution was often observed on different materials [181,192]. The formation of a random dot-like structure during ion beam irradiation at different incidence angles might also result from local ion incidence dependent sputtering. According to Frost et al. [193], initially rough polycrystalline $CuGaSe_2$ and $CuInS_2$ thin films are remarkably smoothed during $N_2$ IBE at ion incidence angles ≥ 70°. In general, the ion beam incidence angle needs to be adapted in such a way, that grains etch faster than the surrounding area resulting in a smoothing effect. Similar smoothing of surface errors situated in the microroughness regime of initially rough RSA Al905 surfaces at normal ion incidence was analyzed in detail in [108,130]. Further investigations on the ion incidence angle dependent surface structure formation in the microroughness regime after constant material removal depths would be of highly interest with regard to further investigations beyond the scope of this work.

Surface errors with local gradients up to about 65° are reduced during $O_2$ finishing at normal ion incidence removing 250 nm material resulting in local gradients below 15° [130]. The local

ion incidence dependent smoothing of rough surfaces was discussed in section 4.2.1. A contrary effect is observed during irradiation of initially smooth surfaces with low initial local gradients of maximum 11.4° (see Fig. 7.5a and Table 7.3). Distinct roughening due to the formation of surface errors in the microroughness regime with local gradients up to 68° is observed after $O_2$ irradiation at 70° incidence angle. Since a sample rotation is applied during machining, the surface structure shows no preferred orientation [51]. However, the roughness evolution is detrimental for smoothing applications of optical aluminium surfaces.

Promising results for ion beam figuring of optical aluminium surfaces are obtained during irradiation at 70° inclination. The erosion rate is enhanced to about 1.5 times (Fig. 4.9b and Table 7.3), compared to normal incidence, and the initial roughness is exceedingly well preserved in the spatial frequency range below 2.9 $\mu m^{-1}$. The current limitations to 400 nm removal depth due to beginning of surface degradation, caused by the formation of etch pits resulting from the inhomogeneous aluminium matrix, might be overcome. The result shown in Fig. 7.5 indicate almost no etch pit formation during machining at 70° and the 6 nm thick oxide passivation layer formed in-situ (see Fig. 4.7c in chapter 4.2.1) is beyond the near surface region of 1 nm, where sputtering originates. Further investigations are necessary to analyze, if the dot-like structure formed during machining at 70° incidence angle changes with increasing material removal depth. Additionally, these features might be reduced within a subsequently applied $O_2$ finishing at normal ion incidence.

## 7.4 Conclusions

RIBE-based machining of a RSA Al905 disc sample shows similar results of roughness evolution using a broad-beam Kaufman-type ion source. Additionally, ion beam planarization on RSA Al6061 with subsequently applied $O_2$ finishing lead to an improved full range roughness by about overall 32 % to (4.0 ±1.2) nm rms. Ion beam planarization investigations conducted on RSA Al6061 and RSA Al905, performed with a TCP-type ion source, resulted in an improved full range roughness of about 27 % and 41 %, respectively. Ion beam incidence angle dependent irradiation with sample rotation results in a reduced etch pit formation with increasing ion beam incidence angles of $\geq 60°$. After machining at 70°, almost no etch pit formation is observed. However, with increasing angle of incidence, the PSD deviations are additionally shifted to higher spatial frequency regimes resulting from the formation of a specific surface error structure in the microroughness regime. After irradiation at 40°, craters

and bumps are formed, which are further intensified after RIBE-investigations at 50°. Additionally, the formation of a dot-like structure distributed over the whole surface is observed, which intensifies with increasing ion beam incidence angles of 60° and 70°. These dots are assumed to result from local ion incidence dependent sputtering without preferred orientation, since the sample was rotated during irradiation.

# 8 Summary

RIBE investigations with the aim of smoothing optical aluminium surfaces reveal, that the combination of ion beam direct machining, ion beam planarization with the aid of a sacrificial layer and ion beam direct smoothing enable the improvement of surface roughness in a wide range of spatial frequencies.

Investigations on direct aluminium machining with $N_2$ gas at normal ion incidence enable an extension of the RIBE – based model scheme for ion beam figuring of optical aluminium surfaces [34] (chapter 4.1). The procedure is based upon the in-situ formation of a surface oxide or nitride layer, acting as passivation layer and inhibiting aluminium surface mobility and compositional homogeneities, thus preserving the initial surface topography during machining up to 1 µm machining depth. Moderate surface degradation is observed up to 2 µm machining depth [34,37]. In contrast to RIBE investigations of RSA Al6061, the full range roughness of RSA Al905 is exceedingly well preserved during $N_2$ machining (chapter 4.1). During machining of RSA Al6061, surface degradation s observed when 230 nm material was removed corresponding to significant PSD deviation in the spatial frequency range above 0.15 $\mu m^{-1}$. SEM-EDX measurements were performed and reveal particle formation resulting from significant Mg and Si fractions accumulate together within the etch pits. Reported in literature, $Mg_2Si$ precipitates are formed during the initial alloy annealing procedure [34,63,112] and are assumed to cause the observed etch pits.

RSA Al905 contains marginal Mg and Si precipitates within the aluminium base, but mainly Cu, Ni, Fe, Mn and Ti instead. Analyzing the local chemical surface composition prior to any ion beam irradiation procedure is of major importance, since various alloy compositions are known from literature [2,16] and preferential precipitate erosion strongly depends on the alloy composition and energetic ions used during irradiation [173-175,180,]. Consequently, the detailed study of roughness evolution during $N_2$ RIBE irradiation up to 2 µm machining depth was performed on RSA Al905 only. The turning marks with an initial height of about (23.1 ± 2.1) nm were gradually reduced during processing. However, after 1 µm material removal, increased surface degradation due to enhanced etch pit formation is observed resulting

in an increased PSD function in the spatial frequency range, where the turning marks are situated (chapter 4.1.2).

However, independent on the alloy composition and machining depth, an increased PSD deviation in the microroughness regime is observed and related to the formation of nanoscopic granules. Once this structure has been formed, it remains almost unchanged up to 2 µm material removal. These roughness features have a considerable impact on light scattering influencing the spectral reflection characteristics in the visible spectral range due to broad halo scattering [115,116]. Additionally, ToF-SIMS depth profiling reveal, that instantly during the first 50 nm material removal, a nitride layer is formed. For all machining depths from 50 nm - 2000 nm, the nitride has a nearly-constant thickness of about (14.7 ± 0.9) nm (chapter 4.1.2).

In order to improve the reflectivity and to reduce the nanoscopic surface errors formed during $N_2$ RIBE investigations, an $O_2$ RIBE direct smoothing procedure was subsequently applied (chapter 4.2.2).

The description of the surface topographical evolution under ion bombardment in direction of the sample normal is given by the local erosion velocity $v(\theta)$ related to the ion incidence angle dependent sputter yield $Y_{Al}(\theta)$ as a function of the local surface slope according to Carter et al. [52-55] (chapter 4.2.1). Based on the experimental and the simulation results, following model view is suggested for the effect of surface roughness evolution in RIBE processing of RSA Al905 surfaces with oxygen ions at normal ion incidence: Smooth surfaces exhibit an about 13 nm thick surface oxide layer during processing, which passivates structural and compositional inhomogeneities of the alloy matrix. Hence, the initial topography is preserved during machining. With increasing surface roughness more pronounced slopes become apparent on the surface resulting in locally different incidence angles of the incoming ions. Due to the angle dependence of the sputter yield, sputter erosion increases with increasing angle of incidence reaching a maximum at about 60 deg. Consequently, roughness features with high slope border areas are remarkably reduced since they show and enhanced erosion velocity resulting in a gradually reduction of these surface roughness features [52-56,130]. Similar observations for ion beam smoothing of various materials (e.g. III-V semiconductors (InAs, InP, InSb), Si or fused silica) has been reported in literature [57,131].

During $O_2$ ion irradiation, a surface oxidation process has to be considered (chapter 4.2.2). The nitride layer initially formed during $N_2$ RIBE machining is continuously eroded during $O_2$ RIBE

and displaced with oxygen. Similar results were obtained for two different ion beam energies of 0.6 keV and 1.5 keV. The surface errors formed during $N_2$ machining are drastically reduced to RMS-values of an untreated aluminium surface. Additionally, the process only affects errors situated in the microroughness regime since the PSD spectra are decreased in the spatial frequency range above $2\,\mu m^{-1}$ and $7.3\,\mu m^{-1}$ during irradiation at 1.5 keV and 0.6 keV, respectively. Below these spatial frequencies, all PSD spectra merge. Multiple repetitions, defining a specific material removal depth, were applied and reveal different results for both ion energies applied. During 1.5 keV irradiation, the RMS-roughness in the microroughness regime is strongly reduced, independent on the removal depth. However, after 120 nm material removal, slightly increased etch pit formation is observed, adversely affecting the reflectivity. The oxide layer is enlarged during processing to about 16 nm, independent on the material removal depth, whereby the nitride layer is continuously eroded with increasing material removal and displaced by oxygen. A comparison of both beam energies with comparable machining depth reveal a reduced oxide layer formation during $O_2$ RIBE machining with 0.6 keV beam energy of about 10 – 12 nm, since the penetration depth of oxygen within the nitride layer formed during $N_2$ RIBE is reduced when 0.6 keV was applied. Indeed, the surface errors situated in the microroughness regime were decreased similarly, independent on the material removal depth. The reflectivity during 0.6 keV $O_2$ irradiation was improved during the oxygen finishing process reaching nearly values of an untreated surface. However, carbon incorporation is observed within the formed oxide layer, which might cause the reduced reflectivity after oxygen finishing for both applied ion energies [137-139]. However, when 0.6 keV beam energies was used, the reflectivity is slightly further improved compared to 1.5 keV beam energy. Reflectivity measurements performed on the surfaces irradiated with $O_2$ at 1.5 keV were repeated after about one year storing the sample in air. As a result, slightly improvement of the reflectivity is observed on the surfaces subsequently irradiated with $O_2$. In contrast, surfaces irradiated with nitrogen, show a distinct improvement after storage, which might be caused by a modification of the top surface layer due to reactions with oxygen.

Though, the situation changes, when the aluminium surface is irradiated with $O_2$ ions at off-normal ion incidence angles (chapter 7.3). The oxide thickness is reduced with increasing ion incidence angle to 6.0 nm at 70 deg compared to 13 nm at normal ion incidence (chapter 4.2). Indeed, the oxide thickness is larger than the near surface region of 1 nm, where sputtering originates. Thus, the formation of sufficient thick surface oxide even in strongly inclined

surface areas is suggested. Consequently, the roughness preservation also holds for increasing ion incidence angles according to the in-situ formation of an oxide passivation layer. However, the roughness evolution strongly depends on the ion incidence angles.

RIBE-based investigations discussed in section 7.3, reveal distinctly reduced formation of etch pits at ion incidence angles of $\geq 60°$. Though, a specific surface structure situated in the microroughness regime is observed during irradiation at $\geq 40°$, which intensifies with increasing ion incidence angle. The local ion incidence dependent smoothing of rough surfaces as discussed in section 4.2.1, is based on an increased erosion velocity on roughness features with high slope border areas [107,130,193]. On initially smooth surfaces with low initial local border areas, a contrary effect can be observed. The evolution of a self-organized surface structure is assumed to result from kinetic roughening of the surface since the solid surface is far from equilibrium during irradiation [181,192].

Based on the $O_2$ RIBE smoothing procedure for surface errors situated in the microroughness regime, a IBP two – step process is discussed in section 5 and 6. The process route consists of an ion beam planarization procedure with the aid of a sacrificial layer to smooth periodically surface errors situated in the high-spatial frequency range resulting from SPDT and a subsequently applied $O_2$ finishing step to regain the initial microroughness and the optical quality of the surface. For ion beam planarization of optical aluminium surfaces RSA Al6061 and RSA Al905, the negative tone photoresist ma-N 2405 was chosen. Five different commercially available photoresists were tested, including positive and negative working photoresist materials (chapter 5.1). However, the negative tone photoresist ma-N 2405 shows a low etch rate and roughness preservation during $N_2$ RIBE processing contrary to the other materials tested. The selection of a negative photoresist as planarizing layer has several merits. The resist film can conveniently be applied by industrial standard techniques like spin coating or spray coating, the thickness is controllable by spin speed and dilution, and the crosslinking of the negative working photoresist during exposure to DUV light reduces the photosensitivity significantly [66,146,147]. Consequently, the IBP process development investigations were carried out with the negative tone resist. The photoresist ma-N 2405 is composed of a novolak as polymeric matrix, the biazide as PAC and an organic solvent consisting of anisole and cyclopentanone [147,148]. During DUV exposure, the PAC releases nitrogen and the resulting reactive nitrenes initiate the crosslinking of the compound (chapter 5.2.1). The organic solvent is essential to depress the viscosity of the solution to realize the spray or spin coating onto work-

pieces [148]. However, solvent molecules can act as plasticizers, lowering the glass transition temperature and thermal flow temperature of the resist film [160]. The subsequently applied postbaking is optimized to prevent bubbling and increase the thermal stability and etch resistance [147]. The postbaking temperature of 150 °C was found to be optimal, since remaining organic solvent is removed without initiating degradation of the polymer network [147,163] (chapter 5.2.3). This result is of major importance, since the degradation mechanism can also be expected to appear during ion beam treatments, if the heat dissipation is not sufficient. For ion beam planarization, irradiation at 1.2 keV with $N_2$ gas is chosen. On the one hand, the roughness of aluminium and photoresist layer are mainly preserved during $N_2$ RIBE machining. Additionally, the etch rates of both materials increase with increasing ion energy, reaching a plateau at about 1 keV. The resulting selectivity is about 0.6 for RSA Al6061 and RSA Al905 (chapter 5.4). When removing nearly the whole photoresist layer by ion beam irradiation with $N_2$ at 1.2 keV, steady-state material removal rates and roughness preservation during ion beam irradiation was achieved (chapter 5.5).

However, preliminary experiments were conducted on smooth silicon wafer. When the photoresist was applied to the aluminium surface, the turning marks became more apparent during postbaking, according to a shrinkage of the thin layer during heating (chapter 6.1). Since for ideal IBP process conditions the selectivity should be 1, iterative processing of two subsequent IBP steps is successfully applied to overcome the limitations of reduced planarization quality. These iteratively ion beam planarization experiments on both optical aluminium alloys RSA Al6061 and RSA Al905 at normal ion incidence angle reveal similar reduction of the turning marks (chapter 6.2). However, superimposed oscillations resulting from SPDT situated in the mid-spatial frequency range of 0.0024 $\mu m^{-1}$ - 0.007 $\mu m^{-1}$ were not fully embedded by the thin photoresist layer. Consequently, a distinct improvement of these surface errors was barely to be expected. Though, the turning marks situated in the high spatial frequency range are successfully reduced by overall 82 % after two planarization runs. In contrast, the turning marks present on the initial RSA Al6061 surface were only a few nanometers in depth. Consequently, these structures are almost completely removed during processing. In consideration of the different surface qualities of the aluminium samples used for ion beam planarization investigations, comparable results are obtained. However, similar surface roughness increase is observed in the microroughness regime after $N_2$ irradiation as

discussed in section 4.1. For applications in the VIS and UV spectral range, a further reduction of the increased microroughness and an improvement of the reflectivity is prerequisite.

Thus, the direct $O_2$ finishing process was applied in both samples (chapter 6.3). The nitride layers formed during planarization reveal thicknesses of about 15.3 nm on RSA Al905 and 16.6 nm on RSA Al6061, respectively, which is similar to the investigations without the use of a planarization layer. During subsequently $O_2$ irradiation, the RMS roughness in the microroughness regime is reduced to values comparable with the untreated surface and even smoother, while preserving the improved rms roughness in the waviness/roughness regime from $N_2$ planarization. Therefore, an overall reduction in the full range roughness is enabled. The nitride layer is continuously replaced by an oxide formed on both RSA Al6061 and RSA Al905. Apparently, there are deviations within the composition of RSA Al6061 and RSA Al905. After the first run ion beam planarization, significant Cu and Ni precipitates are observed irregularly distributed over the whole RSA Al905 surface. This observation is assumed to result from preferential sputter erosion of aluminium within the alloy [171-174]. However, during $O_2$ RIBE investigations at 1.5 keV, preferential erosion of Ni and Cu is observed and analyzed by ToF-SIMS depth profiling and SEM-EDX measurements. Within the altered top layer, the sputtering behavior of oxides seems rather more complex than on pure metals, especially within an alloy [173-180]. On RSA Al6061, local chemical composition monitored by SEM-EDX measurements reveal similar observations after $N_2$ planarization and $O_2$ finishing. The formation of etch pits according to Mg and Si precipitates is observed after $N_2$ planarization and is slightly enhanced during subsequently applied $O_2$ finishing. Additionally, the reflectivity is improved on both alloys to comparable values as already observed in chapter 4.2.2. However, ion beam irradiation at lower beam energies of 0.6 keV and 1 keV result in similar microroughness reduction, but an enhanced reflectivity for both aluminium alloys, in direct comparison to investigations with 1.5 keV. The thickness of the oxide layer is less pronounced when 0.6 keV beam energy are used, but the nitride layer is also drastically reduced (chapter 6.3).

Additionally, the discussed RIBE investigations were also performed using a Kaufman-type broad beam ion source (chapter 7). The use of a broad-beam ion source is a time-efficient and consequently cost-efficient alternative to the scanning ion beam machining, since the processing time is remarkably reduced by overall 50 % during ion beam planarization with the aid of a sacrificial layer (chapter 7.2). However, for complex shaped or strongly curved

aluminium mirror devices the deterministic machining conception with a fine-beam ion source is mandatory. During ion beam machining of a RSA Al905 surface with $O_2$ conform results are obtained using both ion source types (chapter 7.1). However, during $N_2$ irradiation using the Kaufman-type ion source, the PSD function is increased in the spatial frequency range of 0.45 $\mu m^{-1}$ – 34.7 $\mu m^{-1}$, resulting from the formation of nanoscopic granules and exceptionally pronounced etch pit formation. Similar increased surface degradation after $N_2$ machining of a RSA Al905 sample is likewise observed (chapter 4.2.2.2). Possible causes discussed in chapter 4.2.2.2 might be the different initial surface qualities of the samples used for the investigations. The possible worn cutting tool used during SPDT could result in an eroded, larger edge radius less prone to cutting and therefore creating more plastic flow [62,110]. The consequential smeared top surface layer results in reduced roughness, but the underlying surface quality is revealed during ion beam irradiation. However, for RIBE investigations discussed in section 7.1, $O_2$ and $N_2$ RIBE machining was performed on the same sample but at different positions. During $O_2$ RIBE investigations, no enhanced surface degradation was observed. Additionally, two independently used aluminum samples have shown this roughness evolution during machining with the TCP-type ion source and the Kaufman-type ion source used. Consequently, the enhanced surface degradation resulting from increased etch pit formation might also result from changing amounts of precipitate fractions within the alloy. The formation of etch pits might result from small amounts of Mg and Si within the inhomogeneous matrix structure. Once the etch pits are formed, further increasing material removal depth leads to an enlargement of the lateral pit size due to coagulation of neighboring pits and isotropic etching contributions [34]. Additionally, new etch pits will be formed resulting from the statistically distribution within the aluminium alloy matrix. Consequently, the observed enhanced surface degradation might result from a progressively declining degradation during ion beam machining process. Nevertheless, during one $N_2$ ion beam planarization run with the aid of a sacrificial layer and subsequently applied $O_2$ finishing, the initial full range roughness of the about (5.9 ± 0.9) nm of the RSA Al6061 surface is reduced to (4.0 ± 1.2) nm using the Kaufman-type ion source (chapter 7.2). Independent on the ion source used, similar improvement is observed during the two-step smoothing procedure.

Furthermore, promising results for ion beam figuring of optical aluminium surfaces were obtained during irradiation at 70° inclination with substrate rotation (chapter 7.3). The current limitation to 400 nm material removal depth with $O_2$, due to the beginning surface degradation

caused by the formation of etch pits resulting from the inhomogeneous aluminium matrix, might be overcome. The erosion rate is enhanced to about 1.5 times in comparison to normal incidence, and the initial roughness is exceedingly well preserved in the spatial frequency range below 2.9 $\mu m^{-1}$. The ion incidence angle is beyond the maximum of about 60° and already within a range, where it decreases again since the probability of recoil generation is decreased [45,127,128]. However, nearly no etch pit formation is observed during machining at 70° and the approximately 6 nm thick oxide passivation layer formed in-situ (see Fig. 4.7c in chapter 4.2.1) is beyond the near surface region of 1 nm, where sputtering originates. Additionally, further investigations are necessary to analyze, if the dot-like structure formed during machining at 70° incidence angle changes with increasing material removal depth. Additionally, these features might be reduced within a subsequently applied $O_2$ finishing at normal incidence.

# 9 Conclusions and Outlook

The applicability of ion beam technologies on the finishing of aluminium mirror devices is considered. It was demonstrated, that low-energy ion bombardment (≤ 1.5 keV) of single-point diamond turned aluminium mirrors is well suitable for surface error correction in a wide range of spatial frequencies. By use of a reactive process control with non-toxic gases as oxygen and nitrogen a considerable improvement could be verified in different fields of surface correction:

**Figure error correction**

A decisive factor for the process design is the particular control of surface roughness in the depth removal range of several 100 nanometers. This is particular challenging for technological optical materials as aluminium alloys. In this context it was shown, that reactively driven ion beam irradiation results in the formation of a passivation layer, inhibiting aluminium surface mobility and compositional inhomogeneity. The in-situ formation of a nitride layer with steady-state thickness exceedingly-well preserves the initial surface topography during machining up to 1 µm depth. A systematic experimental study of the surface roughness evolution of optical aluminium surfaces RSA Al6061 and RSA Al905 during ion beam irradiation with $N_2$ and $O_2$ is presented. Investigations by white light interferometry and atomic force microscopy and the data evaluation considering the specific PSD functions have shown, that surface degradation during $N_2$ RIBE is mainly caused by the formation of etch pits and small particles as well as granules with sizes in the nanometer range. In this context, a particular interest is given to the inhomogeneous precipitate structure within the aluminium alloy matrix, since particles and pits with sizes in the micrometer and sub-micrometer range formed during irradiation is mainly caused by the statistically distributed fractions of the alloy composition. By means of SEM-EDX and ToF-SIMS depth profiling, the main influence of the alloy composition on roughness evolution is discussed. The granular structure formed during $N_2$ machining was observed on both aluminium alloys. Consequently, a two-step process route was examined throughout the study, subsequently applying an $O_2$ RIBE finishing process to reduce these roughness features. Therefore, the reflective properties regain the characteristic of the untreated optical surface and an increased chemical long-term stability is achieved. Thus, the examined two-step process route enables an extension of the RIBE-based model scheme for ion beam figuring of optical aluminium surfaces.

**Smoothing of the turning mark structures via ion beam planarization with the aid of a sacrificial layer**

Waviness and roughness features resulting from SPDT have a considerable impact on light scattering and adversely affect the spectral reflection characteristics in the visible spectral range. A particular interest is given to the reduction of periodical structures distributed over the whole surface. The main work deals with the influence of different process parameter on the surface roughness evolution in the high- to mid-spatial frequency range. A detailed analysis has been performed by means of topography measurements and local chemical composition analysis.

As a remarkable result of iterative ion beam planarization operation, the periodical turning marks resulting from SPDT are drastically reduced by overall 82 % of both RSA Al6061 and RSA Al905. However, an enhanced etch pit formation was observed after the second run. On the sacrificial layer applied for ion beam planarization investigations a granular structure during $N_2$ machining similar to the observations on aluminium are found. Once nitrogen is used as processing gas for ion beam irradiation, the nanoscopic granular structure is formed on the surface and results in a decreased reflectivity. Hence, a similar nitride layer formation was observed during $N_2$ RIBE-based planarization with the aid of a sacrificial layer. However, the initial surface roughness in the microroughness regime is restored or even reduced when the same two-step process route is applied with subsequently $O_2$ finishing process.

A comparative study on ion beam machining by a TCP-type and a Kaufman-type ion source revealed, that similar process results can be obtained with different, technologically important types of ion beam sources. These investigations show that reactive ion beam etching can be applied in general within the established ion beam machining equipment and is thus very suitable for surface error correction of single-point diamond turned optical aluminium surfaces. Contrary to figure error correction, the amount of material removal at the optical surface is rather low in the planarization process. Although, the aluminium alloy composition has a considerable impact on surface roughness evolution counteracting the planarization process result, those contributions are limited due to the low removal depth. Thus, a significant reduction of the turning marks can be achieved. A particular customization is possible by targeted adaptation of the process parameters.

**Microroughness improvement via ion beam direct smoothing**

Investigations on subsequently applied $O_2$ finishing procedure have shown, that experimental investigations on reduction of surface errors situated in the microroughness regime agrees with the theoretical model of the local surface slope dependent surface smoothing. The reduction of these surface features in the high spatial frequency range strongly depends on the ion incidence angle and the initial gradient distribution of these surface features. It was shown, that normal ion incidence irradiation with $O_2$ results in a remarkable reduction of these surface features on initially rough surfaces. Applying the process route on aluminium surfaces after $N_2$ irradiation, the granular structure in the microroughness regime is removed. The nitride layer is gradually reduced and replaced with an oxygen-rich surface. As a consequence, the reflectivity is distinctly enhanced. Additionally, the role of the ion energy applied for $O_2$ processing is studied. This parameter is mainly important for the nitride layer removal and oxide replacement as well as microroughness improvement. The model only holds for the assumption that the ion beam incidence angle is adapted in such a way, that grains etch faster than the surrounding area resulting in a smoothing effect. Due to self-organization processes for the given off-normal erosion conditions, surface features with nanometer sizes are formed.

The results can be a starting point for continuative studies considering ion beam process optimization of optical aluminium surfaces.

In particular, the observed surface degradation of RSA Al6061 is mainly caused by etch pit formation of $Mg_2Si$ precipitates statistically distributed within the aluminium matrix. Consequently, ion beam machining investigations with $N_2$ and $O_2$ were limited to RSA Al905 only. It has not been studied, whether the enhanced erosion rates of these precipitates might be reduced when varying ion incidence angles are used. Additionally, ion beam machining was performed within a defined machining area limited by an aluminium mask. The influence of aluminium redeposition during machining was not investigated. Concerning a further optimization of the developed processes, further investigations on the formation of the nitride layer by the use of nitrogen are necessary. In particular, it has not been investigated at what time during the process the granular-structured layer is formed, since the entire measurements were performed ex-situ.

From a technological point of view, adjusting the sample to the ion source in such a way, that the ion beam incidence angle is continuously normal to the sample surface, is possible. The knowledge gained in the course of this work can in principle be used for RIBE-based machining of curved surfaces on the five-axis motion set-up described in section 3.1, adjusting the sample to the ion source under specific angles. Moreover, up to now, the RIBE-based machining procedures failed on optical aluminium surfaces after specific polishing or after use of the fly-cutting technology. Despite those surfaces are ultra-smooth their material matrix differs strongly from the bulk material, thus they degrade during ion beam irradiation. The analysis of the differed surface structure and the development of adapted ion beam process would be of technological interest.

Regarding the ion beam planarization technique with the aid of a sacrificial layer, further work has to be done to optimize the photoresist application. The used spin-coating within the present study might be limited due to the viscosity of the planarizing layer since the thickness of the layer has to be constant over the whole surface. To overcome these limitations, an optimized spray-coating application might represent one possible solution. With regard to an optimization of the process for further reduction of the surface roughness for short-wave applications, a closer look needs to be taken at the cleaning procedure of the aluminium disc samples before machining, since the creation of small scratches on the surface during cleaning with an optical cloth pose a danger. According to the process conditions used in ion beam planarization, a further improvement might be achieved with increasing iterative runs under inclined ion incidence conditions, where surface degradation and surface smoothing intersect. Known from literature [143,161,168], the use of fluorine-containing gases can optimize the selectivity between planarization layer and aluminium. Additionally, studies on ion beam processing using $N_2$ depending on the ion incidence angle are still unclear. This raises further questions regarding the optimization of ion beam planarization. From a technological point of view, operating with pure $CHF_3$ or $NF_3$ led to unstable process conditions. A supply of these gases within an adapted gas mixture together with $N_2$ as well as $O_2$ could increase the process stability and the selectivity. With view on a further improvement of the optical device characteristic the choice of materials used within the ion source may be reconsidered to reduce the impurity incorporation as carbon into the optical surface.

# Appendix

## A List of abbreviations

Table A.1: List of abbreviations

| | |
|---|---|
| AFM | Atomic Force Microscopy |
| ATR | Attenuated Total Reflection |
| CI | Chemical ionization |
| CMP | Chemical Mechanical Polishing |
| dec | decade |
| DSC | Differential Scanning Calorimetry |
| DTG | Derivative thermogram |
| DUV | Deep Ultraviolet |
| EDX | Energy-Dispersive X-ray |
| EI | Electron ionization |
| ESCA | Electron spectroscopy for chemical analysis |
| fcc | Face-centered cubic |
| FOV | Field of view |
| FT | Fourier-Transform |
| FWHM | Full-width at half maximum |
| GAATR | Grazing Angle Attenuated Total Reflection |
| GC | Gas Chromatography |
| HSF | High Spatial Frequency |
| IBF | Ion Beam Figuring |
| IBP | Ion Beam Planarization |
| IR | Infrared |
| IRE | Internal reflection element |
| LSF | Low Spatial Frequency |
| MIR | Mid-Infrared |
| MMD | Multiple magnification detector |
| MRF® | Magnetorheological Finishing |
| MS | Mass Specrometry |
| MSF | Mid Spatial Frequency |
| NiP | Nickel-Phosphorous |
| NIR | Near infrared |
| OMM | Optical metrology module |
| PAC | Photoactive Compound |

(Continued on the next page)

Prosecution of Table A.1

| | |
|---|---|
| PSD | Power Spectral Density |
| PSI | Phase shift interferometry |
| RF | Radio frequency |
| RIBE | Reactive Ion Beam Etching |
| RIE | Reactive ion etching |
| RMS | Root Mean Square |
| RSA | Rapidly Solidified Aluminum |
| RSP | Rapidly Solidification Process |
| sccm | Standard cubic centimeter |
| SEM | Scanning Electron Microscopy |
| SIMS | Secondary Ion Mass Spectrometry |
| SPDT | Single-Point Diamond Turning |
| SPM | Scanning probe microscopy |
| TCP | Transformed coupled plasma |
| TGA | Thermogravimetric Analysis |
| TMA | Three-Mirror-Anastigmat |
| ToF | Time of flight- |
| TRIM.SP | Transport of ions in matter for sputtering |
| UHV | Ultrahigh vacuum |
| UV | Ultraviolet |
| VIS | Visible |
| VSI | Vertical scanning interferometry |
| WLI | White Light Interferometry |
| XPS | X-ray Photoelectron Spectroscopy |

# B Selected properties of photoresist materials

**AZ 1505**

The positive tone photoresist AZ 1505 is one type of the AZ 1500 product series of MicroChemicals GmbH. The different types differ in the solvent concentration, the photo active compound content, and special reins for different applications. AZ 1505 is a commonly used resist mask for Cr etching in photomask production with resulting film thickness of about 400 – 700 nm, depending on the applied spin speed. About 580 nm are achieved at 3000 rpm during spin-coating for 30 seconds. It consists of a methoxy-propyl acetate (PGMEA) solvent, novolak as polymer matrix and a photoactive compound belonging to Diazo-Naphto-Quinon-sulfonates (DNQ) [68].

**ma-P 1205**

The positive tone photoresist ma-P 1205 is one type of the ma-P 1200 series of micro resist technology. The novolak-based photoresist also contains DNQ and represents a positive resist for conventional patterning processes used in dry and wet chemical etching as well as for electroplating processes. The resulting thickness of the photoresist layer is approximately 500 nm at 3000 rotations per minute [67].

**mr-PosEBR 0.3**

mr-PosEBR is an acrylic copolymer consisting of a chlorine-containing monomer and another monomer bearing aromatic side-groups. The positive tone photoresist material is developed for high resolution electron-beam lithography of micro resist technology. The approximated film thickness at 3000 rotations per minute is 300 nm [69].

**ma-N 405**

ma-N 400 series are mainly used as single layer resist for conventional pattern transfer. ma-N 405 is one ready-to-use solution of the series with a film thickness of about 500 nm at 3000 rotations per minute. ma-N 400 and ma-N 2400 series are negative photoresists for UV and e-beam lithography, pattern transfer process via physical vapor deposition and lift-off processes

of microresist technology. The ma-N 405 resist is based on aromatic biazide/novolak composition with a temperature stability during prebake limited to 110 °C maximum [67].

**ma-N 2405**

ma-N 2405 is one type of negative photoresist of the ma-N 2400 series by micro resist technology. The material is composed of a novolak matrix, biazide as crosslinking agent and anisole and cyclopentanone as organic solvent. The ma-N 2400 series is e-beam and deep UV sensitive mainly used for electron beam lithography. The viscosity of the resist is about (8 ± 1) mPas resulting in (500 ± 0.05) nm layer thickness after spin-coating at 3000 rpm for 30 seconds [71,147,150,151].

During DUV-exposure, the azide groups of the photoactive compound (R-$N_3$) release nitrogen and the resulting reactive nitrenes (R-N:) initiate the crosslinking of the resist. The organic solvent is not involved in the chemical reaction, but is essential to depress the viscosity of the solution to realize spray- or spin-coating [66,147,150,152]. The schematic reaction scheme is illustrated in Fig. B.1.

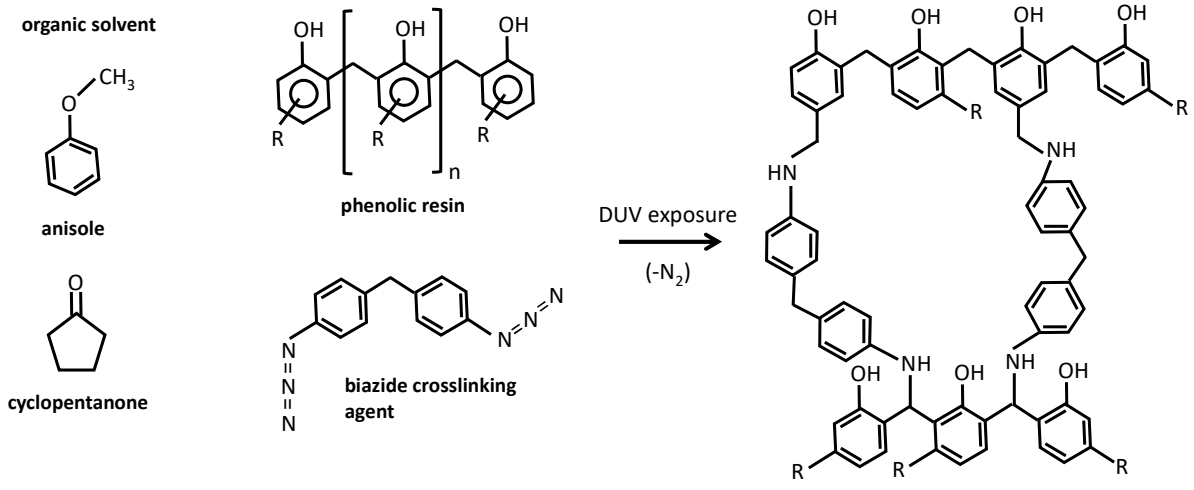


Fig. B.1: Schematic reaction scheme of the novolak-based ma-N 2405 negative tone photoresist

# References


1 Delplancke, F., Nijenhuis, J., de Man, H., Andolfato, L., Treichel, R., Hopman, J., Derie, F., *Proc. SPIE* **5491**, 81250T (2014)

2 Gubbels, G. P. H., van Venrooy, B. W. H., Bosch, A. J., Senden, R., *Proc. SPIE*, **7018**, 70183A (2008)

3 Steinkopf, R., Gebhardt, A., Scheiding, S., Rohde, M., Stenzel, O., Gliech, S., Giggel, V., Löscher, H., Ullrich, G., Rucks, P., Duparre, A., Risse, S., Eberhardt, R., Tünnermann, A., *Proc. SPIE,* **7102**, 71020C (2008)

4 Vukobratovich, D., Schaefer, J.P., *Proc. SPIE* **8125**, 81250T (2011)

5 Rozelot, J. P., Bingham, R., Walker, D. D., *ESO Conference on progress in telescope and instrumentation technologies* (ed. M.-H. Ulrich), Observatory, Garching, 71-74 (1992)

6 Yin, Z., Yi, Z., *Appl. Opt.* **54**, 7835-7841 (2015)

7 ter Horst, R., Tromp, N., de Haan, M., Navarro, R., Venema, L., Pragt. J., *Proc. SPIE* **10566**, 105660P (2017)

8 Kinast, J., Schlegel, R., Kleinbauer, K., Steinkopf, R., Follert, R., Dorn, R. J., Lizon, J. L., Hatzes, A., Tünnermann, A., *Proc. SPIE* **10706**, 107063G (2018)

9 Klocek, P. (ed.): Handbook of Infrared Optical Materials, CRC Press, New York (1991)

10 Zang, Z., Yan, J., Kuriyagawa, T., *Int. J. Extrem. Manuf.* **1**, 022001 (2019)

11 Gubbels, G. P. H., Venrooy, B. W. H., and Henselmans, R., *Proc. SPIE* **7426**, 742607 (2009)

12 Risse, S., Gebhardt, A. Damm, C., Peschel, T., Stöckl, W., Feigl, T., Kirschstein, S., Eberhardt, R., Kaiser, N., Tünnermann, A., *Proc. SPIE* **7010***,* 701016 (2008)

13 Zhang, J., Zhang, X., Tan, S., Xie, X., *Curr. Opt. Photon.* **1**, 364-371 (2017)

14 He, C. L., Zong, W. J., *Opt. Express* **27**, 1326-1344 (2019)

15 Supranowitz, C., Hall, C., Dumas, P., Hallock, B., *Proc. SPIE* **6545**, 65450S (2007)

16 ter Horst, R., de Haan, M., Gubbels, G., Senden, R., van Venrooy, B., Hoogstrate. A., *Proc. SPIE* **8450**, 84502M (2012)

17 ter Horst, R., Tromp, N., de Haan, M., Navarro, R., Venema, L., Pragt. J., *Proc. SPIE* **10566**, 105660P (2017)

18 Xu, H., Zhang, X., Xu, M., Li, X., *Proc SPIE* **8416**, 84161D (2012)

19 Revel, P., Khanfir, H., Fillit, R.-Y., *J. Mater. Process. Technol.* **178**, 154-161 (2006)

20 Khan, G. S., Sarepaka, R. G. V., Chattopadhyay, K. D., Jain, P. K., Bajpai, R. P., *IJEMS* **11**, 25-30 (2004)

21 Dogra, M., Sharma, V. S., Dureja, J. S., *J. Eng. Sci. Technol. Rev.* **4**, 1-13 (2011)

22 Beier, M., Scheiding, S., Gebhardt, A., Loose, R., Risse, S., Eberhardt, R., Tünnermann, A., *Proc. SPIE* **8884**, 88840S (2013)

23 Li, Y., Takino, H., Frost, F., *Opt. Express*, **25**, 7828-7838 (2017)

24 Li, Y., Takino, H., Frost, F., *JEOS:RP*, **13**, 27 (2017)

25 Li, Z. Z., Wang, J. M., Peng, X. Q., Ho, L. T., Yin, Z. Q., Li, S. Y., Cheung, C. F., *Appl. Opt.* **50**, 2458-2463 (2011)

26 Folkman, S. L., Stevens, M., *Proc. SPIE*, **4771**, 254–264 (2002)

27 Ahmad, E. A., Paquin, R.A.: Metal Mirrors, In: Ahmad, E. A. (ed.) Handbook of Optomechanical Engineering, pp. 89-110, CRC Press LLC, New York (1997)

28 Yin, Z., Yi, Z., *Appl. Opt.* **54**, 7835-7841 (2015)

29 Moeggenborg, K. J., Barros, C., Lesiak, S., Naguib, N., Reggie, S., *Proc. SPIE* **7060**, 706002 (2008)

30 Weiser, M., *Nucl. Instruments Methods Phys. Res. Sect. B Beam Interact. Mater. Atoms* **267**, 1390-1393 (2009)

31 Zhou, L., Idir, M., Bouet, N., Kaznatcheev, K., Huang, L., Vescovi, M., Dai. Y., Li, S.," *J. Synchrotron Radiat.* **23**, 182–186 (2016).

32 Zeuner, M., Kiontke, S. R., *Opt. Photonik* **7**, 56–58 (2012)

33 Egert, C. M., *Proc. SPIE* **1752**, 63-72 (1992)

34 Bauer, J., Frost, F.,Arnold, T., *J. Phys. D*, **50**, 85101 (2017)

35 Donnelly, V. M., Kornblit, A., *J. Vac. Sci. Technol.* A **31**, 050825 (2013)

36 Schaible, P. M., Metzger, W. C., Anderson, J. P., *J. Vac. Sci. Technol.* **15**, 334-337 (1978)

37 Bauer, J., Frost, F., Lehmann, A., Ulitschka, M., Li, Y., Arnold, T., *Opt. Eng* **58**, 092612 (2019)

38 Harsha, K. S. S. (ed.): Principles of Vapor Deposition of Thin Films, Elsevier Ltd, Oxford (2006)

39 Wehner, G. K., *Phys. Rev.* **102**, 690-719 (1956)

40 Wehner, G. K., *Adv. Electronics Electr. Phys.***7**, 239-298 (1955)

41 Sigmund, P.: Sputtering by ion bombardment theoretical concepts, In: Behrisch, R. (ed.) Sputtering by Particle Bombardment I: Physical Sputtering of Single-Element Solids, pp. 9–71, Springer-Verlag Berlin-Heidelberg (1981)

42 Sigmund, P., *Phys. Rev.* **184**, 383; *Phys. Rev.* **187**, 786 (1969)

43 Bohdansky, J., *J. Nucl. Instrum. Methods Phys. Res. B* **2**, 587-591 (1984)

44 Y. Yamamura, H. Tawara, *At. Data Nucl. Data Tables* **62**, 149–253 (1996)

45 Yamamura, Y., Itikawa, Y., Itoh, N., Institute of Physics, Nagoya University Report No IPPJ-AM-26 (1983)

46 Eckstein, W., Preuss, R., *J. Nucl. Mater.* **320**, 209-213 (2013)

47 Johnson, L. F., Ingersoll, K. A. and Kahng, D., *Appl. Phys. Lett.*, **40**, 636–638. (1982)

48 Johnson, L. F., Ingersoll, K. A., *Appl. Opt.*, **22**, 1165–1167 (1983)

49 Frost, F., Takino. H., Fechner, R., Schindler, A., Ohi, N., Numora, K. (2007), Towards Synthesis of Micro-/Nano-systems, Springer, London, 239-242 (2007)

50 Frost, F., Takino, H., Fechner, R., Schindler, A., Ohi, N., Nomura, K., *Jpn. J. Appl. Phys.* **46**, 6071-6073 (2007)

51 Frost, F., Fechner, R., Flamm, D., Ziberi, B., Franke, W., Schindler, A., *Appl. Phys. A* **78**, 651-654 (2004)

52 Nobes, M. J., Colligon, J. S., Carter, G., *J. Mater. Sci.* **4**, 730 – 733 (1969).

53 Carter, G., Colligon, J. S., and Nobes, M. J., *J. Mater. Sci.* **6**, 115–117 (1971).

54 Carter G., Nobes, M. J., Whitton, J. L., *J. Mater. Sci.* **13**, 2725-2728 (1978).

55 Carter, G., *J. Phys. D: Appl. Phys.* **34**, R1-R22 (2001).

56 Carter, G., Nobes, M. J., Katardjiev, I. V., *Phil. Mag. B* **66**, 419-425 (1992).

57 Frost, F., Fechner, R., Ziberi, B., Völlner, J., Flamm, D. and Schindler, A., *J. Phys. Condens. Matter* **21**, 224026 (2009).

58 Bauer, J., Ulitschka, M., Pietag, F., Arnold, T., *J. Astron. Telesc. Instrum. Syst.* **4**, 046003 (2018)

59 OWIS GmbH, Universal Position Control Unit PS 90 User Manual, 2017 https://www.owis.eu/fileadmin/user_upload/owis.eu/pages/05_Support/01_Handbuecher/PS_90_User_Manual.pdf

60 Zeuner, M., Meichsner, J., Neumann, H., Scholze, F., Bigl, F., *J. Appl. Phys.* **80**, 611-622 (1996)

61 Paquin, R. A.: Properties of Metals, In: Bass, M., van Stryland, E. W., Williams, D. R., Wolfe, W. I. (eds.) Handbook of Optics Volume II. Devices, Measurements, and Properties, pp. 35.1-35.78, McGraw-Hill, Inc., New York, (1995)

62 Jasinevicius, R. G., Duduch, J. G., Porto, A. J. V., Purquério, B. M., *J. Braz. Soc. Mech. Sci.* **21**, 628-644 (1999)

63 Askeland, D. R., Phulé, P. P. (eds.): The Science and Engineering of Materials, CA: Brooks/Cole-Thomson Learning, Pacific Groove (2003)

64 Wouters O., Vellinga W. P., van Tijum, R., de Hosson, J. Th. M., *Acta Materialia* **53**, 4043-4050 (2005)

65 Gubbels, G., Tegelaers, L., Senden, R., *Proc. SPIE* **8884**, 88841W (2013)

66 Steppan, H., Buhr, G., Vollmann, H., *Angew. Chem. Int. Ed.* **94**, 471–485 (2006)

67 Product Data Sheet ma-P 1200 series, https://www.microresist.de/sites/default/files/download/PI_map1200_2015_0.pdf

68 Product Data Sheet and Safety Data Sheet AZ 1500 series, https://www.microchemicals.com/micro/tds_az_1500_series.pdf

69 Pfirrmann, S., Kirchner, R., Lohse, O., Guzenko, V. A., Voigt, A., Harder, I., Kolander, A., Schift, H., Gruetzner, G., *Proc. SPIE* **9779**, 977925 (2016)

70 Product Data Sheet ma-N 400 series https://www.microresist.de/sites/default/files/download/PI_ma-N_400_1400_2015.pdf

71 Product Data Sheet ma-N 2400 series https://www.microresist.de/sites/default/files/download/PI_ma-N_2400_mr-EBL_6000_2015_0.pdf

72 Harvey, J. E., Thompson, A. K., *Proc. SPIE* **2576**, 155-174 (1995).

73 Bennett, J. M., *Meas. Sci. Technol.* **3**, 1119-1127 (1992).

74 DIN ISO 10110-8:2012-02, Optik und Photonik - Erstellung von Zeichnungen für optische Elemente und Systeme - Teil 8: Oberflächengüte; Rauheit und Welligkeit (ISO 10110-8:2010)

75 Mishra, V., Khatri, N., Nand, K., Singh, K., Sarepaka, R. G. V. (2015), *Mater. Manuf. Processes*, **30**, 232-240 (2015)

76 Bruker Corporations, "NPFlex and NPFlex-LA Optical Profiling System User Manual, (2011)

77 de Groot, P.: Phase Shifting Interferometry, In: Leach, R. (ed.), Optical Measurement of Surface Topography, pp. 167-186, Springer-Verlag Berlin Heidelberg (2011)

78 Sugawara, Y.: Atomic Force Microscopy, In: Morita, S.(ed.) Roadmap of Scanning Probe Microscopy, pp. 15-21, Springer-Verlag Berlin-Heidelberg (2007)

79 Eaton, P., West, P. (eds.): Atomic Force Microscopy, Oxford University Press Inc., New York (2010)

80 The Scanning Probe Image Processor SPIP™, Image Metrology, Denmark, https://www.imagemet.com/products/spip/

81 Duparré, A., Ferre-Borrull, J., Gliech, S., Notni, G., Steinert, J., Bennett J. M., *Appl. Opt.* **41** 154 (2002)

82 Jacobs, T. D. B., Junge, T., Pastewka, L., *Surf. Topogr.: Metrol. Prop.* **5**, 013001

83 Zhou, W., Apkarian, R. P., Wang, Z. L., Joy, D.: Fundamentals of scanning electron microscopy, In: Zhou, W., Wang, Z. L. (eds.) Scanning Microscopy for Nanotechnology: Techniques and Applications, pp. 1-40, Springer, New York (2006)

84 Newbury, D. E., Ritchie, N. W. M., *Scanning* **35**, 141–168 (2013)

85 Van der Heide, P., "X-ray photoelectron spectroscopy: An introduction to principles and practices", John Wiley & Sons, Hoboken, New Jersey (2011)

86 Moulder, J. F., Stickle, W. F., Sobol, P. E., Bomben, K. D.: Handbook of X-ray Photoelectron Spectroscopy. A reference book of standard spectra for identification and interpretation of XPS data, In: Chastain, J. (ed.), Physical Electronics Division, Perkin-Elmer Corporation, Minnesota (1992)

87 Unifit, Scientific Software GmbH, Germany, https://unifit-software.de

88 Schwarz, S. A., "Secondary Ion Mass Spectroscopy", In: Buschow, K. H. J., Flemings, M. C., Kramer, E. J., Veyssière, P., Cahn, R. W., Ilschner, B., Mahajan, S. (eds.) Encyclopedia of Materials: Science and Technology (2nd Edition), pp. 8283-8290, Elsevier, Oxford (2001)

89 Adriaens, A., van Vaeck, L., Adams, F., *Mass Spectrom. Rev.* **18**, 48–81 (1999)

90 Brown, A., Vickerman, J. C., *Surf. Interface Anal.* **6**, 1-14 (1984)

91 Vickerman, J. C.: SIMS, Time-of-flight, and Surface Analysis, Buschow, K. H. J., Flemings, M. C., Kramer, E. J., Veyssière, P., Cahn, R. W., Ilschner, B., Mahajan, S. (eds.) Encyclopedia of Materials: Science and Technology (2nd Edition), pp 8624-8628, Elsevier, Oxford (2001)

92 Ruedenauer, F. G.: Liquid Metal Ion Sources for Scanning SIMS, In: Benninghoven A., Okano J., Shimizu R., Werner H.W. (eds) Secondary Ion Mass Spectrometry SIMS IV. Springer Series in Chemical Physics, vol 36. Springer, Berlin, Heidelberg (1984)

93 Wittmaack, K., *Appl. Surf. Sci.***203-204**, 20-26 (2003)

94 Ismail, A. A., van de Voort, F. R., Sedman, J.: Fourier transform infrared spectroscopy: Principles and applications, In: Paré, J. R. J., Bélanger, J. M. R. (eds.) Techniques and Instrumentation in Analytical Chemistry, vol **18**, pp. 93-139, Elsevier, Amsterdam (1997)

95 Larkin, P. J. (ed.): Infrared and Raman Spectroscopy. Principles and spectral Interpretation, Elsevier, Amsterdam (2011)

96 Fringeli, U. P.: ATR and Reflectance IR spectroscopy, applications, In: Lindon, J. C. (ed.) Encyclopedia of spectroscopy and spectrometry, Academic press, London (2000)

97 Milosevic, M. (ed.): Internal Reflection and ATR Spectroscopy, John Wiley & Sons, Inc., Hoboken, New Jersey (2012)

98 Milosevic, M., Milosevic, V., Berets S. L., *Appl Spectrosc.* **61**, 530-536 (2007)

99 Maxwell Garnett, J. C., *Philos. Trans. R. Soc. London Ser. A* **203**, 385(1904); **205**, 237 (1906).

100 Ng, H. M., Saidi, N. M., Omar, F. S., Ramesh, K., Ramesh, S., Bashir, S.: Thermogravimetric Analysis of Polymers, In: Encyclopedia of Polymer Science and Technology, John Wiley & Sons, Inc. Hoboken, New Jersey (2018)

101 Bottom, R.: Thermogravimetric Analysis, In: Gabbott, P. (ed.) Principles and Applications of Thermal Analysis, pp. 87-118, Wiley, Hoboken, (2008)

102 Höhne, G. W. H., Hemminger, W. F., Flammersheim, H.-J.: Differential Scanning Calorimetry, Springer Verlag, Berlin Heidelberg (2004)

103 Brittain, H. G., Bruce, R. D.: Thermal analysis, In: Ahuja, S., Jespersen, N. (eds.) Comprehensive Analytical Chemistry volume 47. Modern Instrumental Analysis, pp. 63-109, Elsevier, Amsterdam (2006)

104 Hussain, S. Z., Maqbool, K., *Int. J. Curr. Sci.* **13**, E116-E126 (2014)

105 Vazquez-Roig, P., Pico, Y.: Gas chromatography and mass spectroscopy techniques for the detection of chemical contaminants and residues in foods, In: Schrenk, D. (ed.), Chemical Contaminants and Residues in Food, pp. 17-64, Woodhead Publishing, Cambridge (2012)

106 Kitson, F. G., Larsen, B. S., McEwen, C. N.: Gas Chromatography and Mass Spectrometry. A Practical Guide 1st edition, Academic Press, New York (1996)

107 Ulitschka, M., Bauer, J., Frost, F., Arnold, T., *J. Astron. Telesc. Instrum. Syst.* 6(1), 014001 (2020)

108 Ulitschka, M., Bauer, J., Dornberg, G., Frost, F., Arnold, T., *Opt. Eng.* 59(3), 035108 (2020)

109 Ulitschka, M., Bauer, J., Frost, F., Arnold, T., J. Eur. Opt. Soc.-Rapid Publ. (under review)

110 Thiele, J. D., Melkote, S. N., *J. Manuf. Process.* **2**, 270-276 (2000)

111 Khan, G. S., Sarepaka, R. G., Chattopadhyay, K. D., Jain, P. K. Narasimham, V. M. L., *Indian J. Eng. Mater. Sci.* **10**, 123-130 (2003)

112 Chakrabarti, D. J., Cheong, B. K., Laughlin, D. E., *Mater. Sci. Forum* **396-402**, 857-862 (2002)

113 Thedsakhulwong, A., Locharoenrat, K., Thowladda, W, *Adv. Mater. Res.* **631-632**, 186-191 (2013)

114 Visuttipitukul, P., Aizawa, T., *Surf. Eng*. **22**, 187-195 (2006)

115 Loughin, S., French, R. H.: Aluminium nitride (AlN), In: Palik, E. D. (ed.) Handbook of Optical Constants of Solids volume III, pp. 373-401, Academic Press, New York (1997)

116 Bennett, H. E., Porteus, J. O., *J. Opt. Soc. Am.* **51**, 123-129 (1961)

117 McCune, R. C., Donlon, W. T., Plummer Jr., H. K., Toth, L., Kunz, F. W., *Thin Solid Films* **168**, 263-280 (1989)

118 Sanghera, H. K., Sullivan, J. L., Saied, S. O. (1999), *Appl. Surf. Sci.* **141**, 57-76 (1999)

119 Möller, W., Parascandola, S., Telbizova, T., Günzel, R., Richter, E., *Surf. Coat. Tech.* **136**, 73-79 (2001)

120 Netterfield, R. P., Müller, K.-H., McKenzie, D. R., Goonan, M. J., Martin, P. J., *J. Appl. Phys.* **63**, 760-769 (1988)

121 Espinós, J. P., González-Elipe, A. R., Mohai, M., Bertóti, I., *Surf. Interface Anal.* **30**, 90-94 (2000)

122 Yang, M., Gatto, A., Kaiser, N., *Proc. SPIE* **5963**, 59630M (2005)

123 Eckstein, W. (ed.): Computer simulation of ion-solid interactions, Springer, Berlin (1991)

124 Iijima, T., Kato, S., Ikeda, R., Ohki, S., Kido, G., Tansho, M., Shimizu, T. *Chem. Letter* **34**, 1286-7 (2005)

125 Hasnaoui, A., Politano, O., Salazar, J. M., Aral, G., *Phys. Rev B* **73**, 035427 (2006)

126 Hattori, S., Kalia, R. K., Nakano, A., Nomura, K., Vashishta, P., *Appl. Phys. Lett.* **101**, 063106 (2012)

127 Yamamura, Y., Shindo, S., *Rad. Eff.* **80**, 57-72 (1984)

128 Oechsner, H., *Appl. Phys.* **8**, 185-198 (1975)

129 Depla, D., Mahieu, S. (eds.): Reactive Sputter Deposition, Springer, Heidelberg (2008)

130 Ulitschka, M., Bauer, J., Frost, F., Arnold, T., *Proc. SPIE* **11032**, 110320D (2019)

131 Frost, F., Schindler, A., Bigl, F., *Appl. Phys. A* **66**, 663-668 (1998).

132 Yeh, C.-T., Tuan, W.-H., *J. Adv. Ceram.* **6**, 27-32 (2017)

133 Sharma, N., Ilango, S., Dash, S., Tyagi, A. K., *Thin Solid Films* **636**, 626-633(2015)

134 Dutta, I., Mitra, S., Rabenberg, L., *J. Am. Ceram. Soc.* **75**, 3149-3153 (1992)

135 Yue, R., Wang, Y., Wang, Y., Chen, C., *Appl. Surf. Sci.* **148**, 73-78 (1999)

136 Korbutowicz, R., Zakrzewski, A., Rac-Rumijowska, O., Stafiniak, A., Vincze, A., *J Mater Sci.*: *Mater Electron* **28**, 13937-13949 (2017)

137 Marot, L., De Temmermann, G., Oelhafen, P., Covarel, G., Litnovsky, A., *Rev. Sci. Instrum.* **78**, 103507 (2007)

138 Toyoshima, A., Kikuchi, T., Tanaka, H., Mase, K., Amemiya, K., *J Synchrotron Radiat.* **22**, 1359–1363 (2015)

139 Chauvet, C., Polack, F., Silly, M. G., Lagarde, B., Thomasset, M., Kubsky, S., Duval, J. P., Risterucci, P., Pilette, B., Yao, I., Bergeard, N., Sirotti, F., *J Synchrotron Radiat.* **18**, 761-4 (2011)

140 Voigt, A., Gruetzner, G., Sauer, E., Helm. S., Harder, T., Fehlberg, S., Bendig, J., *Proc. SPIE* **2438**, 413-420 (1995)

141 Bruce, R. L., Weilnboeck, F., Lin, T., Phaneuf, R. J., Oehrlein, G. S., Long, B. K., Willson, C. G., Vegh, J. J., Nest, D., Graves, D. B., *J. Appl. Phys.,* **107**, 084310 (2010)

142 Pal, A. R., Bruce, R. L., Weilnboeck, F., Engelmann, S., Lin, T., Kuo, M.-S., Phaneuf, R. J. Oehrlein, G. S., *J. Appl. Phys.* **105,** 013311 (2009)

143 Sumiya, M., Bruce, R., Engelmann, S., Weilnboeck, F., Oehrlein, G. S., *J. Vac. Sci. Technol. B*, **26**, 1637 (2008)

144 Luckman, G. (1993). Measurement of wafer temperature variations using photoresist reticulation thresholds, *J. Vac. Sci. Technol. B,* **11,** 99.

145 Hesse, M., Meier, H., Zeeh, B. (eds.): Spektroskopische Methoden in der organischen Chemie, Georg Thieme Verlag, Stuttgart, New York. (2005)

146 Turner, S. R., Daly, R. C., *J. Chem. Educ.* **65**, 322-325 (1988)

147 micro resist technology GmbH, Processing guideline of ma N 2400 negative photoresist, Berlin, Germany

148 Voigt, A., Zur Chemie photolytisch generierter Arylnitrene in Polymermatrizen, Dissertation, Humboldt-Universität zu Berlin (1998)

149 Sensu, Y., Sekiguchi, A., *Proc. SPIE* **4979**, 561-581 (2003)

150 Voigt, A., Elsner, H., Meyer, H. G., Gruetzner, G., *Proc. SPIE* **3676**, 485-491 (1999)

151 Elsner, H., Meyer, H.-G., Voigt, A., Gruetzner, G., *Microelectron. Eng*., **46**, 389-392 (1999)

152 Hashimoto, M., Iwayanagi, T., Shiraishi, H. Nonogaki, S., *Polym. Eng. Sci*, **26**, 1090-1095 (1986)

153 Lobo, H., Bonilla, J.V. (eds.): Handbook of Plastics Analysis, Marcel Dekker, Inc., New York (2003)

154 Conley, R. T., Bieron, J. F., *J. Appl. Polym. Sci.* **7**, 103–117 (1963)

155 Huang, J., Xu, M., Ge, Q., Lin, M., Lin, Q., Chen, Y., Chu, J., Dai, L. Zou, Y., *J. Appl. Polym. Sci* **97**, 652–658 (2005)

156 Lieber, E., Rao, C. N. R., Thomas, A. E., Oftedahl, E., Minnis, R., Nambury, C. V. N., *Spectrochim. Acta.,* **19**, 1135-1144 (1962)

157 Jackson, W. M., Conley, R. T., *J Appl Polymer Sci.* **8**, 2163-2193 (1964)

158 Gutmann, A., Kleinhaus, A., Bade, W., *Microelectron. Eng.* **3**, 329–337 (1985)

159 Orvek, K. J., Dennis, M. L., *Proc. SPIE* **0771**, 281-288 (1987)

160 ten Brinke, G., Karasz, F. E., Ellis, T. S., *Macromolecules*, **16**, 244–249 (1983)

161 Schuster, B. E., Haug, A., Häffner, M., Blideran, M. M., Fleischer, M., Peisert, H., Kern, D. P., Chassé, T., *Anal. Bioanal. Chem.,* **393**, 1899–1905 (2009)

162 Sumiya, M., Bruce, R., Engelmann, S., Weilnboeck, F., Oehrlein, G. S., *J. Vac. Sci. Technol. B*, **26**, 1978 (2008)

163 Conley, R. T., *J. Appl. Polym. Sci.* **9**, 1117-1126 (1965)

164 Kim, J., *J. Electrochem. Soc.*, **145**, 2314-2319 (1998)

165 Shulman, G. P., Lochte, H. W., *J. Appl. Polym. Sci.*, **10**, 619–635 (1966)

166 Morshed, M. M., Daniels, S. M., *IEEE Transactions on Plasma Science* **38**, 1512-1516 (2010)

167 Weill, A., Dechenaux, E., Paniez, P., *Microelectron. Eng.* **4**, 285–296 (1986)

168 Blideran, M. M., Häffner, M., Schuster, B.-E., Raisch, C., Weigand, H., Fleischer, M., Peisert, H., Chassé, T., Kern, D. P., *Microelectron. Eng.* **86**, 769-772 (2008)

169 Eckstein, W.: Sputtering Yields, In: Behrisch, R., Eckstein, W. (eds.) Sputtering by Particle Bombardment: Experiments and Computer Calculations from Threshold to MeV Energies, pp. 33-187, Springer, Berlin Heidelberg (2007)

170 Tartz, M., Heyn, T., Bundesmann, C., Zimmermann, C., Neumann, H., *Eur. Phys. J. D* **61**, 587–592 (2011)

171 Whetten, T. J., Ruoff, A. L., *Nucl. Instrum. Methods Phys. Res., Sect. B* **7-8**, 836-839 (1985)

172 Chu, W. K., Howard, J. K., Lever, R. F., *J. Appl. Phys.* **47**, 4500-4503 (1976)

173 Betz, G., *Surf. Sci.* **92**, 283-309 (1980)

174 Stefanov, P., Stanchev, A., *Mater. Chem. Phys.* **50**, 209–212 (1997)

175 Ho, P. S., Lewis, J. E., Wildman, H. S., Howard, J. K., *Surf. Sci.* **57**, 393-405 (1976)

176 Kelly, R., Lam, N. Q., *Radiat. Eff.* **19**, 39-48 (1973)

177 Balarin, M., Otto, G., Storbeck, I., Schenk, M., Wagner, H., *Thin Solid Films* **4**, 255-263 (1969)

178 Drobny, V. F., Pulfrey, D. L., *Thin Solid Films* **61**, 89-98 (1979)

179 Ferreira, F. F., Tabacniks, M. H., Fantini, M. C. A., Faria, I. C., Gorenstein, A., *Solid State Ion.* **86-88**, 971-976 (1996)

180 Winters, H. F., *J. Vac. Sci. Technol.* **20**, 493-497 (1982)

181 Frost, F., Ziberi, B., Schindler, A., Rauschenbach, B., *Appl. Phys. A* **91**, 551-559 (2008)

182 Stewart, A. D. G., Thompson, M. W., *J. Mater. Sci.* **4**, 56-60 (1969)

183 Teichmann, M., Lorbeer, J., Frost, F., Rauschenbach, B., *Nanoscale Res. Lett.* **9**, 439 (2014)

184 Madi, C. S., Anzenberg, E., Ludwig, K. F. Jr., Aziz, M. J., *Phys. Rev. Lett.* **106**, 066101 (2011)

185 Makeev, M. A., Barabási, A.-L., *Nucl. Instrum. Meth. B* **222**, 335–354 (2004)

186 Hofsäss, H., *Appl. Phys. A* 114, 401-422 (2014)

187 Karmakar, P., Ghose, D., *Surf. Sci*. **554**, L101-L106 (2004)

188 Škereň, T., Temst, K., Vandervorst, W., Vantomme, A., *New J. Phys.* **15**, 093047 (2013)

189 Hirata A., Tokura H., Yoshikawa M., *Thin Solid Films* **212** 43-48 (1992)

190 Holzwarth, M., Wissing, M., Simeonova, D. S., Tzanev, S., Snowdon, K. J., Yordanow, O. I., *Surf. Sci.* **331–333 B**, 1093-1098 (1995)

191 Kimura K., Fukui A., Nakajima K., Mannami M, *Nucl. Instrum. Methods B* **148**, 149-153 (1999)

192 Frost, F., Ziberi, B., Höche, T., Rauschenbach, B., *Nucl. Instruments Methods Phys. Res. Sect. B Beam Interact. Mater. Atoms* **216**, 9-19 (2004)

193 Frost, F., Lippold, G., Otte, K., Hirsch, D., Schindler, A., Bigl, F., *J. Vac. Sci. Technol. A* **17**, 793-796 (1999)